

Spring 2015

Pose Detection and Control of Unmanned Underwater Vehicles (UUVs) Utilizing an Optical Detector Array

Firat Eren

University of New Hampshire, Durham

Follow this and additional works at: <https://scholars.unh.edu/dissertation>

Recommended Citation

Eren, Firat, "Pose Detection and Control of Unmanned Underwater Vehicles (UUVs) Utilizing an Optical Detector Array" (2015). *Doctoral Dissertations*. 2193.
<https://scholars.unh.edu/dissertation/2193>

This Dissertation is brought to you for free and open access by the Student Scholarship at University of New Hampshire Scholars' Repository. It has been accepted for inclusion in Doctoral Dissertations by an authorized administrator of University of New Hampshire Scholars' Repository. For more information, please contact nicole.hentz@unh.edu.

**POSE DETECTION AND CONTROL OF UNMANNED UNDERWATER
VEHICLES (UUVs) UTILIZING AN OPTICAL DETECTOR ARRAY**

BY

FIRAT EREN

B.S. in Mechatronics Engineering, Sabanci University, Turkey, 2008

M.S. in Mechanical Engineering, University of New Hampshire, USA, 2011

DISSERTATION

Submitted to the University of New Hampshire
in Partial Fulfillment of the Requirements for the Degree of

Doctor of Philosophy
in
Mechanical Engineering

May, 2015

ALL RIGHTS RESERVED

©2015

Firat Eren

This dissertation has been examined and approved in partial fulfillment of the requirements for the degree of Doctor of Philosophy in Mechanical Engineering by:

Dissertation Co-director, Dr. May-Win Thein
Associate Professor of Mechanical and Ocean Engineering

Dissertation Co-director, Dr. Shachak Pe'eri
Research Associate Professor in the Center for Coastal and Ocean Mapping

Dr. Barbaros Celikkol
Professor of Mechanical and Ocean Engineering

Dr. Yuri Rzhanov
Research Professor in the Center for Coastal and Ocean Mapping

Dr. M. Robinson Swift
Professor of Mechanical and Ocean Engineering

On 04/17/2015

Original approval signatures are on file with the University of New Hampshire Graduate School.

DEDICATION

*Dedicated to my parents,
Ayhan Eren and Abdullah Eren*

ACKNOWLEDGEMENTS

I would like to thank Dr. Barbaros Celikkol for introducing me to the world of Ocean Engineering which enabled me to complete my Ph.D. During the course of my 7 years at UNH, he had been an excellent mentor and a great friend, always showing his support inside and outside the university, expecting nothing in return but my success. He was a role model for me and I feel privileged to learn from him. I will never be able to repay him my gratitude in my lifetime.

Thanks to Dr. May-Win Thein for creating a research environment which helped me to become an independent researcher. I appreciate her support and generosity during my entire study. I also enjoyed our conference trips to Taipei, Keyport, Hampton Roads and Orlando.

I am grateful to Dr. Shachak Pe’eri for guiding me throughout the research and his contributions on my professional and personal development. It was a great pleasure for me to work with him and be a part of the same team. I learned a lot from him and I am looking forward to learning from him even more.

Dr. Yuri Rzhanov was always there when I got stuck on the research. I enjoyed our discussions on the detector array simulator. He expanded my horizons by looking at things from a different point of view.

Many thanks to Dr. Robinson Swift for his time in evaluating the dissertation.

I would also like to thank to Dr. Martin Renken for the technical discussions which improved the quality of the research.

Paul Lavoie contributed greatly on the design and machining of the waterproof acrylic fixtures He went above and beyond to help me carry out my research and he was very patient

with me when I had questions.

Matt Birkebak and Tim Brown worked long late hours with me in Chase Ocean Engineering Lab during the experimental stage of the research. It was also a pleasure for me to be the grad student adviser of their Harbor Security senior design team.

I also had the pleasure of being the grad student adviser of UNH Remotely Operated Vehicle (ROV) teams from 2011-2015. I also would like to thank to each member of the ROV teams for the past 4 years.

Thanks to Tom Fuller and Jesse Maillhot for their contributions on the prototype data acquisition system for the detector array.

The materials and supplies used in this research were funded by Naval Engineering Education Consortium (NEEC) and Naval Sea Systems Command (NAVSEA). I acknowledge the funding sources from UNH Graduate School Dissertation Fellowship (2014-2015), the LINK Foundation Fellowship for Ocean Engineering and Instrumentation (2013-2014), UNH Summer Teaching Assistant Fellowship (2012), Leslie S. Hubbard Marine Endowment to support Marine Research Development/Equipment (2012). I also acknowledge UNH Mechanical Engineering Department for supporting me through Teaching Assistant appointments.

Finally, I would like to thank to my family who was always there to support me. They helped me to get through the turbulence of living abroad.

TABLE OF CONTENTS

| | |
|--|-------------|
| DEDICATION | iv |
| ACKNOWLEDGEMENTS | v |
| LIST OF TABLES | xi |
| LIST OF FIGURES | xii |
| ABSTRACT | xvii |
| 1 INTRODUCTION | 1 |
| 1.1 Unmanned Underwater Vehicle Formation Control | 1 |
| 1.2 Unmanned Underwater Vehicle Inter-Communication | 3 |
| 1.3 Research Scope and Contributions | 5 |
| 1.3.1 Contributions | 6 |
| 1.3.2 Potential Contributions | 7 |
| 2 UNMANNED UNDERWATER VEHICLE MODELING, CONTROL AND STABILITY | 8 |
| 2.1 Introduction | 8 |
| 2.2 UUV Kinematics | 8 |
| 2.2.1 Euler Angles | 10 |
| 2.3 UUV Dynamics | 12 |
| 2.3.1 Newton-Euler Formulation | 12 |

| | | |
|----------|---|-----------|
| 2.4 | Rigid-Body Dynamics | 13 |
| 2.4.1 | Translational Motion | 15 |
| 2.4.2 | Rotational Motion | 16 |
| 2.4.3 | 6-DOF Rigid-Body Equations of Motion | 18 |
| 2.5 | Hydrodynamic Forces and Moments | 19 |
| 2.5.1 | Added Mass | 20 |
| 2.5.2 | Hydrodynamic Damping | 23 |
| 2.5.3 | Restoring Forces and Moments | 25 |
| 2.6 | Unmanned Underwater Vehicle Control and Stability | 26 |
| 2.6.1 | Proportional-Integral-Derivative (PID) Control | 26 |
| 2.6.2 | Sliding Mode Control (SMC) | 29 |
| 3 | CHARACTERIZATION OF OPTICAL COMMUNICATION IN A LEADER-FOLLOWER UUV FORMATION | 34 |
| 3.1 | Introduction | 35 |
| 3.2 | Theoretical Background | 35 |
| 3.2.1 | Beam pattern | 36 |
| 3.2.2 | Inverse Square Law | 36 |
| 3.2.3 | Beer-Lambert law | 38 |
| 3.3 | Experimental Test Platform | 38 |
| 3.4 | Optical Characterization Results | 41 |
| 3.5 | Optical Characterization Discussion and Conclusions | 44 |
| 4 | OPTICAL DETECTOR ARRAY DESIGN FOR NAVIGATIONAL FEED-BACK BETWEEN UUVs | 46 |
| 4.1 | Optical Design Considerations | 47 |
| 4.1.1 | Environmental Considerations | 48 |
| 4.1.2 | Hardware Considerations | 51 |

| | | |
|----------|--|-----------|
| 4.2 | The Simulator | 52 |
| 4.2.1 | The Simulator Reference Frames | 53 |
| 4.2.2 | Array Geometry | 53 |
| 4.2.3 | Radiometry | 55 |
| 4.3 | Results | 56 |
| 4.3.1 | Simulator Results | 56 |
| 4.3.2 | Detector Array Comparison | 57 |
| 4.3.3 | Experimental Confirmation | 60 |
| 4.4 | Discussion of Detector Array Design and Numerical Simulator | 62 |
| 5 | POSE DETECTION AND CONTROL ALGORITHMS FOR DYNAMIC POSITIONING OF UUVs VIA AN OPTICAL SENSOR FEEDBACK SYSTEM | 65 |
| 5.1 | Introduction | 66 |
| 5.2 | Pose Detection Algorithms | 66 |
| 5.2.1 | Phase Correlation and log-polar transform | 66 |
| 5.2.2 | Spectral Angle Mapper (SAM) | 69 |
| 5.2.3 | Calculation of image moment invariants | 70 |
| 5.3 | UUV Modeling and Control | 71 |
| 5.4 | Positioning Control Results | 72 |
| 5.4.1 | Static-Dynamic System | 73 |
| 5.4.2 | Dynamic-Dynamic System | 80 |
| 5.5 | Discussion of Analytical Pose Detection and Positioning Control | 82 |
| 6 | EXPERIMENTAL POSE DETECTION AND POSITIONING CONTROL | 85 |
| 6.1 | Docking Station Maneuvers | 86 |
| 6.2 | Detection Array Hardware | 88 |
| 6.3 | Methodology | 90 |

| | | |
|----------|--|------------|
| 6.3.1 | Photodiode and Pose Estimation Calibration Procedure | 92 |
| 6.3.2 | Stochastic Assessment of Pose Uncertainty | 96 |
| 6.3.3 | Pose Detection Performance Evaluation | 98 |
| 6.4 | Calibration Results | 99 |
| 6.5 | Stochastic Model Results | 100 |
| 6.6 | Pose Detection Performance Evaluation | 102 |
| 6.7 | Discussion of Experimental Pose Detection Results | 106 |
| 7 | DISCUSSION | 110 |
| 8 | CONCLUSIONS | 115 |
| | LIST OF REFERENCES | 118 |
| A | Numerical Simulator Algorithms and Frame Design | 127 |
| B | Photodiode Data Collection Procedure using Beagleboard-XM and two Arduinos | 129 |
| B.1 | Arduino | 130 |
| B.2 | Beagleboard-XM (BB-XM) | 130 |
| C | Programs for Experimental Data Collection and Analysis | 137 |
| C.1 | Program to collect photodiode data to Arduino (hmtsu.ino) | 137 |
| C.2 | Program to get the photodiode readings from Arduino to BB-XM (readPD.py) | 138 |
| C.3 | Program to get the photodiode readings from BB-XM to PC and save as a .txt file (getPD.py) | 139 |
| C.4 | Program that extracts the intensity readings from the text file and processes | 140 |
| D | Beam Patterns from Experimental Data | 145 |

LIST OF TABLES

| | | |
|-----|--|----|
| 2.1 | SNAME notation for marine vehicles. | 9 |
| 5.1 | A portion of the look-up table for pose detection. | 69 |
| 5.2 | Initial, reference and final UUV positions and orientations for a 21 x 21 curved array for decoupled 5-DOF Control. | 76 |
| 5.3 | Initial, reference and final UUV positions and orientations for a 5 x 5 curved array for decoupled 5-DOF Control. | 76 |
| 5.4 | Initial, reference and final UUV positions and orientations for a 5 x 5 curved array for decoupled 4-DOF control. | 78 |
| 5.5 | Initial, reference and final UUV positions and orientations for a 5 x 5 curved array for dynamic-dynamic control. | 81 |
| 6.1 | Uncertainty parameters for Monte Carlo simulations. | 97 |

LIST OF FIGURES

| | | |
|-----|---|----|
| 2.1 | The body-fixed reference frame and the earth fixed reference frame. | 9 |
| 2.2 | The earth-fixed non-rotating reference frame XYZ and the body-fixed rotating reference frame $X_oY_oZ_o$ | 14 |
| 2.3 | Two dimensional added mass coefficients used in strip theory. | 23 |
| 2.4 | UUV Control Block diagram with the output obtained from optical feedback array. | 27 |
| 3.1 | Light intensity as a function of polar angle θ | 37 |
| 3.2 | Experimental schematic of UNH tow tank. | 39 |
| 3.3 | Experimental Setup for translational 3-D underwater experiments. (Left) spectrometer unit and its connections. (Right) transmitting unit mounted to the wall of the tank. | 41 |
| 3.4 | Diffuse attenuation graph. | 42 |
| 3.5 | The intensity vs. distance plot. | 43 |
| 3.6 | Plot of the cross-sectional beam pattern. The measurements were collected from 0 to 1.0 m at x -axis and at 4.5 m at the illumination axis for 50 W light source. The measurements between 500-550 nm are averaged. | 44 |
| 4.1 | Schematic illustration of array designs used in the simulator: (a) Planar array and (b) Curved array. | 48 |

| | | |
|-----|--|----|
| 4.2 | Optical detector array and relevant optical angles, the solid line representing the light ray reaching a detector, the dashed line represents the optical axis and the dotted line represents the normal to the array. | 49 |
| 4.3 | Key image parameters and intensity profiles for a planar array with hardware and environmental background noise: (top left) Output image from the simulator, (top right) Horizontal intensity profile, (bottom left) Vertical intensity profile, (bottom right) Input values used to generate output image and key parameters describing output image. | 58 |
| 4.4 | Key image parameters and intensity profiles for a curved array with hardware and environmental background noise: (top left) Output image from the simulator, (top right) Horizontal profile, (bottom left) Vertical profile, (bottom right) Input values used to generate output image and key parameters describing output image. | 59 |
| 4.5 | Comparative resemblance results (SAM angles) for 21 x 21 element curved and planar array (at x=4m) as a function of: (a) lateral translation, (b) yaw rotation. | 60 |
| 4.6 | Comparative resemblance results (i.e., SAM angle) with respect to varying array sizes (incorporating environmental and background noise): (a) Under lateral motion (b) Under angular rotation. | 61 |
| 4.7 | Comparative resemblance results (i.e., SAM angle) with respect to operational distance (incorporating environmental and background noise): (a-c) lateral shift, (d-f) yaw rotation - (a, d) 3 x 3 array (b, e) 5 x 5 array (c, f) 101 x 101 array with spacing of 0.2 m, 0.1 m and 0.004 m, respectively. | 62 |
| 4.8 | Comparison of Experimental and Simulation results (a) 4 m (b) 5 m (c) 6 m (d) 7 m (e) 8 m. | 63 |
| 5.1 | Transformation of an image from Cartesian space (left) to polar space (right). | 68 |

| | | |
|-----|---|----|
| 5.2 | (Left) Image for a specific relative geometry between the light source and the detector. (Right) Image moments invariants output matrix. | 71 |
| 5.3 | Independent DOF SMC results for a curved 21 x 21 array. (a) x -axis control (b) y -axis control (c) z -axis control (d) yaw control (e) pitch control. | 75 |
| 5.4 | Independent DOF control results with SMC for a curved 5 x 5 array. (a) x -axis control (b) y -axis control (c) z -axis control (d) yaw control (e) pitch control. | 77 |
| 5.5 | PID x -axis control for a 5 x 5 array. | 78 |
| 5.6 | UUV docking case study using SMC for a 5 x 5 array. The UUV with four initial non-zero pose errors is commanded to position itself with respect to a fixed light source. (a) x -axis control (b) y -axis control c) yaw control d) z -axis control. | 79 |
| 5.7 | UUV docking case study using SMC for a 5 x 5 array with a current of -0.03 m/s in x -axis. (a) x -axis control (b) y -axis control c) yaw control d) z -axis control. | 80 |
| 5.8 | The leader-follower case study in a dynamic-dynamic system with SMC for a 5 x 5 array. (a) x -axis control (b) y -axis control and (c) z -axis control. . . . | 82 |
| 6.1 | (a) Funnel type docking station and (b) Pole type docking station architectures. | 87 |
| 6.2 | (Left) Optical Module Concept with data acquisition components. (Right) ROV platform. | 89 |
| 6.3 | Reverse-bias circuit used in the experiments. | 90 |
| 6.4 | The optical detector array used in the experiments. (Left) Top view. (Right) Side view. | 90 |
| 6.5 | Detector array mounted on the dynamic platform on the wave and tow tank. | 92 |
| 6.6 | 400 W light beacon mock-up docking station mounted on the wall of the wave and tow tank. | 93 |
| 6.7 | Photodiode Calibration. | 94 |

| | | |
|------|--|-----|
| 6.8 | Diagram for temperature calibration. | 94 |
| 6.9 | Experimental setup for photodiode response to the temperature changes. . . | 95 |
| 6.10 | Monte Carlo flow diagram for the pose statistics. | 97 |
| 6.11 | Monte Carlo generated CI bounds (95%). | 101 |
| 6.12 | Monte Carlo Simulation results with 95% CI bounds for navigation in $x - y$ plane. (Top-left) Nominal x -axis pose estimates. Middle-left: y -axis estimation. (Bottom-left) z -axis estimation. (Top-right) UUV reference navigation in the $x - y$ plane and the nominal estimation. (Bottom Right) Yaw pose estimation. | 102 |
| 6.13 | Empirical Pose detection for case 1: (Top left): Reference position, x -axis pose estimate. (Top right): Velocity reference, raw velocity estimates and moving average window of size 10 applied to the raw velocity estimates. (Bottom left): y -axis pose estimate. (Bottom right): z -axis pose estimate. | 104 |
| 6.14 | Empirical Pose detection for case 1: (Top left): Reference position, x -axis pose estimate. (Top right): Velocity reference, raw velocity estimates and moving average window of size 10 applied to the raw velocity estimates. (Bottom left): y -axis pose estimate. (Bottom right): z -axis pose estimate. | 105 |
| 6.15 | Yaw and y -axis cross-talk when there is only yaw motion. | 107 |
| A.1 | Numerical Simulator input parameters | 127 |
| A.2 | Numerical Simulator Flow Diagram. | 127 |
| A.3 | 4-DOF system detection and control strategy. | 128 |
| A.4 | Detector Array Frame dimension drawing. | 128 |
| B.1 | Photodiode-PC communication general diagram. | 130 |
| B.2 | Arduino sketch. This will be for one Arduino. For the other Arduino change the 13 to 12 and other variables accordingly. | 131 |
| B.3 | BB-XM setup. | 132 |

| | | |
|-----|---|-----|
| B.4 | Minicom login screen. | 133 |
| B.5 | Serial to USB port check on PC. | 133 |
| B.6 | Arm login and password screen. | 134 |
| B.7 | Arduino Device names verified in the BB-XM. | 135 |
| B.8 | The program that reads data from two Arduinos and passes it to the PC. (readPD.py). | 136 |
| B.9 | The program that reads the serial output of BB-XM and saves it to a file (getPD.py). | 136 |
| D.1 | Beam pattern images at x=4.5 m. | 145 |
| D.2 | Beam pattern images at x=5.5 m. | 146 |
| D.3 | Beam pattern images at x=6.5 m. | 146 |
| D.4 | Beam pattern images at x=7.5 m. | 147 |
| D.5 | Beam pattern images at x=8.5 m. | 147 |

ABSTRACT

POSE DETECTION AND CONTROL OF UNMANNED UNDERWATER VEHICLES (UUVs) UTILIZING AN OPTICAL DETECTOR ARRAY

by

Firat Eren

University of New Hampshire, May 2015

As part of the research for development of a leader-follower formation between unmanned underwater vehicles (UUVs), this study presents an optical feedback system for UUV navigation via an optical detector array. Capabilities of pose detection and control in a static-dynamic system (e.g. UUV navigation into a docking station) and a dynamic-dynamic system (e.g. UUV to UUV leader-follower system) are investigated. In both systems, a single light source is utilized as a guiding beacon for a tracker/follower UUV. The UUV uses an optical array consisting of photodiodes to receive the light field emitted from the light source. For UUV navigation applications, accurate pose estimation is essential. In order to evaluate the feasibility of underwater distance detection, the effective communication range between two platforms, i.e. light source and optical detector, and the optimum spectral range that allowed maximum light transmission are calculated. Based on the light attenuation in underwater, the geometry and dimensions of an optical detector array are determined, and the boundary conditions for the developed pose detection algorithms along with the error sources in the experiments are identified.

As a test bed to determine optical array dimensions and size, a simulator, i.e. numerical software, is developed, where planar and curved array geometries of varying number of elements are analytically compared and evaluated. Results show that the curved optical detector array is able to distinguish 5 degree- of-freedom (DOF) motion (translation in x , y , z -axes and pitch and yaw rotations) with respect to a single light source. Analytical pose detection and control algorithms are developed for both static-dynamic and dynamic-dynamic systems. Results show that a 5 x 5 curved detector array with the implementation of SMC is reasonably sufficient for practical UUV positioning applications.

The capabilities of an optical detector array to determine the pose of a UUV in 3-DOF (x , y and z -axes) are experimentally tested. An experimental platform consisting of a 5 x 5 photodiode array mounted on a hemispherical surface is used to sample the light field emitted from a single light source. Pose detection algorithms are developed to detect pose for steady-state and dynamic cases. Monte Carlo analysis is conducted to assess the pose estimation uncertainty under varying environmental and hardware conditions such as water turbidity, temperature variations in water and electrically-based noise. Monte Carlo analysis results show that the pose uncertainties (within 95% confidence interval) associated with x , y and z -axes are 0.78 m, 0.67 m and 0.56 m, respectively. Experimental results demonstrate that x , y and z -axes pose estimates are accurate to within 0.5 m, 0.2 m and 0.2 m, respectively.

CHAPTER 1

INTRODUCTION

1.1 Unmanned Underwater Vehicle Formation Control

Unmanned underwater vehicles (UUVs) play a major role in deep oceanic applications, such as underwater pipeline and cable inspection and in bathymetry. They also play a major role in military applications such as mine detection, harbor monitoring and anti-submarine warfare [1], [2], [3], [4], [5]. These applications mostly take place in deep sea environments and include tasks which involve significant weights that may take long periods of time and, therefore, are not suitable to be performed by divers. Some underwater operations (e.g., surveying a large area or an area with a complex seafloor bathymetry) require more than one UUV for efficient task completion. In these cases, the deployment of multiple UUVs in formation can perform such tasks and reduce the operational time and costs. A key requirement for this group of UUVs to move in a controlled formation is an underwater communication link between the UUVs [6], [7]. In addition to UUV operation in formation, underwater communication links can also be used for UUV docking [8] or data transfer from an operating UUV to a stationary data storage platform [9]. The two latter applications allow UUVs to operate with longer periods underwater without the need for excessive emerging/submerging. This study presents the development of an optical feedback interface and control system for two types of UUV applications: 1) Static-Dynamic system (e.g., a UUV and a data transfer/storage platform such as a docking station) and 2) Dynamic-Dynamic system (i.e., formation control of at least two UUVs). A key requirement for a fleet of UUVs to move in a controlled formation is a reliable underwater communication link between all

UUVs and between the UUV to a docking station.

There is a variety of possible formation architectures for controlled formation of unmanned vehicles. Most of these architectures require specialized on-board hardware to enable communication between the vehicles in formation. For coordinated formation control of unmanned vehicles, a variety of formation architectures and strategies have been developed. The main strategies include [10]:

Virtual structure approach - In this approach, the entire fleet of UUVs is treated as a single rigid structure [11]. The main advantage of this approach is that a highly precise formation can be maintained. However, its disadvantage is that the position and orientation from each of the individual UUVs states requires high computational complexity [12].

Behavior based methods - Several behaviors for each robot UUV are employed and final control action is obtained from the weighting of each behavior [13]. However, the stability of the system is not guaranteed because there is insufficient modeling information of the subsystems and the environment.

Leader-follower - This method employs one vehicle (the leader) that guides the other vehicles (the followers) in the formation [14]. Based on one-way communication transmitted from the leader, the followers position themselves relative to the leader position and orientation. The leader-follower method is considered less complex than the other approaches as it requires no feedback from the followers to the leader [15]. The disadvantage of this method is that if there is an error in the leaders trajectory, the followers deviate from their trajectory as well and positioning errors accumulate.

Artificial potentials- In artificial potentials an interaction control force is defined between the vehicles. The artificial potential uses this force to enforce a desired inter-vehicle spacing [16]. In this method, there is no leader vehicle assigned in the fleet. This eliminates single point failures and adds robustness to the system. However, the assumption is that each node is equipped with appropriate sensors so as to determine the range and forces between each of the nodes, which in turn increases the hardware and complexity in the system [17].

Graph theory Graph theory allows flexibility in changing the group formation during the operation [18]. However, this approach requires a list of all possible transitional geometries that are expected to occur in the UUVs that are in the formation. In addition, a good plan of action is needed a priori when faced with environmental and sensor constraints.

The formation control approach used in this study, more specifically in the dynamic-dynamic system, is the leader-follower strategy because of the simplicity in its implementation. In an underwater environment, the communication signals commonly used in aerial and terrestrial vehicles (e.g., GPS and radio signals) are significantly attenuated and thus cannot be used.

1.2 Unmanned Underwater Vehicle Inter-Communication

Most studies on inter-communication between UUVs have concentrated on acoustic communication, which shows good performance over long distances [19], [20], [21], [22], [23], [24], [25], [26]. Acoustic communication types used in underwater operations consist of Long Baseline (LBL), Short Baseline (SBL) and Ultra-Short Baseline (USBL) systems. In LBL, multiple acoustic transponders are placed on the seafloor and provide high accuracy navigation for underwater tasks that require precision. LBL systems are used in leader-follower formation flying systems [3] SBL systems are mainly used for tracking of underwater vehicles and divers. Unlike LBL systems, SBL transponders are not placed on the seafloor. Multiple SBL transponders are placed in water from the sides of the ship and one transponder is placed on the target to be tracked. SBL systems are used for communication between UUVs and docking stations [27]. USBL systems which offer fixed precision consist of two transponders, one is lowered to the sea on the ship and the other one is placed on the target of interest. In addition, USBL systems have found application in docking systems as well [28].

The necessary hardware for acoustics communication, however, is costly and requires payload considerations in the UUV platform design [29]. In areas with large traffic volume, such as harbor and recreational fishing areas, the marine environment can become acous-

tically noisy. This noise can reduce the performance of the acoustic communication and may not allow for UUV operations such as docking. A cost-effective alternative is optical detection that either uses existing hardware (e.g., light sources as beacons) or additional hardware, i.e. low cost, commercially available off the shelf (COTS) photo detectors, etc. In astronautical and aeronautical applications, optical communications are used for navigation, docking and data transfer [30], [31]. For example, free space optical communication is used in rendezvous radar antenna systems [32]. In both cases of interspacecraft rendezvous and docking, a continuous-wave laser is transmitted from the pursuer spacecraft to a target spacecraft or to aid in the docking process [33]. The challenge to conduct underwater optical communication is that light is significantly more scattered and is absorbed more quickly in water than it does in air. As a result, the effective communication range is, however, shorter than that of acoustic communication [34]. Optical communication for data transfer in underwater was demonstrated at range of 30 m for clear water conditions [35]. In addition to relatively shorter range of operation, the optical properties of water (e.g., diffuse attenuation coefficient and scattering) constantly change and affect communication reliability [36], [37], [38], [39], [40], [41], [42], [43].

Many possible geometric shapes for optical detector arrays exist, but the two most common array designs in literature are planar and curved [44], [45], each design having its own benefits. A planar-array design can maximize the signal-to-noise ratio between all its elements, while curved arrays require a smaller number of optical elements and results in a larger field of view. Currently, studies that have investigated optical communication for UUVs are very limited and focus mainly on planar arrays for Autonomous Underwater Vehicles (AUVs). These studies include an estimation of AUV orientation to a beacon by using a photodiode array [46] and distance measurement between two UUVs [47], [48]. In addition to array designs for communication between UUVs, other studies have investigated optical communications for docking operations. For example, a single detector (quadrant photodiode) has been used to operate as a 2 x 2 detector array [49]. In addition, researchers

have mounted an optical detector on an AUV to detect translational motion of the AUV with respect to a light source. Optical communication for distance sensing between a swarm of UUVs was conducted using a LED transceiver with an IrDA encoder/decoder chip [50]. In addition to navigation purposes, the use of optical communication has been investigated for transmitting remote control commands [51] and data transfer rates [52], [53], [54], [55]. Results based on laboratory and field work showed that an optical modem system consisting of an omnidirectional light source and photomultiplier tube can achieve a data streaming rate of up to 10 Mbit/s, with a reported 1.2 Mbit/s data transfer rate up to 30 m underwater in clear water conditions [56]. Other studies utilized underwater sensor network consisting of static and mobile nodes for high-speed optical communication system, where a point-to-point node communication is proposed for data muling [57].

Previous studies using acoustic communication evaluated the control performance of the UUVs for docking applications, namely using Autonomous Underwater Vehicles (AUVs) that include: Adaptive Control Strategy [58] Proportional-Integral-Derivative (PID) [59], [60]; Multi-Input-Multi-Output controller [61]; and Sliding Mode Controller (SMC) and its variants, namely High-Order SMC (HOSMC) and State Dependent Riccati Equation-HOSMC (SDRE-HOSMC) [62]. Recent studies have demonstrated the potential use of both acoustic and optical communication for docking [63], [64], [65]. In these systems, acoustic communication is used in relatively longer ranges, 100 m, for navigating towards a docking station and video cameras are used in closer ranges, 8-10 m, to guide the vehicle into the docking station. In this study, PID and SMC are investigated for both static-dynamic and dynamic-dynamic systems.

1.3 Research Scope and Contributions

The scope of work in this study is on the control between two UUVs and between a UUV and docking stations) using only optical communication. The three main goals in this study are:

1. **Design of a cost-effective optical detector array interface.** In order to receive feedback to the controls, an optical detector array interface is vital. A guiding light beacon will be used as a transmitter. The light field intersecting with the detector module will be translated into an electronic signal for pose detection and control purposes.
2. **Evaluation of control and image processing algorithms to be used in pose detection and UUV control.** For timely and stable response of the UUV to the changes in the optical input coming from another UUV or a docking station, the performance of image processing and control algorithms need to be evaluated. The performance should take into account the optical variability that exists in natural waters.
3. **Development of optical detector hardware to obtain real-time pose feedback signal for the control of a UUV.** A proof-of-concept hardware will demonstrate the performance of pose detection and control in laboratory settings.

1.3.1 Contributions

The purpose of this research is to expand the limited current application of optical detection of UUVs by generalizing the types of underwater platforms by the investigation of various types of detector arrays, and by the analysis and development of various pose detection algorithms. The following are contributions of this research:

1. Experimental work is performed to determine the wavelength band that allows maximum light transmittance. The effective range that allows usable optical feedback between two platforms is also determined. Approximate dimensions of an optical array are determined by observing the beam divergence under water.
2. A numerical simulator is developed to evaluate different array geometries and array sizes for underwater position and orientation detection to be used in static-dynamic

and/or dynamic-dynamic systems.

3. Analytical pose detection and control algorithms are developed to control the UUV in static-dynamic and dynamic-dynamic scenarios with a single light source. The algorithm effectiveness is evaluated based on processing time, positional accuracy and dependence on the environmental characteristics such as noise.
4. An optical array interface of 5 x 5 photodiodes is built and experimentally tested. Algorithms are developed to estimate pose in all translational axes for steady-state and dynamic cases. Monte Carlo analysis is performed to assess the accuracy of the pose estimates under environmental and hardware uncertainty.

1.3.2 Potential Contributions

In addition to the main goals of this study to develop an interface and controls between two UUVs and between a UUV and a docking station, there are other applications that can benefit from this study:

Free-Space Optical (FSO) communication - In this study a continuous-wave light source is used as the transmitting signal. However, the bandwidth of the photodetectors allows the transmission of pulsed signals which can provide coded control signals and also data transfer.

Beam diagnostics - The two array designs, i.e. planar and curved arrays, are compared based on their ability to generate a unique image footprint. This can also be used to evaluate scattering and absorption of light through the water column in addition to the geometrical and environmental factors that affect the light travel under water.

CHAPTER 2

UNMANNED UNDERWATER VEHICLE MODELING, CONTROL AND STABILITY

2.1 Introduction

The control of a UUV to either navigate to a predefined point in space or to follow a path requires a fundamental understanding of the UUV model. In this chapter, the UUV model is analyzed in two sections: kinematics (i.e. geometrical aspects of the motion without force analysis) and UUV dynamics (i.e. analysis of the forces that contribute to the motion of the UUV). More detailed analysis of marine vehicle modeling (including UUVs) is provided in [64], [65], [66]. This chapter summarizes the main concepts demonstrated in these sources.

2.2 UUV Kinematics

UUVs are capable of motion in 6-DOF. For analysis of UUV motion, two coordinate frames are introduced (Figure 2.1):

1. The moving coordinate frame, as defined by $X_o - Y_o - Z_o$, orthogonal triad, which is fixed to the UUV body and thus also named body-fixed reference frame. X_o defines the longitudinal axis (aft to fore), Y_o defines the transverse axis (port to starboard) and Z_o defines the normal axis (top to bottom)
2. Earth-fixed reference frame. The motion of the UUV in body fixed frame is described in the Earth-fixed frame which is also referred as the inertial reference frame.

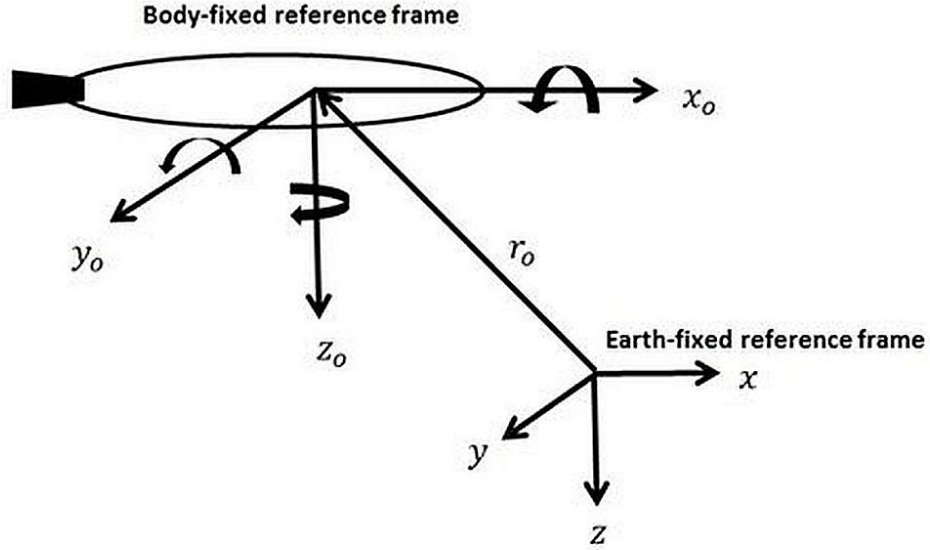


Figure 2.1: The body-fixed reference frame and the earth fixed reference frame.

Because the rotation of the Earth does not affect the motion of that of UUVs significantly (as they are considered low-speed vehicles), it is assumed that the acceleration of a point on the Earth-fixed reference frame can be neglected. Thus, UUV position and orientation can be expressed in the Earth-fixed frame while the linear and angular velocities are expressed in the body-fixed reference frame. The variables in this manuscript are defined according to the SNAME (the Society of Naval Architects and Marine Engineers) (1950) notation as demonstrated in Table 2.1.

| DOF | Motion type | Forces and Moments | Linear and Angular Velocities | Positions and Euler angles |
|-----|-------------|--------------------|-------------------------------|----------------------------|
| 1 | Surge | X | u | x |
| 2 | Sway | Y | v | y |
| 3 | Heave | Z | w | z |
| 4 | Roll | K | p | ϕ |
| 5 | Pitch | M | q | θ |
| 6 | Yaw | N | r | ψ |

Table 2.1: SNAME notation for marine vehicles.

The motion of a UUV in 6-DOF can be represented in the following vectorial forms:

$$\boldsymbol{\eta} = [\boldsymbol{\eta}_1^T \boldsymbol{\eta}_2^T]^T \quad \boldsymbol{\eta}_1 = [x, y, z]^T \quad \boldsymbol{\eta}_2 = [\phi, \theta, \psi]^T \quad (2.1)$$

$$\boldsymbol{\nu} = [\boldsymbol{\nu}_1^T \boldsymbol{\nu}_2^T]^T \quad \boldsymbol{\nu}_1 = [u, v, w]^T \quad \boldsymbol{\nu}_2 = [p, q, r]^T \quad (2.2)$$

$$\boldsymbol{\tau} = [\boldsymbol{\tau}_1^T \boldsymbol{\tau}_2^T]^T \quad \boldsymbol{\tau}_1 = [X, Y, Z]^T \quad \boldsymbol{\tau}_2 = [K, M, N]^T \quad (2.3)$$

where $\boldsymbol{\eta} \in \mathbb{R}^{6 \times 1}$ denotes the position and orientation in the Earth-fixed coordinate frame, $\boldsymbol{\nu} \in \mathbb{R}^{6 \times 1}$ denotes the linear and angular velocities acting in the body-fixed frame and $\boldsymbol{\tau} \in \mathbb{R}^{6 \times 1}$ represents the forces and the moments acting in the UUV on the body-fixed reference frame. In this manuscript, the UUV orientation is described using Euler angle representation.

2.2.1 Euler Angles

The vehicle motion in body-fixed reference frame can be translated into the Earth-fixed coordinate system through a velocity transformation as in

$$\dot{\boldsymbol{\eta}}_1 = \mathbf{J}_1(\boldsymbol{\eta}_2) \boldsymbol{\nu}_1 \quad (2.4)$$

where $\mathbf{J}_1(\boldsymbol{\eta}_2)$ is the linear velocity transformation matrix from linear body-fixed velocity vector to the velocities expressed in Earth-fixed reference frame. The transformation matrix is a function of roll (ϕ), pitch (θ) and yaw (ψ) angles. $\mathbf{J}_1(\boldsymbol{\eta}_2)$ is described through a series of rotation sequences (3-2-1) as follows:

$$\mathbf{J}_1(\boldsymbol{\eta}_2) = \mathbf{C}_{z,\psi}^T \mathbf{C}_{y,\theta}^T \mathbf{C}_{x,\phi}^T \quad (2.5)$$

where the principle rotations $\mathbf{C}_{z,\psi}^T, \mathbf{C}_{y,\theta}^T, \mathbf{C}_{x,\phi}^T$ are defined as

$$\mathbf{C}_{z,\psi}^T = \begin{bmatrix} c\psi & s\psi & 0 \\ -s\psi & c\psi & 0 \\ 0 & 0 & 1 \end{bmatrix} \quad \mathbf{C}_{y,\theta}^T = \begin{bmatrix} c\theta & 0 & -s\theta \\ 0 & 1 & 0 \\ s\theta & 0 & c\theta \end{bmatrix} \quad \mathbf{C}_{x,\phi}^T = \begin{bmatrix} 1 & 0 & 0 \\ 0 & c\phi & s\phi \\ 0 & -s\phi & c\phi \end{bmatrix} \quad (2.6)$$

Here, $c(\cdot)$ and $s(\cdot)$ represent cosine and sine functions, respectively. Expanding formula 2.5 results in:

$$\mathbf{J}_1(\boldsymbol{\eta}_2) = \begin{bmatrix} c\psi c\theta & -s\psi c\phi + c\psi s\theta s\phi & s\psi s\phi + c\psi c\phi s\theta \\ s\psi c\theta & c\psi c\phi + s\phi s\theta s\psi & -c\psi s\phi + s\theta s\psi c\phi \\ -s\theta & c\theta s\phi & c\theta c\phi \end{bmatrix} \quad (2.7)$$

Similarly, the angular velocities acting on the body-fixed frame can be transformed into Euler rate vector $\dot{\boldsymbol{\eta}}_2 = [\dot{\phi}, \dot{\theta}, \dot{\psi}]^T$ as in

$$\boldsymbol{\eta}_2 = \mathbf{J}_2(\boldsymbol{\eta}_2) \boldsymbol{\nu}_2 \quad (2.8)$$

$\mathbf{J}_2(\boldsymbol{\eta}_2)$ is the angular velocity transformation matrix that transforms from angular body-fixed reference frame to Euler rate vector. Integration of Euler rate vector yields Euler angles. $\mathbf{J}_2(\boldsymbol{\eta}_2)$ is expressed as

$$\mathbf{J}_2(\boldsymbol{\eta}_2) = \begin{bmatrix} 1 & s\phi t\theta & c\phi t\theta \\ 0 & c\phi & -s\phi \\ 0 & s\phi/c\theta & c\phi/c\theta \end{bmatrix} \quad (2.9)$$

where $t(\cdot)$ represents tangent function. It should be noted that for a pitch angle of $\theta = \pm 90^\circ$, $\mathbf{J}_2(\boldsymbol{\eta}_2)$ is undefined. UUVs can possibly operate near this singularity point. To resolve this issue, quaternion representation [64] rather than Euler angle may be used. In this manuscript, UUVs are assumed to be mechanically designed and built stable to be within $\theta = \pm 10^\circ$. Therefore, the UUVs are physically prevented to approach the singularity point.

2.3 UUV Dynamics

6-DOF nonlinear UUV dynamic equations are expressed as

$$\mathbf{M}\dot{\boldsymbol{\nu}} + \mathbf{C}(\boldsymbol{\nu})\boldsymbol{\nu} + \mathbf{D}(\boldsymbol{\nu})\boldsymbol{\nu} + \mathbf{g}(\boldsymbol{\eta}) = \boldsymbol{\tau} \quad (2.10)$$

where $\mathbf{M} \in \mathbb{R}^{6 \times 6}$ is the inertial matrix including rigid body terms, \mathbf{M}_{RB} , and added mass, \mathbf{M}_A . $\mathbf{C}(\boldsymbol{\nu}) \in \mathbb{R}^{6 \times 6}$ is the Coriolis and centripetal terms consisting of rigid body Coriolis and centripetal terms \mathbf{C}_{RB} and hydrodynamic Coriolis and centripetal terms, \mathbf{C}_A . $\mathbf{D}(\boldsymbol{\nu}) \in \mathbb{R}^{6 \times 6}$ is the damping force matrix, $\mathbf{g}(\boldsymbol{\eta}) \in \mathbb{R}^{6 \times 1}$ is the gravitational forces and moments and $\boldsymbol{\tau} \in \mathbb{R}^{6 \times 1}$ is the vector of control inputs. The UUV 6-DOF dynamic equations are expressed using Newtons second law.

2.3.1 Newton-Euler Formulation

The foundations of Newton-Euler formulation are based on the Newtons second law relating the mass, m , acceleration, $\dot{\boldsymbol{\nu}}_c$, and force, \mathbf{f}_c , as follows:

$$m\dot{\boldsymbol{\nu}}_c = \mathbf{f}_c \quad (2.11)$$

subscript c denotes the center of mass of the body. Eulers first axiom states that the linear momentum of a body, \mathbf{p}_c is equal to the product of the mass and the velocity of the center of mass:

$$m\boldsymbol{\nu}_c = \mathbf{p}_c \quad (2.12)$$

Eulers second axiom states that the rate of change of angular momentum, \mathbf{h}_c , about a point fixed in Earth fixed reference frame or center of mass of the body is equal to the sum of external torques:

$$\mathbf{I}_c\dot{\boldsymbol{\omega}} = \mathbf{h}_c \quad (2.13)$$

where \mathbf{I}_c is the inertia tensor about the center of gravity. These expressions are used to derive the UUV rigid body equations of motion.

2.4 Rigid-Body Dynamics

Defining a body-fixed coordinate frame $X_oY_oZ_o$ rotating with an angular velocity vector $\omega = [\omega_1, \omega_2, \omega_3]^T$ about an Earth-fixed coordinate system XYZ (Figure 2.2), the inertia tensor of the body, I_o , in the body-fixed coordinate system $X_oY_oZ_o$ with an origin O is defined as

$$\mathbf{I}_o \triangleq \begin{bmatrix} I_x & -I_{xy} & -I_{xz} \\ -I_{yx} & I_y & -I_{yz} \\ -I_{zx} & -I_{zy} & I_z \end{bmatrix} \quad (2.14)$$

I_x , I_y and I_z are the moments of inertia about the X_o , Y_o and Z_o axes while the products of inertia $I_{xy} = I_{yx}$, $I_{xz} = I_{zx}$ and $I_{yz} = I_{zy}$. The elements of the inertia tensor are defined as

$$I_x = \int_V (y^2 + z^2) \rho_A dV; \quad I_{xy} = \int_V xy \rho_A dV = I_{yx} \quad (2.15)$$

$$I_y = \int_V (x^2 + z^2) \rho_A dV; \quad I_{xz} = \int_V xz \rho_A dV = I_{zx} \quad (2.16)$$

$$I_z = \int_V (x^2 + y^2) \rho_A dV; \quad I_{yz} = \int_V yz \rho_A dV = I_{zy} \quad (2.17)$$

where ρ_A is the mass density of the body.

The inertia tensor, \mathbf{I}_o , can be represented in the vector form:

$$\mathbf{I}_o \boldsymbol{\omega} = \int_V \mathbf{r} \times (\boldsymbol{\omega} \times \mathbf{r}) \rho_A dV \quad (2.18)$$

The mass of the body can be defined as

$$m = \int_V \rho_A dV \quad (2.19)$$

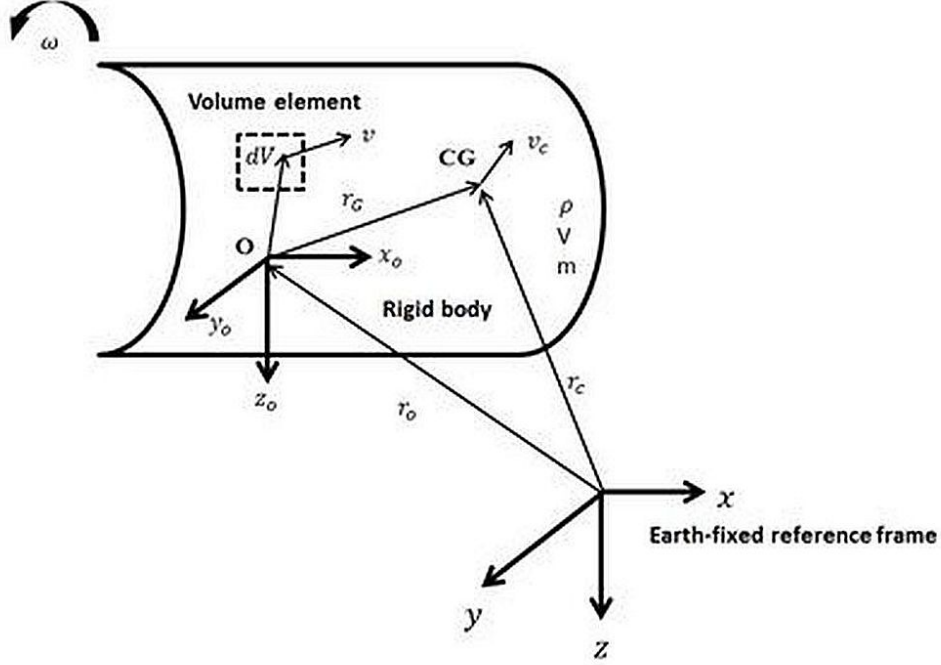


Figure 2.2: The earth-fixed non-rotating reference frame XYZ and the body-fixed rotating reference frame $X_oY_oZ_o$.

The underlying assumptions in the dynamics analysis of UUV are

1. The vehicle mass is constant in time, i.e. $\dot{m} = 0$
2. The vehicle is rigid: This assumption neglects the interacting forces between the individual UUV parts.
3. The Earth-fixed reference frame is inertial: This assumption eliminates the need to include the occurring forces due to Earth's motion relative to a star-fixed reference system which is used in space applications.

By utilizing the first assumption, the distance from the origin of the body fixed reference frame, $X_oY_oZ_o$, to the vehicles center of gravity is

$$\mathbf{r}_G = \frac{1}{m} \int_V \mathbf{r} \rho_A dV \quad (2.20)$$

In order to obtain the equations of motion from a selected arbitrary origin in the body-fixed coordinate system, the following is used

$$\dot{\mathbf{c}} = \dot{\mathbf{c}}_B + \boldsymbol{\omega} \times \mathbf{c} \quad (2.21)$$

Formula 2.21 relates the time derivative of an arbitrary vector in the Earth-fixed frame, i.e. $\dot{\mathbf{c}}$, to the time derivative of an arbitrary vector in the body-fixed reference frame, i.e. $\dot{\mathbf{c}}_B$. This relation yields:

$$\dot{\boldsymbol{\omega}} = \dot{\boldsymbol{\omega}}_B + \boldsymbol{\omega} \times \boldsymbol{\omega} = \dot{\boldsymbol{\omega}}_B \quad (2.22)$$

stating that the angular acceleration is equal in both reference frames.

2.4.1 Translational Motion

From Figure 2.2 it is seen that the distance from the origin of the Earth-fixed reference frame to the center of gravity of the vehicle, i.e. \mathbf{r}_C can be expressed as

$$\mathbf{r}_C = \mathbf{r}_G + \mathbf{r}_o \quad (2.23)$$

Thus, the velocity of the center of gravity is

$$\boldsymbol{\nu}_c = \dot{\mathbf{r}}_C = \dot{\mathbf{r}}_o + \dot{\mathbf{r}}_G \quad (2.24)$$

Utilizing the following relations $\mathbf{v}_o = \dot{\mathbf{r}}_o$ and $\dot{\mathbf{r}}_{G_B} = \mathbf{0}$ for rigid body,

$$\dot{\mathbf{r}}_{G_B} + \boldsymbol{\omega} \times \mathbf{r}_G = \boldsymbol{\omega} \times \mathbf{r}_G \quad (2.25)$$

$\dot{\mathbf{r}}_{GB}$ stands for time-derivative with respect to the body-fixed reference frame, $X_oY_oZ_o$. Therefore,

$$\boldsymbol{\nu}_c = \boldsymbol{\nu}_o + \boldsymbol{\omega} \times \mathbf{r}_G \quad (2.26)$$

The acceleration vector is:

$$\boldsymbol{\nu}_c = \dot{\boldsymbol{\nu}}_o + \dot{\boldsymbol{\omega}} \times \mathbf{r}_G + \boldsymbol{\omega} \times \dot{\mathbf{r}}_G \quad (2.27)$$

which in turn yields:

$$\boldsymbol{\nu}_c = \dot{\boldsymbol{\nu}}_{oB} + \boldsymbol{\omega} \times \boldsymbol{\nu}_o + \dot{\boldsymbol{\omega}}_B \times \mathbf{r}_G + \boldsymbol{\omega} \times (\boldsymbol{\omega} \times \mathbf{r}_G) \quad (2.28)$$

Substituting formula 2.28 into formula 2.11 results in

$$m(\dot{\boldsymbol{\nu}}_{oB} + \boldsymbol{\omega} \times \boldsymbol{\nu}_o + \dot{\boldsymbol{\omega}}_B \times \mathbf{r}_G + \boldsymbol{\omega} \times (\boldsymbol{\omega} \times \mathbf{r}_G)) = \mathbf{f}_o \quad (2.29)$$

If the arbitrary origin of the body-fixed coordinate system $X_oY_oZ_o$ is chosen to coincide with the center of gravity, the distance from the center of gravity to the origin, $\mathbf{r}_G = [0, 0, 0]^T$ and with $\mathbf{f}_o = \mathbf{f}_C$ and $\mathbf{v}_o = \mathbf{v}_C$, formula 2.29 reduces to

$$m(\dot{\boldsymbol{\nu}}_{CB} + \boldsymbol{\omega} \times \boldsymbol{\nu}_c = \mathbf{f}_c \quad (2.30)$$

2.4.2 Rotational Motion

The absolute momentum at the origin in Figure 2.2 is defined as

$$\mathbf{h}_o \triangleq \int_V \mathbf{r} \times \boldsymbol{\nu} \rho_A dV \quad (2.31)$$

Taking the time derivative of formula 2.31 yields:

$$\dot{\mathbf{h}}_o = \int_V \mathbf{r} \times \dot{\boldsymbol{\nu}} \rho_A dV + \int_V \dot{\mathbf{r}} \times \boldsymbol{\nu} \rho_A dV \quad (2.32)$$

Noting that $\mathbf{m}_o \triangleq \int_V \mathbf{r} \times \dot{\boldsymbol{\nu}} \rho_A dV$ and $\boldsymbol{\nu} = \dot{\mathbf{r}}_o + \dot{\mathbf{r}}$ which implies $\dot{\mathbf{r}} = \boldsymbol{\nu} - \boldsymbol{\nu}_o$ and using these relations with formula 2.32 yields

$$\dot{\mathbf{h}}_o = \mathbf{m}_o - \boldsymbol{\nu}_o \times \int_V \boldsymbol{\nu} \rho_A dV \quad (2.33)$$

or

$$\dot{\mathbf{h}}_o = \mathbf{m}_o - \boldsymbol{\nu}_o \times \int_V (\boldsymbol{\nu} + \dot{\mathbf{r}}) \rho_A dV = \mathbf{m}_o - \boldsymbol{\nu}_o \times \text{int}_V \dot{\mathbf{r}} \rho_A dV \quad (2.34)$$

Formula 2.34 can be rewritten by taking the time derivative of formula 2.20 as:

$$m \dot{\mathbf{r}}_G = \int_V \dot{\mathbf{r}} \rho dV \quad (2.35)$$

Using the fact that $\dot{\mathbf{r}}_G = \boldsymbol{\omega} \times \mathbf{r}_G$, formula 2.35 is rewritten as

$$\int_V \dot{\mathbf{r}} \rho dV = m(\boldsymbol{\omega} \times \mathbf{r}_G) \quad (2.36)$$

Substituting formula 2.36 in formula 2.34 results in

$$\dot{\mathbf{h}}_o = \mathbf{m}_o - m \boldsymbol{\nu}_o \times (\boldsymbol{\omega} \times \mathbf{r}_G) \quad (2.37)$$

Writing formula 2.31 as

$$\mathbf{h}_o = \int_V \mathbf{r} \times \rho_A dV = \int_V \mathbf{r} \times \boldsymbol{\nu}_o \rho_A dV + \int_V \mathbf{r} \times (\boldsymbol{\omega} \times \mathbf{r}) \rho_A dV \quad (2.38)$$

$\int_V \mathbf{r} \times \boldsymbol{\nu}_o \rho_A dV$ term in formula 2.38 can be rewritten as

$$\int_V \mathbf{r} \times \boldsymbol{\nu}_o \rho_A dV = \left(\int_V \mathbf{r} \rho_A dV \right) \times \boldsymbol{\nu}_o = m \mathbf{r}_G \times \boldsymbol{\nu}_o \quad (2.39)$$

Formula 2.38 reduces to

$$\mathbf{h}_o = \mathbf{I}_o \boldsymbol{\omega} + m \mathbf{r}_G \times \boldsymbol{\nu}_o \quad (2.40)$$

Under the assumption that \mathbf{I}_o is constant, we take the time-derivative of formula 2.40:

$$\dot{\mathbf{h}}_o = \mathbf{I}_o \dot{\boldsymbol{\omega}}_B + \boldsymbol{\omega} \times (\mathbf{I}_o \boldsymbol{\omega}) + m(\boldsymbol{\omega} \times \mathbf{r}_G) \times \boldsymbol{\nu}_o + m \mathbf{r}_G \times (\dot{\boldsymbol{\nu}}_{oB} + \boldsymbol{\omega} \times \boldsymbol{\nu}_o) \quad (2.41)$$

Using the relations $(\boldsymbol{\omega} \times \mathbf{r}_G) \times \boldsymbol{\nu}_o = -\boldsymbol{\nu}_o \times (\boldsymbol{\omega} \times \mathbf{r}_G)$ and eliminating $\dot{\mathbf{h}}_o$ term from formula 2.37 and formula 2.41 yields

$$\mathbf{I}_o \dot{\boldsymbol{\omega}}_B + \boldsymbol{\omega} \times (\mathbf{I}_o \boldsymbol{\omega}) + m \mathbf{r}_G \times (\dot{\boldsymbol{\nu}}_{oB} + \boldsymbol{\omega} \times \boldsymbol{\nu}_o) = \mathbf{m}_o \quad (2.42)$$

If the origin of the body-fixed coordinate system $X_o Y_o Z_o$ is chosen to coincide with the center of gravity of the UUV, then formula 2.42 simplifies to

$$\mathbf{I}_c \boldsymbol{\omega} + \boldsymbol{\omega} \times (\mathbf{I}_c \boldsymbol{\omega}) = \mathbf{m}_c \quad (2.43)$$

2.4.3 6-DOF Rigid-Body Equations of Motion

In this section, vector representation of the UUV dynamics will be shown. In addition, assumption that simplify the equations of motion will be introduced. Applying the following SNAME notation

$$\mathbf{f}_o = \boldsymbol{\tau}_1 = [X, Y, Z]^T = \text{External Forces}$$

$$\mathbf{m}_o = \boldsymbol{\tau}_2 = [K, M, N]^T = \text{External Moments about origin O}$$

$$\mathbf{v}_o = \boldsymbol{\nu}_1 = [u, v, w]^T = \text{Linear velocities on body-fixed coordinate frame } X_o Y_o Z_o$$

$$\boldsymbol{\omega} = \boldsymbol{\nu}_2 = [p, q, r]^T = \text{Angular velocities on body-fixed coordinate frame } X_o Y_o Z_o$$

$$\mathbf{r}_G = [x_G, y_G, z_G]^T = \text{center of gravity}$$

Applying this notation to the translational and rotational motion equations shown in previous sub-sections yields

$$\begin{aligned}
m[\dot{u} - vr + wq - x_G(q^2 + r^2) + y_G(pq - \dot{r}) + z_G(pr + \dot{q})] &= X \\
m[\dot{v} - wp + ur - y_G(r^2 + p^2) + z_G(qr - \dot{p}) + x_G(pq + \dot{r})] &= Y \\
m[\dot{w} - uq + vp - z_G(p^2 + q^2) + x_G(pr - \dot{q}) + y_G(qr + \dot{p})] &= Z \\
I_x \dot{p} + (I_z - I_y)qr - (\dot{r} + pq)I_{xz} + (r^2 - q^2)I_{yz} + (pr - \dot{q})I_{xy} + \\
m[y_G(\dot{w} - uq + vp) - z_G(\dot{v} - wp + ur)] &= K \\
I_y \dot{q} + (I_x - I_z)pr - (\dot{p} + qr)I_{xy} + (p^2 - r^2)I_{zx} + (pq - \dot{r})I_{yz} + \\
m[z_G(\dot{u} - vr + wq) - x_G(\dot{w} - uq + vp)] &= M \\
I_z \dot{r} + (I_y - I_x)pq - (\dot{q} + pr)I_{yz} + (q^2 - p^2)I_{xy} + (rq - \dot{p})I_{zx} + \\
m[x_G(\dot{v} - wp + ur) - y_G(\dot{u} - vr + wq)] &= N
\end{aligned} \tag{2.44}$$

These equations can be represented in a more compact, vector form as follows:

$$\mathbf{M}_{RB}\boldsymbol{\nu} + \mathbf{C}_{RB}(\boldsymbol{\nu})\boldsymbol{\nu} = \boldsymbol{\tau}_{RB} \tag{2.45}$$

The rigid-body equations can be simplified by choosing the origin of the body fixed-coordinate frame coinciding with the center of gravity. In this case $r_G = [0, 0, 0]$ and all the center of gravity related terms drop out of equation. This yields

$$\begin{aligned}
m(u - vr + wq) &= X & I_{x_c}p + (I_{z_c} - I_{y_c})qr &= K \\
m(v - wp + ur) &= Y & I_{y_c}q + (I_{x_c} - I_{z_c})pr &= M \\
m(w - uq + vp) &= Z & I_{z_c}r + (I_{y_c} - I_{x_c})pq &= N
\end{aligned} \tag{2.46}$$

2.5 Hydrodynamic Forces and Moments

Hydrodynamic forces acting on a rigid body, are analyzed as radiation-induced forces, i.e. when the rigid body is forced to oscillate with the wave excitation frequency and there are

no incident waves. In this case, the radiation induced forces and moments can be analyzed in three parts:

1. Added mass due to inertia of the surrounding fluid
2. Damping effects due to potential damping, skin friction, wave drift damping and vortex shedding
3. Restoring forces due to weight and buoyancy

The effect of hydrodynamic forces acting on the vehicle can be shown as follows

$$\boldsymbol{\tau}_H = -\boldsymbol{M}_A\boldsymbol{\nu} - \boldsymbol{C}_A(\boldsymbol{\nu})\boldsymbol{\nu} - \boldsymbol{D}(\boldsymbol{\nu})\boldsymbol{\nu} - \boldsymbol{g}(\boldsymbol{\eta}) \quad (2.47)$$

where \boldsymbol{M}_A and $\boldsymbol{C}_A(\boldsymbol{\nu})$ are added mass and hydrodynamic Coriolis and centripetal term matrices, $\boldsymbol{D}(\boldsymbol{\nu})$ is the hydrodynamic damping matrix including potential damping, skin friction, wave drift damping and vortex shedding, $\boldsymbol{g}(\boldsymbol{\eta})$ is the restoring forces. In addition to the hydrodynamic forces exerting on the UUV during the motion, environmental forces also affect the UUV motion. The environmental forces are mainly due to ocean currents, waves and winds. Combining all of these effects, the 6-DOF dynamic equations of motion of a UUV is

$$\boldsymbol{M}\dot{\boldsymbol{\nu}} + \boldsymbol{C}(\boldsymbol{\nu})\boldsymbol{\nu} + \boldsymbol{D}(\boldsymbol{\nu})\boldsymbol{\nu} + \boldsymbol{g}(\boldsymbol{\eta}) = \boldsymbol{\tau} + \boldsymbol{\tau}_H + \boldsymbol{\tau}_E \quad (2.48)$$

where $\boldsymbol{\tau}$ is the propulsion forces including the thruster/propellers and control surfaces/rudder forces and $\boldsymbol{\tau}_E$ denotes the environmental forces.

2.5.1 Added Mass

Added mass is the pressure-induced force and moment due to a forced harmonic motion of the body which are proportional to the acceleration of the body. As the UUV passes through

the fluid, the fluid must move aside and close behind the vehicle, i.e. open the passage for the UUV. The fluid passage possesses the kinetic energy (which would be non-existent if the UUV is stationary). Fluid kinetic energy can be written as

$$\mathbf{T}_A = \frac{1}{2} \boldsymbol{\nu}^T \mathbf{M}_A \boldsymbol{\nu} \quad (2.49)$$

where $\mathbf{M}_A \in \mathbb{R}^{6 \times 6}$ is the added inertia matrix defined as

$$\mathbf{M}_A \triangleq - \begin{bmatrix} X_{\dot{u}} & X_{\dot{v}} & X_{\dot{w}} & X_{\dot{p}} & X_{\dot{q}} & X_{\dot{r}} \\ Y_{\dot{u}} & Y_{\dot{v}} & Y_{\dot{w}} & Y_{\dot{p}} & Y_{\dot{q}} & Y_{\dot{r}} \\ Z_{\dot{u}} & Z_{\dot{v}} & Z_{\dot{w}} & Z_{\dot{p}} & Z_{\dot{q}} & Z_{\dot{r}} \\ K_{\dot{u}} & K_{\dot{v}} & K_{\dot{w}} & K_{\dot{p}} & K_{\dot{q}} & K_{\dot{r}} \\ M_{\dot{u}} & M_{\dot{v}} & M_{\dot{w}} & M_{\dot{p}} & M_{\dot{q}} & M_{\dot{r}} \\ N_{\dot{u}} & N_{\dot{v}} & N_{\dot{w}} & N_{\dot{p}} & N_{\dot{q}} & N_{\dot{r}} \end{bmatrix} \quad (2.50)$$

where the matrix elements denote the hydrodynamic added masses. For many UUV applications, the vehicle is allowed to move at low speeds. If the vehicle is assumed to have three planes of symmetry, then \mathbf{M}_A and $\mathbf{C}_A(\boldsymbol{\nu})$ simplifies to

$$\mathbf{M}_A = -\text{diag}\{X_{\dot{u}}, Y_{\dot{v}}, Z_{\dot{w}}, K_{\dot{p}}, M_{\dot{q}}, N_{\dot{r}}\} \quad (2.51)$$

$$\mathbf{C}_A(\boldsymbol{\nu}) = - \begin{bmatrix} 0 & 0 & 0 & 0 & -Z_{\dot{w}}w & Y_{\dot{v}}v \\ 0 & 0 & 0 & Z_{\dot{w}}w & 0 & -X_{\dot{u}}u \\ 0 & 0 & 0 & -Y_{\dot{v}}v & X_{\dot{u}}u & 0 \\ 0 & -Z_{\dot{w}}w & Y_{\dot{v}}v & 0 & -N_{\dot{r}}r & M_{\dot{q}}q \\ Z_{\dot{w}}w & 0 & -X_{\dot{u}}u & N_{\dot{r}}r & 0 & -K_{\dot{p}}p \\ Y_{\dot{v}}v & X_{\dot{u}}u & 0 & -M_{\dot{q}}q & K_{\dot{p}}p & 0 \end{bmatrix} \quad (2.52)$$

Strip Theory

In order to estimate the hydrodynamic derivatives, i.e. added inertia matrix terms, strip theory is used. By dividing the submerged part of the vehicle into strips, the hydrodynamic coefficients can be computed for each strip and estimated over the length of the UUV to obtain three-dimensional results. For submerged slender vehicles the following formulas can be used to obtain the hydrodynamic coefficients

$$-X_{\dot{u}} = \int_{-L/2}^{L/2} A_{11}^{2D}(y, z) dx \approx 0.10m \quad (2.53)$$

$$-Y_{\dot{v}} = \int_{-L/2}^{L/2} A_{22}^{2D}(y, z) dx \quad (2.54)$$

$$-Z_{\dot{w}} = \int_{-L/2}^{L/2} A_{33}^{2D}(y, z) dx \quad (2.55)$$

$$-K_{\dot{p}} = \int_{-L/2}^{L/2} A_{44}^{2D}(y, z) dx \quad (2.56)$$

$$-M_{\dot{q}} = \int_{-L/2}^{L/2} A_{55}^{2D}(y, z) dx \quad (2.57)$$

$$-N_{\dot{r}} = \int_{-L/2}^{L/2} A_{66}^{2D}(y, z) dx \quad (2.58)$$

where L is the length of the vehicle, A_{22}^{2D} , A_{33}^{2D} and A_{44}^{2D} values are approximated using the values in Figure 2.3 depending on the UUV body type.

Two-dimensional hydrodynamic coefficients for roll, pitch and yaw angles can be found by

$$\int_{-L/2}^{L/2} A_{44}^{2D}(y, z) dx \triangleq \int_{-B/2}^{B/2} y^2 A_{33}^{2D}(x, z) dy + \int_{-H/2}^{H/2} z^2 A_{22}^{2D}(x, y) dz \quad (2.59)$$

$$\int_{-L/2}^{L/2} A_{55}^{2D}(y, z) dx \triangleq \int_{-L/2}^{L/2} x^2 A_{33}^{2D}(y, z) dy + \int_{-H/2}^{H/2} z^2 A_{22}^{2D}(x, y) dz \quad (2.60)$$

$$\int_{-L/2}^{L/2} A_{66}^{2D}(y, z) dx \triangleq \int_{-B/2}^{B/2} y^2 A_{11}^{2D}(x, z) dy + \int_{-L/2}^{L/2} x^2 A_{22}^{2D}(x, y) dz \quad (2.61)$$

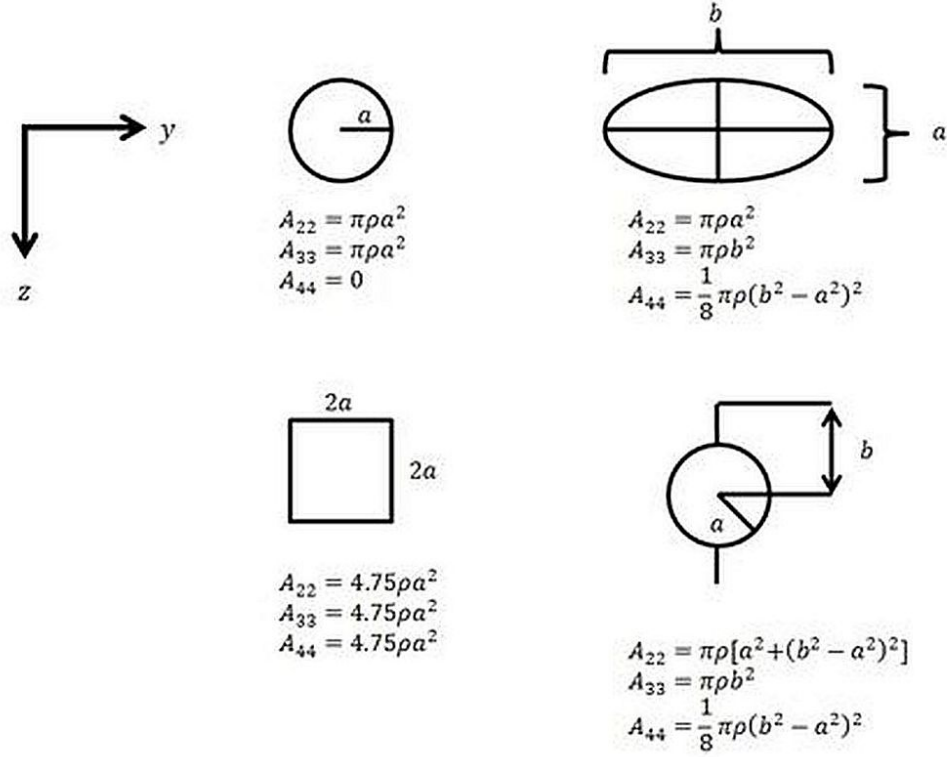


Figure 2.3: Two dimensional added mass coefficients used in strip theory.

B and H are the width and height of the vehicle, respectively. For other geometrical types of vehicles, more detailed analysis can be found in [64]. Another approach to estimate the hydrodynamic coefficients is to use hydrodynamic computation software such as, WAMIT, RESPONSE, SIMAN, MIMOSA, SIMO and WAVERES, etc. [65]

2.5.2 Hydrodynamic Damping

Hydrodynamic damping for marine vehicles is mainly caused by potential damping, skin friction, wave drift damping and vortex shedding. *Potential Damping* is the radiation-induced damping term encountered when a UUV body is forced to oscillate with the wave excitation frequency in the absence of incident waves. The contribution from potential damping is negligible in comparison to dissipative terms, such as viscous damping.

Skin Friction is due to laminar boundary layer when a UUV undergoes low-frequency motion. In addition to the linear skin friction, there is also quadratic skin friction effects

that should be taken into account during the design of the control system.

Wave-drift damping is additional resistance that surface vessels encounter and is not a dominant effect for UUVs.

Vortex Shedding is caused by frictional forces in a viscous fluid. The viscous damping force due to vortex shedding can be formulated as:

$$\mathbf{f}(\mathbf{U}) = -\frac{1}{2}\rho C_D(R_n)\mathbf{A}_i|\mathbf{U}_i|\mathbf{U}_i \quad (2.62)$$

where subscript $i \in 6\text{-DOF } x, y, z, \phi, \theta \text{ and } \psi$. U_i is the vehicle speed in the corresponding DOF, ρ is the surrounding water density, A_i is the projected cross-sectional area in water and $C_D(R_n)$ is the drag coefficient as a function of Reynolds number,

$$R_n = \frac{UD}{\nu} \quad (2.63)$$

Here, D is the characteristic length of the vehicle and ν is the kinematic viscosity coefficient (for salt water at 5°C with salinity 3.5%, $\nu = 1.5610^{-6}$). Quadratic drag in 6-DOF is expressed as shown in Morisons equation:

$$\mathbf{D}_M(\boldsymbol{\nu})\boldsymbol{\nu} = - \begin{bmatrix} |\boldsymbol{\nu}|^T \mathbf{D}_1 \boldsymbol{\nu} \\ |\boldsymbol{\nu}|^T \mathbf{D}_2 \boldsymbol{\nu} \\ |\boldsymbol{\nu}|^T \mathbf{D}_3 \boldsymbol{\nu} \\ |\boldsymbol{\nu}|^T \mathbf{D}_4 \boldsymbol{\nu} \\ |\boldsymbol{\nu}|^T \mathbf{D}_5 \boldsymbol{\nu} \\ |\boldsymbol{\nu}|^T \mathbf{D}_6 \boldsymbol{\nu} \end{bmatrix} \quad (2.64)$$

$D_i(i = 1...6) \in \mathbb{R}^{6 \times 6}$ depend on ρ , C_D and A . Thus each term in formula 2.64 is different.

2.5.3 Restoring Forces and Moments

The gravitational and buoyancy forces acting on a marine vehicle are referred to as restoring forces in the hydrodynamic terminology. f_G , the gravitational force, acts on the center of gravity $r_G = [x_G, y_G, z_G]^T$ while f_B , the buoyancy force, acts on the center of buoyancy $r_B = [x_B, y_B, z_B]^T$. For underwater vehicles, defining m as the mass of the vehicle and Δ as the volume of fluid displaced by the vehicle, g the gravitational acceleration and ρ as the fluid density, the submerged weight of the body is $W = mg$, and the buoyancy force is $B = g\Delta$. The weight and the buoyancy forces can be transformed into the body-fixed coordinate frame respectively, as

$$\mathbf{f}_G(\boldsymbol{\eta}_2) = J_1^{-1}(\boldsymbol{\eta}_2) \begin{bmatrix} \mathbf{0} \\ \mathbf{0} \\ W \end{bmatrix} \quad \mathbf{f}_B(\boldsymbol{\eta}_2) = -J_1^{-1}(\boldsymbol{\eta}_2) \begin{bmatrix} \mathbf{0} \\ \mathbf{0} \\ B \end{bmatrix} \quad (2.65)$$

The restoring force and moment vector can be expressed as:

$$\mathbf{g}(\boldsymbol{\eta}) = - \begin{bmatrix} \mathbf{f}_G(\boldsymbol{\eta}) + \mathbf{f}_B(\boldsymbol{\eta}) \\ \mathbf{r}_G \times \mathbf{f}_G(\boldsymbol{\eta}) + \mathbf{r}_B \times \mathbf{f}_B(\boldsymbol{\eta}) \end{bmatrix} \quad (2.66)$$

Expanding this expression results in

$$\mathbf{g}(\boldsymbol{\eta}) = \begin{bmatrix} (W - B)s\theta \\ -(W - B)c\theta s\phi \\ -(W - B)c\theta c\phi \\ -(y_G W - y_B B)c\theta c\phi + (z_G W - z_B B)c\theta s\phi \\ (z_G W - z_B B)s\theta + (x_G W - x_B B)c\theta c\phi \\ -(x_G W - x_B B)c\theta s\phi - (y_G W - y_B B)s\theta \end{bmatrix} \quad (2.67)$$

which is the Euler angle representation of the hydrostatic forces and moments. If a UUV is neutrally buoyant, then $W = B$. Defining the distance between the center of gravity r_G and

the center of buoyancy r_B as \overline{BG} such that:

$$\overline{BG} = [\overline{BG}_x, \overline{BG}_y, \overline{BG}_z]^T = [x_G - X_B, y_G - y_B, z_G - z_B]^T \quad (2.68)$$

Therefore, formula 2.67 simplifies to

$$\mathbf{g}(\boldsymbol{\eta}) = \begin{bmatrix} 0 \\ 0 \\ 0 \\ -\overline{BG}_y W c \theta c \phi + \overline{BG}_z W c \theta s \phi \\ \overline{BG}_z W s \theta + \overline{BG}_x W c \theta c \phi \\ -\overline{BG}_x W c \theta s \phi - \overline{BG}_y W s \theta \end{bmatrix} \quad (2.69)$$

2.6 Unmanned Underwater Vehicle Control and Stability

2.6.1 Proportional-Integral-Derivative (PID) Control

Most UUV systems, specifically Remotely Operated Vehicles (ROVs), utilize a series of single-input-single-output (SISO) PID controllers to control each DOF. This suggests the use of control gain matrices \mathbf{K}_p , \mathbf{K}_i and \mathbf{K}_d in the PID control law as follows:

$$\boldsymbol{\tau}_{PID} = \mathbf{K}_p \mathbf{e}(t) + \mathbf{K}_d \dot{\mathbf{e}}(t) + \mathbf{K}_i \int_0^t \mathbf{e}(\tau) d\tau \quad (2.70)$$

where, $\mathbf{e} = \boldsymbol{\eta}_d - \boldsymbol{\eta}$ is the tracking error, $\boldsymbol{\eta}_d$ denotes the vector of desired states and $\boldsymbol{\eta}$ denote the vector of measured states from the sensors. Throughout this research, $\boldsymbol{\eta}$ is referred to as the pose output obtained from the optical detector array as seen in Figure 2.4. Controller regulates the UUV motion based on the feedback obtained from the optical detector array and changes the course of the UUV by sending commands to the thrusters.

The control problems for the static-dynamic and dynamic-dynamic cases demonstrated in this research can be evaluated as a setpoint regulation problem in which the desired state

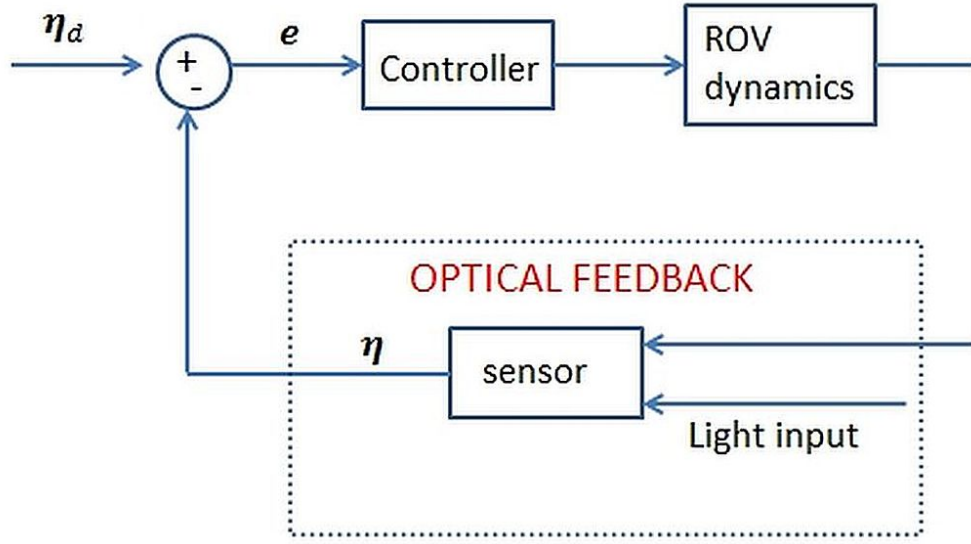


Figure 2.4: UUV Control Block diagram with the output obtained from optical feedback array.

vector $\boldsymbol{\eta}_d$ is constant. In the static-dynamic case, a UUV navigates to a position based on sensor feedback detection of the static light source. In the dynamic-dynamic case a follower UUV follows the changing path of a leader UUV.

In the setpoint regulation problem, PID control of a nonlinear square system is shown to guarantee local stability as follows [64]: The generalized momentum, \mathbf{p} , of a UUV is

$$\mathbf{p} = \mathbf{M}_\eta \dot{\boldsymbol{\eta}} \quad (2.71)$$

where \mathbf{M}_η is the mass represented in the Earth-fixed coordinate system. The inertia matrix \mathbf{M} represents the mass with respect to the body-fixed coordinate system such that

$$\mathbf{M}_\eta = \mathbf{J}^{-T}(\boldsymbol{\eta}) \mathbf{M} \mathbf{J}^{-1}(\boldsymbol{\eta}) \quad (2.72)$$

where \mathbf{J} is the transformation matrix relating the body and Earth-fixed coordinate systems (as discussed previously). A PID control law is taken to be of the following form:

$$\mathbf{u} = \mathbf{B}^{-1}[\mathbf{J}^T(\boldsymbol{\eta})(\mathbf{K}_p \mathbf{e} + \mathbf{K}_i \int_0^t \mathbf{e}(\tau) d\tau - \mathbf{K}_d \dot{\boldsymbol{\eta}}) + \mathbf{g}(\boldsymbol{\eta})] \quad (2.73)$$

In addition, a Lyapunov function candidate is given as

$$\mathbf{V}(\mathbf{x}) = \frac{1}{2} \mathbf{x}^T \begin{bmatrix} \mathbf{M}_\eta^{-1} & \alpha \mathbf{I} & \mathbf{0} \\ \alpha \mathbf{I} & \mathbf{K}_p & \mathbf{K}_i \\ \mathbf{0} & \mathbf{K}_i & \alpha \mathbf{K}_i \end{bmatrix} \quad (2.74)$$

where α small positive constant and \mathbf{x} is given as:

$$\mathbf{x} = [\mathbf{p}, \boldsymbol{\eta}, \int_0^t \mathbf{e}(\tau) d\tau]^T \quad (2.75)$$

Then, it can be shown that $\dot{\mathbf{V}} \leq \mathbf{0}$ and $\boldsymbol{\eta}$ converges to a constant $\boldsymbol{\eta}_d$ [64]. The PID control parameters \mathbf{K}_p , \mathbf{K}_i and \mathbf{K}_d are matrices that satisfy:

$$\mathbf{K}_d > \mathbf{M}_\eta \quad (2.76)$$

$$\mathbf{K}_i > \mathbf{0} \quad (2.77)$$

$$\mathbf{K}_p > \mathbf{K}_d + \frac{2}{\alpha} \mathbf{K}_i \quad (2.78)$$

Positive constant α is chosen such that it satisfies the following condition:

$$\frac{1}{2}(1 - \alpha)\mathbf{K}_d - \alpha\mathbf{M}_\eta + \frac{\alpha}{2} \sum_{i=1}^6 (\eta_i - \eta_{id}) \frac{\partial \mathbf{M}_\eta}{\partial \eta_i} > \mathbf{0} \quad (2.79)$$

Further details of this proof are given in [67].

2.6.2 Sliding Mode Control (SMC)

The dynamics of a UUV system can easily change when, for example, new sensor packages and tools are mounted on a UUV. The Sliding Mode Control (SMC) is a robust nonlinear control technique that is designed to address modeling uncertainties and has been previously employed in dynamic positioning of remotely operated vehicles [68]. The SMC, however, requires a priori knowledge of uncertainty bounds and assumes full-state feedback. In this study, SMC uses pose detection via an image moment invariants algorithm for full state sensor feedback (to be described in Chapter 5).

The SMC requires both position and velocity feedback. In the developed system, the detector array is able to provide the SMC with position/orientation feedback. However, for the velocity signals, the time derivatives of the pose signals are taken to obtain velocity data. Because UUV motion actuation in this study is restricted to be applied in a decoupled manner, the SISO system approach is taken for UUV SMC system design [69]. Therefore, five second-order controllers are designed rather than a single fifth-order controller such that:

$$x^n = \mathbf{b}(\mathbf{X}; t)[\mathbf{f}(\mathbf{X}; t) + \mathbf{U} + \mathbf{d}(t)] \quad (2.80)$$

where x^n is the n^{th} derivative of state x , U is the control input generated by the UUV propulsion system, $d(t)$ represents the potential disturbances (e.g., as wave and currents), $X = [x, \dot{x}, \dots, x^{n-1}]^T$ is the state vector of the system (i.e., the position, velocity and acceleration of the vehicle along a specified axis). $\mathbf{f}(\mathbf{X}; t)$ represents all lumped nonlinear functions in the system dynamics. For the follower UUV model used in this research, $\mathbf{f}(\mathbf{X}; t)$ includes all velocity-dependent effects including drag forces and inertia. For a second order system, $\mathbf{b}(\mathbf{X}; t)$ is the inverse of inertia.

The following simplified UUV model is used for pose detection for each of the 5-DOF of under interest for this study:

$$m\ddot{x} + c\dot{x}|\dot{x}| = u \quad (2.81)$$

where x is the state variable, m is the mass/inertia term (which includes added mass/inertia), c is the drag coefficient and u is the control input.

A time-varying surface $S(t)$ in the state space R^n is defined by the scalar equation $s(\mathbf{X}; t) = 0$ as in

$$S(\mathbf{X}; t) = \left(\frac{d}{dt} + \lambda\right)^{n-1} \tilde{x} \quad (2.82)$$

λ is a positive constant and tracking error \tilde{x} is defined such that $\tilde{x} = x - x_d$, where x_d denotes the desired state value. For a second order system (i.e., $n=2$), the sliding surface becomes

$$S(\mathbf{X}; t) = \dot{\tilde{x}} + \lambda\tilde{x} \quad (2.83)$$

where s is a weighted sum of position and velocity errors. $s(\mathbf{X}; t)$ corresponds to a line in the $\dot{\tilde{x}}$ vs \tilde{x} phase plane, having a slope λ .

The sliding condition is achieved when $\dot{s} = 0$, where the error trajectory \tilde{x} converges to the origin. For this, the derivative of the sliding surface is analyzed:

$$\dot{s} = \ddot{\tilde{x}} - \ddot{x}_d + \lambda\dot{\tilde{x}} \quad (2.84)$$

Combining formula 2.84 with the follower UUV model represented in formula 2.81 yields:

$$\dot{s} = -\frac{c}{m}\dot{x}|\dot{x}| + \frac{1}{m}u - \ddot{x}_d + \lambda\dot{\tilde{x}} \quad (2.85)$$

Setting $\dot{s} = 0$, an equivalent control law \hat{u} may be obtained to help achieve the sliding condition $\dot{s} = 0$ such that

$$\hat{u} = \hat{m}(\ddot{x}_d - \lambda\dot{\tilde{x}}) + c\dot{x}|\dot{x}| \quad (2.86)$$

In order to satisfy the sliding condition, a discontinuous term across the surface $s = 0$ is added to the \hat{u} term such that

$$u = \hat{u} - k1(s) \quad (2.87)$$

where $1(s)$ is a switching function and can be any odd function. Typically the signum function is used, but for this research, $1(s)$ is chosen to be the saturation function, $sat(s/\Phi)$, to eliminate the high frequency chattering that is inherent in the signum function and undesirable for UUV thruster actuation. (Here, Φ represents the boundary layer thickness of the switching function within which the switching function is smooth and linear.) The discontinuous switching gain, k , is chosen to be larger than the maximum bounded uncertainty such that

$$k(x) = (F + \beta\eta) + \hat{m}(\beta - 1)|\ddot{x}_d - \lambda\dot{\tilde{x}}| \quad (2.88)$$

where F is the estimation error bound on the nonlinear dynamics f , i.e. $|\hat{f} - f| \leq F$. β is the gain margin of the system, defined as

$$\beta = \sqrt{\frac{b_{max}}{b_{min}}} \quad (2.89)$$

where b_{min} and b_{max} are the minimum and maximum bounds on the control gain b in the system, i.e. $\ddot{x} = f + bu$. η is a strictly positive constant. In order to fully utilize the available control bandwidth, the control law is smoothed out in a time-varying thin boundary layer $\bar{k}(x)$ such that

$$\bar{k}(x) = k(x) - \dot{\Phi} \quad (2.90)$$

where Φ is the boundary layer thickness. Tuning Φ to represent a first-order filter of bandwidth λ ,

$$k(x_d) = \dot{\Phi} + \lambda\phi \quad (2.91)$$

Setting the gain margin, $\beta_d = \beta$, the switching term with time-varying thin boundary layer $\bar{k}(x)$ is expressed as

$$\bar{k}(x) = k(x) - k(x_d) + \frac{\lambda\Phi}{\beta_d} \quad (2.92)$$

Finally, the resulting control input u is

$$u = \hat{u} - \bar{k}(x) \text{sat}(s/\Phi) \quad (2.93)$$

An SMC for a Multiple-Input-Multiple-Output (MIMO) UUV 6-DOF system is shown to be stable in the sense of Lyapunov as follows [70]: Defining a Lyapunov-like function candidate $\mathbf{V}(\mathbf{s}, t)$:

$$\mathbf{V}(\mathbf{s}, t) = \frac{1}{2} \mathbf{s}^T \mathbf{M}^* \mathbf{s} \quad (2.94)$$

where $\mathbf{M}^* = \mathbf{J}^{-T} \mathbf{M} \mathbf{J}^{-1}$, the time derivative of the Lyapunov function is

$$\dot{\mathbf{V}} = \mathbf{s}^T \mathbf{M}^* \dot{\mathbf{s}} + \frac{1}{2} \mathbf{s}^T \dot{\mathbf{M}}^* \mathbf{s} - \mathbf{s}^T \mathbf{C}^* \mathbf{s} + \mathbf{s}^T \mathbf{C}^* \mathbf{s} \quad (2.95)$$

Incorporating the 6-DOF nonlinear UUV equations of motion as in formula 2.81 and assuming that the number of control inputs is greater than or equal to the number of controllable DOF,

$$\dot{\mathbf{V}} = -\mathbf{s}^T (\mathbf{D}^* + \mathbf{K}_D) \mathbf{s} + (\mathbf{J}^{-1} \mathbf{s})^T (\tilde{\mathbf{M}} \ddot{\mathbf{q}}_r + \tilde{\mathbf{C}} \dot{\mathbf{q}}_r + \tilde{\mathbf{g}}) - \mathbf{k}^T |\mathbf{J}^{-1} \mathbf{s}| \quad (2.96)$$

where $\tilde{\mathbf{M}} = \hat{\mathbf{M}} - \mathbf{M}$, $\tilde{\mathbf{C}} = \hat{\mathbf{C}} - \mathbf{C}$, $\tilde{\mathbf{D}} = \hat{\mathbf{D}} - \mathbf{D}$, $\tilde{\mathbf{g}} = \hat{\mathbf{g}} - \mathbf{g}$ and \mathbf{q}_r denotes a virtual reference vector. Defining the switching term k_i as

$$k_i \geq |\tilde{M}\ddot{q}_r + \tilde{C}(\dot{q}\dot{q}_r) + \tilde{D}(\dot{q}\dot{q}_r) + \tilde{g}(x)|_i + \eta_i \quad (2.97)$$

where $\eta_i > 0$ as defined previously

$$\dot{V} \leq -s^T(D^* + K_D)s - \eta^T(J^{-1}s) \leq 0 \quad (2.98)$$

The dissipative matrix $D > 0$ and the gain matrix $K_D \geq 0$ results in

$J^{-T}DJ^{-1} + K_D > 0$. For a more detailed explanation of proof of stability, the reader is referred to [70].

CHAPTER 3

CHARACTERIZATION OF OPTICAL COMMUNICATION IN A LEADER-FOLLOWER UUV FORMATION

As part of the research to develop an optical communication design of a leader-follower formation between Unmanned Underwater Vehicles (UUVs), this chapter presents light field characterization and design configuration of the hardware required to allow the use of distance detection between UUVs. Without loss of generality, the research in this chapter specifically targets communication between Remotely Operated Vehicles (ROVs). The following contributions are made in this chapter:

1. The light field produced from a light source mounted on a leader UUV is empirically characterized and modeled.
2. Based on the light field measurements, a photo-detector array for the follower UUV is designed.
3. Evaluation of the communication algorithms to monitor the UUVs motion is conducted through underwater experiments in the Jere A. Chase Ocean Engineering Laboratory at the University of New Hampshire.
4. The optimal spectral range was determined based on the calculation of the diffuse attenuation coefficient by using two different light sources and a spectrometer.
5. The range between the leader and the follower vehicles for a specific water type is determined.

6. The array design and the communication algorithms were modified according to the results from the light field.

3.1 Introduction

Preliminary work for this study includes the development of a control design for distance detection of UUV using optical sensor feedback in a Leader-Follower formation [47]. The distance detection algorithms are designed to detect translational motion above water utilizing a beam of light for guidance. The light field of the beam is modeled using a Gaussian function as a first-order approximation. This light field model is integrated into nonlinear UUV equations of motion for simulation to autonomously and actively regulate the distance between the leader and the follower vehicles to an *a priori* specified reference value. A prototype design of a photo-detector array consisting of photodiodes is constructed and tested above water. However, before an array can be mounted on the bow of a follower UUV, a better understanding of the underwater light is needed. The proposed system is based on detecting the relative light intensity changes on the photodiodes in the array. The size of the array strictly depends on the size of the ROV.

This chapter provides an overview on the experiments and simulations conducted to adjust the algorithms based on underwater conditions. Underwater light is attenuated due to the optical characteristics of the water, which are constantly changing and are not uniformly distributed. As a result, applying distance detection algorithms underwater adds complexity and reduces operational ranges. Experimental work in this study was performed in the wave and tow tank at the Jere A. Chase Ocean Engineering facilities.

3.2 Theoretical Background

The basic concept for optical communication in this chapter is based on the relative intensity measured between the detectors within the photo-detector array mounted on the follower ROV. In addition to the beam pattern produced by the light source, the intensity

of light underwater follows two basic concepts in ocean optics [71]: The Inverse Square Law and Beer-Lambert Law.

3.2.1 Beam pattern

The light field emitted from a light source can be modeled by various mathematical functions. In addition, there are a variety of light sources that can be used underwater that differ in their spectral irradiance (e.g., halogen, tungsten, and metal-halide). The spectral characteristics of the light source are an important issue that affects the illumination range, detector type and the detection algorithms. As in the case of the light sources, the photodetectors also have a spectral width in which their sensitivity is at a maximum value. By determining the spectral characteristics of the light source, it is possible to select the detector and filters for the photodetector array. We assume that the beam pattern can be modeled using a Gaussian function. This representation is valid for a single point light source. The Gaussian model used in this study can be represented as follows [72]:

$$I(\theta_i) = Ae^{-B\theta_i^2} \quad (3.1)$$

In (3.1), I is the intensity at a polar angle, θ_i where the origin of the coordinate system is centered around the beam direction of the light source. A and B are constants that describe the Gaussian amplitude and width respectively in Figure (3.1).

3.2.2 Inverse Square Law

According to the Inverse Square Law, the intensity of the light is inversely proportional to the inverse square of the distance from the light source:

$$I = \frac{S}{4\pi r^2} \quad (3.2)$$

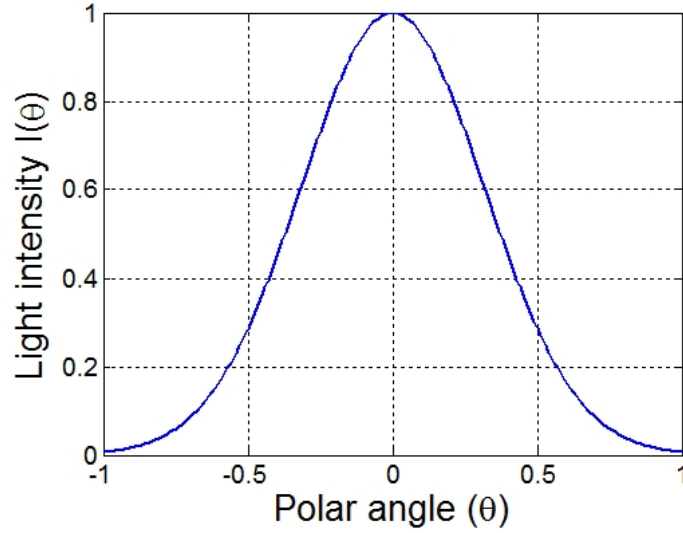


Figure 3.1: Light intensity as a function of polar angle θ .

where I is the intensity at r distance away from the source and S is the light field intensity at the surface of the sphere. Thus, the ratio of the light intensities at two different locations at the same axis can be expressed

$$\frac{I_1}{I_2} = \frac{\frac{S}{4\pi r_1^2}}{\frac{S}{4\pi r_2^2}} = \left(\frac{r_2}{r_1}\right)^2 \quad (3.3)$$

The light field S generated by a light source is assumed to show uniform illumination characteristics in all directions. In addition, the light intensity is such that the light source is assumed to be a point source and that its intensity is not absorbed by the medium. It should also be noted that although the Inverse Square Law is the dominant concept in the development of control algorithms, for this research this law is not the only dominant optical mechanism that affects the light passing in water. As light travels through water, its rays also get absorbed by the medium according to the Beer-Lambert law.

3.2.3 Beer-Lambert law

Beer-Lambert law states that radiance at an optical path length l in a medium decreases exponentially depending on the optical length, l , the angle of incidence, θ_i , and the attenuation coefficient, K [34]: Beer-Lambert Law describes light absorption in a medium under the assumption that an absorbing, source-free medium is homogeneous and that scattering is insignificant.

When light travels through a medium, its energy is absorbed exponentially as in

$$L(\zeta, \hat{\xi}) = L(0, \hat{\xi}) \exp\left(-\frac{\zeta}{\mu}\right) \quad (3.4)$$

where L denotes the radiance, ζ the optical depth, $\hat{\xi}$ the direction vector, and μ denotes the light distribution as a function of angle θ_i such that:

$$\mu = \cos \theta_i \quad (3.5)$$

l , (i.e. the optical path length in direction μ),

$$dl \equiv \frac{d\zeta}{\mu} = \frac{K(z)dz}{\mu} \quad (3.6)$$

where $K(z)$ is the total beam attenuation coefficient and dz is the geometric depth.

In this chapter, an experimental setup is built such that the incidence angle θ_i is zero. As a result, combination of formula (3.4) and formula (3.6) results in :

$$L(\zeta, \hat{\xi}) = L(0, \hat{\xi}) \exp(-K(z)dz) \quad (3.7)$$

3.3 Experimental Test Platform

Experimental work in this study to evaluate a proposed hardware design is based on ocean optics and hardware restrictions for a given ROV system. The experiments include

beam diagnostics, spectral analysis and intensity measurements from several light sources. These experiments are conducted in the Tow and Wave Tank at the UNH Jere A. Chase Ocean Engineering facilities. The wave and tow tank has a tow carriage that moves on rails. A light source is mounted on a rigid frame to the wall in the tow tank and a light detector is placed underwater connected to a tow carriage (Figure 3.2). This experimental setup is based on the design configured by [71]. To characterize the interaction between the light source and the light array a 50 Watt halogen lamp powered by 12 V power source is used. For the detector unit, a spectrometer (Ocean Optics Jaz) is used to characterize the underwater light field. These empirical measurements are used to adjust the detection algorithms and are also to be used in the design of a photo-detector array. The light source in the tank simulates a light source that is mounted on the crest of a leader ROV. The design of the photo-detector array simulates the array that is to be mounted on the bow of the corresponding follower ROV. The photo-detector array design depends on the size of the ROV and the light field produced by the light source mounted on the leader ROV. In this case, the size for an optical detector module is kept at 0.4 m, which is the width dimension of the UNH ROV (built by senior design team 2014 summer) test platform, a small observation class ROV.

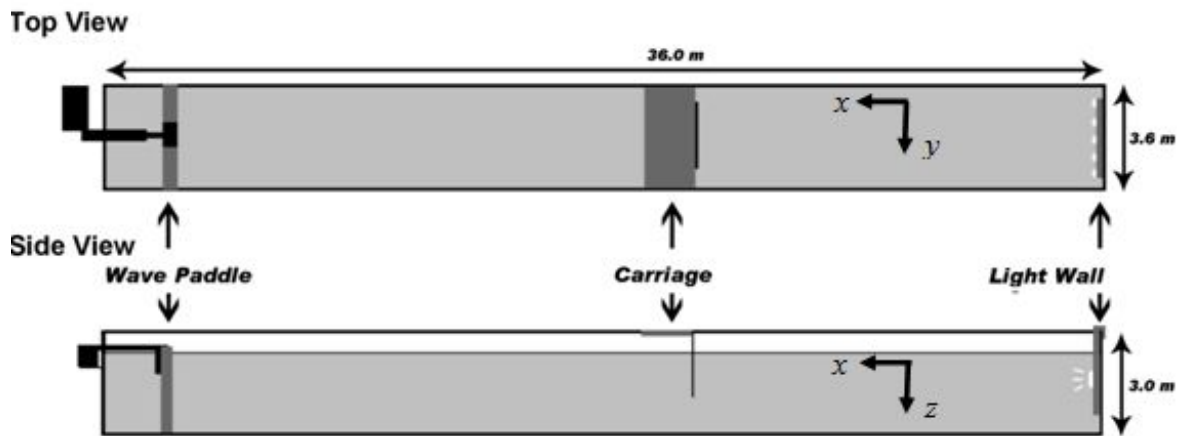


Figure 3.2: Experimental schematic of UNH tow tank.

Translational experiments in 1-D and 3-D motion (i.e., motion along and perpendicular to

the center beam of the light source) are conducted in air and in water. The goals for the 1-D experiments are to characterize the spectral properties of the water and to determine the best spectral ranges for optical communication between ROVs. In this underwater experiment, a submerged fiber optic cable with a collimator is connected to a spectrometer and is vertically aligned based on the peak value of radiance emitted from the light source. This alignment is considered the illumination axis (x -axis). The radiance emitted from the light source through the water column was empirically measured by the spectrometer at distances ranging from 4.5 to 8.5 m at 1 m increments. The spectrometer is configured to average 40 samples with an integration time of 15 milliseconds. A 2° collimator is used to restrict the spectrometer field of view and to avoid the ambient effects of stray light rays reflecting off the tank walls or from the water surface.

The experimental setup in air is very similar, where the spectrometer is mounted on a tripod and aligned to the peak value of radiance at the illumination axis (x -axis) (Figure 3.2). Because such light sources produce heat at high temperatures (up to 700°C) that can damage the waterproof fixing, the experimental setup in air requires that the light source be submerged in an aquarium during operation. Similar to the underwater experiments, the same distances between the light source and the spectrometer, including the offsets, remain fixed.

The 3-D translational underwater experiments utilize the same setup as that of the underwater 1-D experiments where additional radiance measurements are conducted along a normal axis (z -axis) that is located on a plane normal to the illumination axis (x -axis). In the 3-D translational experiments, fixed distances along the illumination axis between the light source and the spectrometer (i.e., 4.5 to 8.5 m) are held constant where additional measurements are conducted along the normal axis at 0.1 m increments ranging from 0 m to 1 m. As mentioned in Section 3.2, it is assumed that the light source produces a beam pattern that can be modeled as Gaussian. Accordingly, the radiance measurements along the normal axis are assumed to be axisymmetric. The experimental setups for 3-D underwater

experiments can be seen in Figure 3.3.

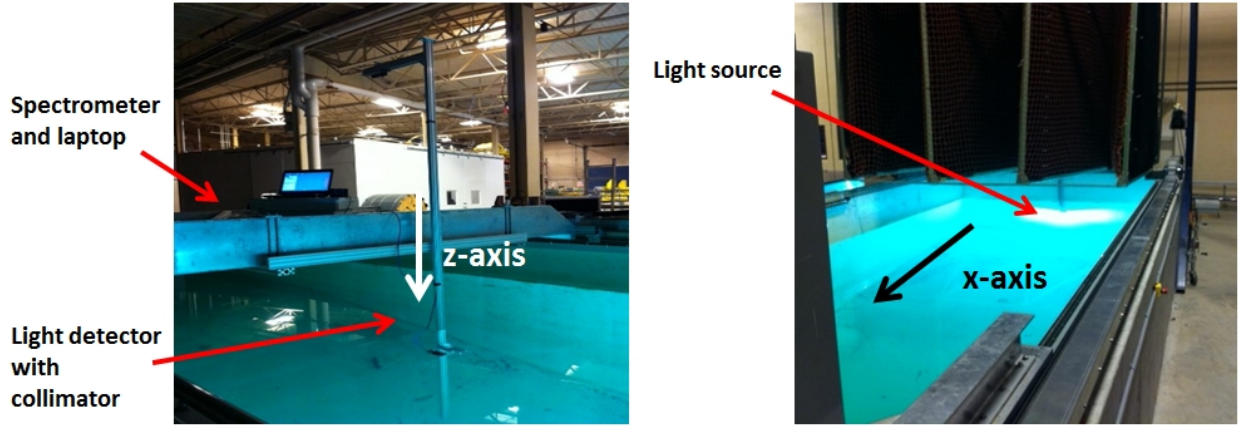


Figure 3.3: Experimental Setup for translational 3-D underwater experiments. (Left) spectrometer unit and its connections. (Right) transmitting unit mounted to the wall of the tank.

3.4 Optical Characterization Results

attenuation underwater causes a significant loss of radiant energy over increasing distances. The diffuse attenuation coefficient, K , is used as a parameter to calculate the decrease of energy from the light source to the target. In this study, the diffuse attenuation coefficient is used to determine the spectral range of the light source and determine the photo-detector types that can be utilized in the array. For successful optical communication up to ranges of 9 m, the ideal spectral ranges are to be maintained such that the diffuse attenuation coefficient values are smaller than 0.1 m^{-1} . At this distance, light signal loses about half its energy. As a first-order approximation, the diffuse attenuation coefficient values are assumed constant throughout the water column. This assumption reduces the number of parameters used in the distance detection algorithms and, thus, the expected processing time used in implemented controls applications. In the study, the diffuse attenuation coefficient values are calculated for a 50 W light source. In Figure 3.4, the percentage loss curve for various distances is shown.

Diffuse attenuation was calculated based on formula (3.7). Measurements taken at a specific distance in water and in air are compared in order to account for the Inverse Square Law. Light that travels in air also undergoes diffuse attenuation but it is ignored in this case as the diffuse attenuation in air is negligible compared to in water. These values suggest that the UNH wave tank where the experiments are conducted contains algae and dissolved matter. The study results suggest that 500-550 nm band-pass filters in the range should be used in the detector unit to provide better performance when applying distance detection algorithms.

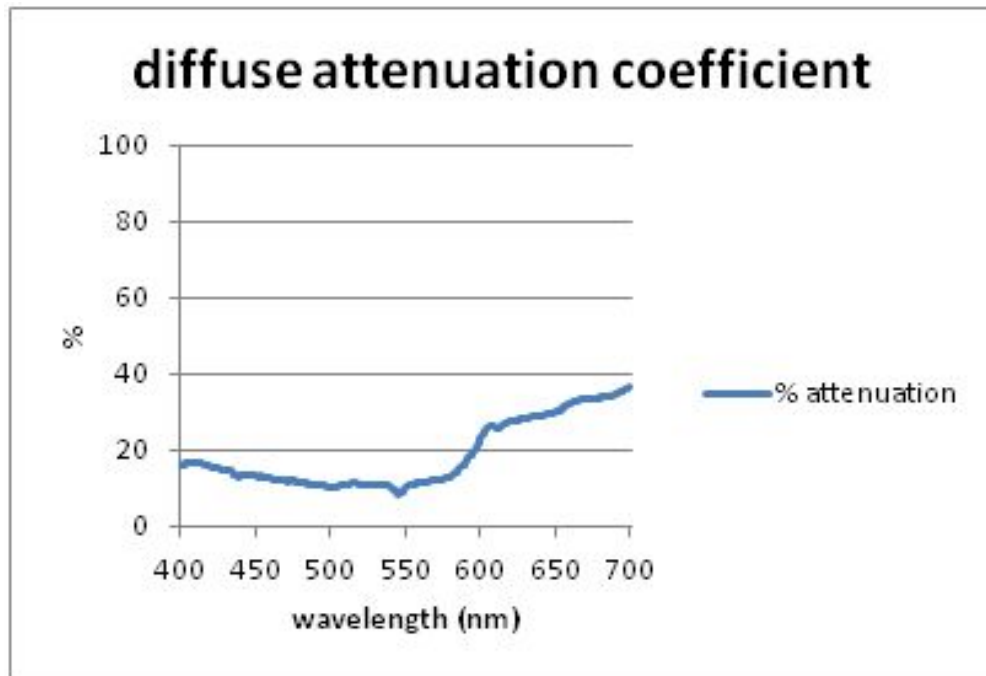


Figure 3.4: Diffuse attenuation graph.

Based on the light attenuation results, the distance between the leader and the follower vehicles was calculated. The intensity readings are collected between 500-550 nm and averaged. In Figure 3.5 the experimental values are compared with the theoretical values. Blue diamonds represent the experimental data and the green triangles represent the theoretical calculations from taking the Inverse Square and Beer-Lambert Laws. The readings are normalized and the measurement at 4.5 m is used as the reference measurement to normalize the

intensity. The experimental results show that algorithm performance of the algorithms in the UNH water tank is expected to decrease after 8.5 m where this range, the light intensity cannot be distinguished from the background noise levels (i.e., $\pm 20\%$).

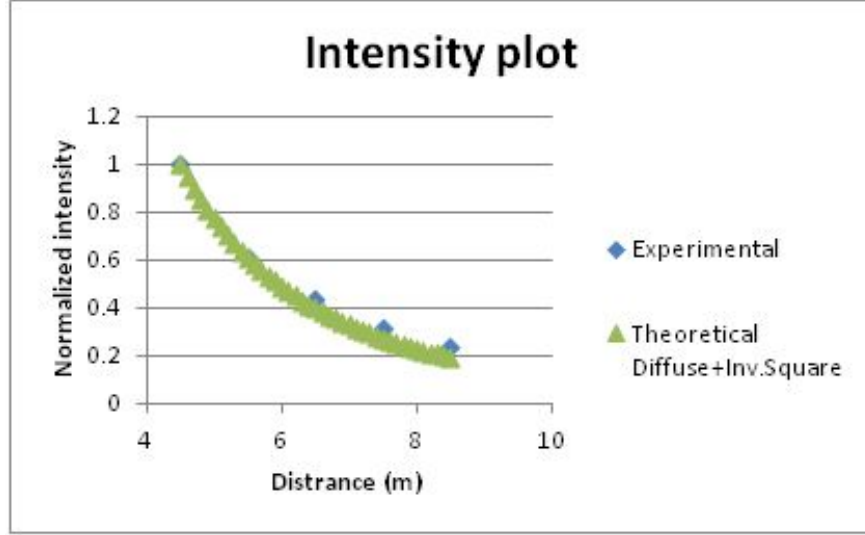


Figure 3.5: The intensity vs. distance plot.

The light profile calculated from the 3-D experiments agrees with the assumption that the pattern of the light beam can be described using a 2-D Gaussian fit as seen in Figure 3.6. The measurements were collected from 0 to 1.0 m at x-axis and at 4.5 m at the illumination axis for 50 W light source. The measurements between 500-550 nm are averaged. Using a 50% intensity decrease as a threshold, the effective beam radius from the center (i.e., the illumination axis) is 0.3 m. Another key finding obtained from the 3-D experiments is the dimensions of the light detector array. It can be seen that if the length of the array is kept at 0.6 m, then different light detector elements can detect the light intensity change, which is useful for implemented control algorithms. It should be noted that the physical characteristics of the photo-detector array such as dimensions and the spacing between the array elements, strictly depend on beam divergence.

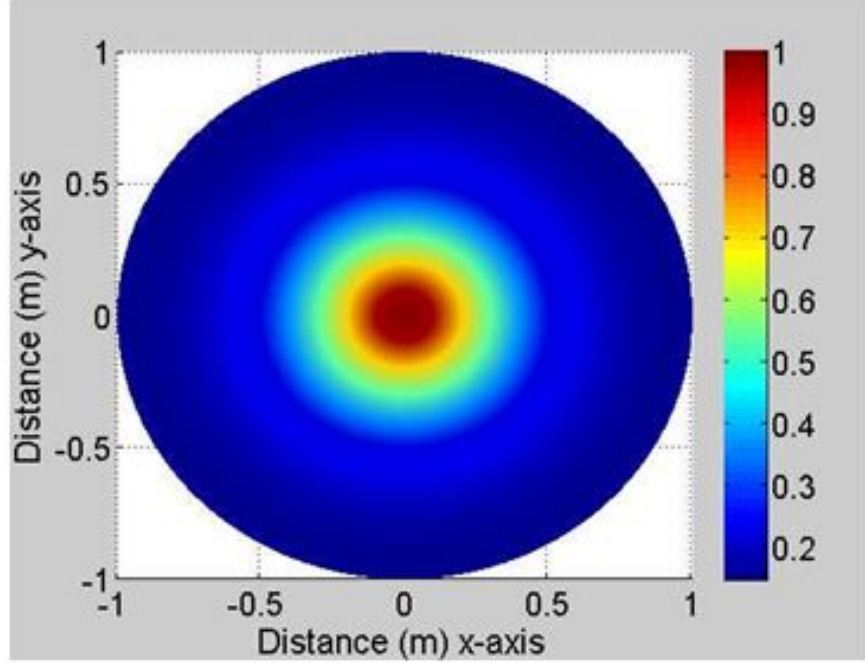


Figure 3.6: Plot of the cross-sectional beam pattern. The measurements were collected from 0 to 1.0 m at x -axis and at 4.5 m at the illumination axis for 50 W light source. The measurements between 500-550 nm are averaged.

3.5 Optical Characterization Discussion and Conclusions

The optical characterization results provide valuable environmental information for modifying a photo-detector array design according to light field. According to the diffuse attenuation, a 500-550 nm band-pass filter allows the same observation of the light field from a single source as a 2-D Gaussian beam pattern. At this spectral range is around 0.1 m^{-1} , the peak power of the beam (along the z -axis) changes from 100% to 23% as the array moves away from light from 4.5 m to a distance of 8.5 m, respectively. The size of the beam pattern is a function of the divergence angle of the beam. In the current configuration, the Full-Width-at-Half-Maximum (FWHM) radius expands from 0.3 m to 0.4 m as the array moves away from light from 4.5 m to a distance of 8.5 m. The beam divergence can be modified using reflectors and optic elements in case more acute changes in the light field are needed over a shorter distance of 0.4 m, which is the maximum length of the array. It is also found that the maximum operational distance between UUVs is 8.5 m for practical application

using the existing hardware.

During the empirical measurements in the UNH Tow Tank depth, several error sources are identified that limit an accurate correlation between the models and its corresponding measurements. These errors include underwater alignment and measurement errors. Although the frame mounting all the elements is rigid and aligned, the internal alignment of the light source and of the detectors may not have been aligned perfectly along one axis. As a result, the profile measurements of light along the z -axis and the along the xy -plane might be slightly skewed. Another factor is the water turbidity. Obtaining an accurate calculation of water turbidity in a survey site is very challenging. Therefore, for more accurate distance detection algorithms, water turbidity should be taken into account. The focus of the current study emphasizes 3-D translational motion, but future work will involve extending the research to characterize rotational motion.

CHAPTER 4

OPTICAL DETECTOR ARRAY DESIGN FOR NAVIGATIONAL FEEDBACK BETWEEN UUVs

Designs for an optical sensor detector array for use in autonomous control of Unmanned Underwater Vehicles (UUVs), or between UUVs and docking station, are demonstrated in this chapter. Here, various optical detector arrays are designed for the purpose of determining and distinguishing relative 5 degree-of-freedom (DOF) motion between UUVs: 3-DOF translation and 2-DOF rotation (pitch and yaw). In this chapter, a numerically based simulator is developed in order to evaluate varying detector array designs. The underwater optical communication methods reported in the literature are shown to be able to measure only up to 3-DOF, as opposed to the UUVs full maneuvering capabilities in all 6-DOF. Multiple DOF motion is necessary to determine the relative orientation between two or more UUVs or between a UUV and a docking platform. Therefore, the design of an optical detector array for such an application becomes crucial. This chapter compares planar and curved array designs for underwater optical detection between UUVs or between a UUV and a docking station. The comparison between the two types of arrays is conducted using a simulator that models a single-beam light field pattern for a variety of motion types (i.e., 3-DOF translation and 2-DOF rotation). In addition, the number of elements in the array and the possible noise sources from experimental hardware and the environment are also taken into account. The results from the simulator are validated using *in situ* measurements conducted in underwater facilities at the Jere A. Chase Ocean Engineering Laboratory and are to be used for the design of an optical detector unit for UUVs and the development of

translational and rotational detection and control algorithms.

4.1 Optical Design Considerations

The performance criteria for an optical detector array design suitable for underwater communication between UUVs can be judged by two characteristics. The first is the ability of the detector array to provide a unique signature, that is, a sampled image that represents a given location and orientation of a UUV with respect to a transmitter (i.e., light source). The second characteristic is the minimum number of required optical detector components. This characteristic is derived from the fact that a UUV should have a timely response to fast changes in UUV motion. Here, a smaller number of detectors simplifies the hardware design and reduce processing time. A unique signature, an image footprint from the optical detectors, enables a UUV to receive the necessary feedback to help the on-board control system determines appropriate control commands to maintain a specified/desired orientation with respect to and distance from a beacon (or any other object of interest).

The idea behind an optical detector array is such that as this array, which is mounted on a UUV, comes in contact with (without loss of generality) a guiding beam, the light field is sampled and a signature of the light beam can be obtained. Here, the light source represents a guide that is mounted on a leader UUV or on a docking station. In this research, a single light source is used as the guiding beam for the detector array. The light field generated from the light source is approximated as a Gaussian beam at a given solid angle. For large arrays (i.e., arrays with several individual detectors), the light signature can be further represented as an image.

The design considerations for an optical detector array can be categorized as environmental and hardware-related. In this research, the primary hardware for such a module consists of optoelectronic array components (e.g. photodiodes). These components are framed in a specific configuration and are mounted to an appropriate area on a UUV. A planar array is an array of optical detectors that are mounted on a flat, 2-dimensional frame. Although

the optical detectors can be placed in any configuration, a traditional equidistant design is assumed (without loss of generality) for the sake of simplicity. The detector, furthermore, is assumed to be square, having an equal number of vertical and horizontal elements (Figure 4.1a)). The planar array simplifies the design and the resulting light signature, which is a cross-sectional (and possibly rotated) view of and within the light field. A curved array is an array of optical detectors that are mounted on either a spherical or parabolic frame. The geometry of the frame (curvature and oblateness) provides a larger range of incidence angles between the detectors and the light field. In this study, all elements of the curved array are equidistant in a plane projection and located at a fixed distance from the geometric center of the frame (Figure 4.1b)).

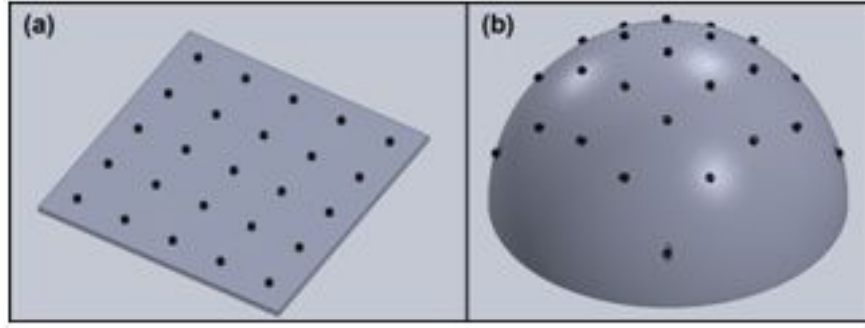


Figure 4.1: Schematic illustration of array designs used in the simulator: (a) Planar array and (b) Curved array.

4.1.1 Environmental Considerations

The light source in this study is assumed to be a point source with peak radiance $L_0(r = 0, \rho = 0, \Delta\lambda)[W/m^2 - sr - nm]$ for a given detector with a fixed aperture area and a spectral range of $\Delta\lambda$. Using a cylindrical coordinate system, the axial distance from the light source to the optical element along the beam axis is defined as r and the radial distance from the beam axis is defined as ρ (Figure 4.2).

Assuming that light is not absorbed or scattered by the water medium, radiance collected by a detector is inversely proportional to the square of the distance to the source. The

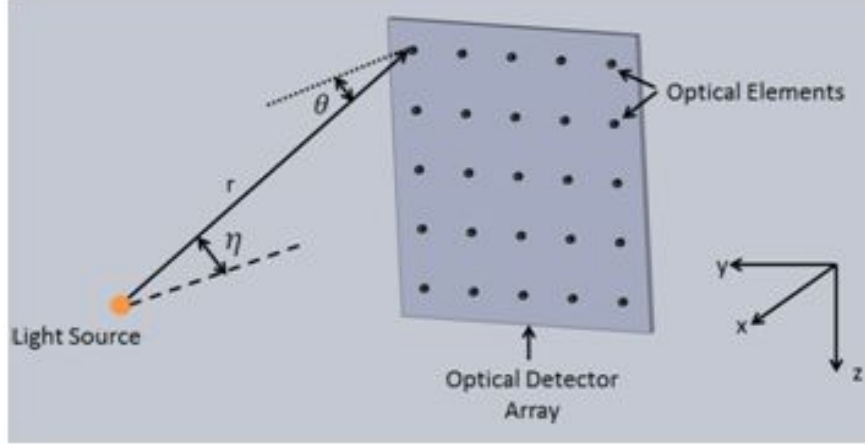


Figure 4.2: Optical detector array and relevant optical angles, the solid line representing the light ray reaching a detector, the dashed line represents the optical axis and the dotted line represents the normal to the array.

location for half-the-peak intensity from the light source, Δr_{half} , along the beam axis is assumed to be relatively small. The radiance from the light source according to the inverse-square law can be defined as:

$$L_{obs}(r, 0, \Delta\lambda) = L_o(0, 0, \Delta\lambda) \left(\frac{\Delta r_{half}}{r} \right)^2 \quad (4.1)$$

Alternatively, the radiance change from one location, r_1 , to a second location, r_2 , along the beam axis can be expressed using

$$L_{obs}(r_1, 0, \Delta\lambda) = L_o(r_2, 0, \Delta\lambda) \left(\frac{r_2}{r_1} \right)^2 \quad (4.2)$$

The beam pattern produced from the intersection of a Gaussian beam light field with a plane that is perpendicular to the transmission direction can be described using a Gaussian function. Traditionally, the beam pattern is described using length terms with the peak intensity value at the intersection point of the beam axis with the plane ($\rho = 0$) [73]:

$$L_{obs}(r, \rho, \Delta\lambda) = L_o(0, 0, \Delta\lambda) \left(\frac{\Delta r_{half}}{r} \right)^2 e^{-\left(\frac{2\rho^2}{W^2(r)} \right)} \quad (4.3)$$

where, $W(r)$ is the radial distance of the beam width on the plane at a beam intensity of $1/e^2$ of the peak value at a distance r from the light source.

A description of the beam pattern angular terms is applied with a relationship $\rho = r \tan(\eta_b)$, where η_b is the angle between the beam axis and the light ray reaching the detector. In addition, the root-mean-squared (RMS) width of intensity distribution, which is half of the beam width, $\sigma_\rho = 0.5W(r)$, is also converted to an angular relationship such that $\sigma_\rho = \tan^{-1} \left(\frac{\sigma_\rho}{r} \right)$. Using small-angle approximation, the exponent term can be represented

$$e^{\left(-\frac{2\rho^2}{W^2(r)}\right)} = e^{\left(-\frac{r^2 \tan^2 \eta_b}{2r^2 \tan^2 \sigma_{\eta_b}}\right)} \cong e^{\left(-\frac{2\eta_b^2}{2\sigma_{\eta_b}^2}\right)} \quad (4.4)$$

Light in water is also attenuated by absorption and scattering. Environmental background noise, denoted by L_b , from light scattering in the water column may occur. This attenuation can be described using Beer-Lambert Law [74], which states that radiance decreases exponentially through the medium as a function of distance, r , from the source and the diffuse attenuation coefficient $K(\Delta\lambda)$. The attenuated radiance at each detector is

$$L_{att}(r, \eta, \Delta\lambda) = L_{obs}(r, \eta, \Delta\lambda) - L_b e^{\left(-\frac{2K(\Delta\lambda)r}{2 - \eta^2}\right)} + L_b \quad (4.5)$$

Environmental background noise caused by the interaction between the light beam and the water medium has been previously modeled. These studies that have investigated the interaction of light beams through turbulent medium (e.g., [75], [76], [77]) approximate the background noise using a blurring function applied to the light beam. For this research, the background noise is modeled using a Hanning window:

$$h(n) = 0.5 \left(1 - \cos \left(\frac{2\pi n}{N_w - 1} \right) \right) \quad (4.6)$$

where, N_w , denotes the size of the Hanning window and n is the sample number in the window, i.e. $0 \leq n \leq N_w - 1$. The Hanning window is convolved with the output image

generated by the optical elements.

4.1.2 Hardware Considerations

As light interacts with a detector element (e.g., photodiode) in the array, photons from the light are absorbed by the detector and current is generated. The current is then manipulated by the signal conditioning circuitry into a digital signal using an analog-to-digital converter (ADC). The strength of the electrical signal measured by the detector is dependent on the intensity (i.e., the optical power) of the light beam and on the detector's responsivity (i.e., the electrical output of a detector for a given optical input). Also, noise sources produced in the hardware can make it difficult to extract useful information from the signal. The quality of the detector is characterized by the minimum intensity value that can be detected. The key hardware noise sources are: signal shot noise σ_s , background shot noise, σ_b , dark-current shot noise, σ_{dc} , Johnson noise, σ_j , amplifier noise, σ_j , and ADC-generated quantization noise, σ_q . All sources of hardware noise are assumed to be mutually independent. Furthermore, it is assumed that all noise can be approximated as Gaussian with corresponding values of standard deviation. Accordingly, these noise sources may be combined as a root sum of squares and represented with a net noise current:

$$\sigma_n = \sqrt{\sigma_s^2 + \sigma_b^2 + \sigma_{dc}^2 + \sigma_j^2 + \sigma_q^2} \quad (4.7)$$

In addition to the electro-optical characteristics of the array component, the geometrical design of the array also affects the received intensity of the light signal. The incidence angle, θ , of the light ray reduces the level of radiance measured by the detector according to Lambert's Cosine Law:

$$L_\theta(r, \eta, \Delta\lambda) = L_n(r, \eta, \Delta\lambda) \cos(\theta) \quad (4.8)$$

where L_n is the radiance at the surface normal.

4.2 The Simulator

Based on the hardware and environmental considerations, a simulator (an analytical test bed) is developed. The goal of the simulator is to analyze varying array designs for UUV optical detection of relative translation and rotation with respect to a reference coordinate frame. The criteria in evaluating the effectiveness of a detector array design includes:

1. Determining the minimum number of detector elements required for robust UUV position and attitude determination
2. Verifying that the detector is able to acquire a unique signature for each UUV position/orientation combination with respect to the given light source.

The simulator calculates light intensities at the individual optical elements based on the relative geometry between the light source and the detector. The simulator also takes into account the environmental and hardware effects described in the previous section. The effective operational distance for underwater communication is dependent on water clarity. Although a broad spectral range of light (400 to 700 nm) can be used for optical communication, the radiation calculation in the simulator uses a narrower spectral range (between 500 to 550 nm), providing maximum transmittance in clear to moderately clear waters. Based on empirical measurements using a 400 W metal halide lamp [71] and a commercial grade Mounted Silicon Photodiode photodetector, a maximum operational distance of up to 20 m is assumed for extremely clear waters, which represent open ocean conditions ($K = 0.05m^{-1}$), up to 8 m for moderately clear waters, which represent tropical coastal waters ($K = 0.1m^{-1}$). Although the simulator can provide results for larger angles, pitch and roll angles are limited to within 20° . This constraint is based on the assumption that most UUVs are built to be stable about their pitch and roll axes of rotation, e.g. [78], [79], [80], [81]]. The simulator input parameters and the flow diagram are presented in Appendix A.

4.2.1 The Simulator Reference Frames

In the simulator, an Earth-fixed reference frame is assumed, where a light source is centered at the origin (0,0,0). Several coordinates are identified in the x - y - z coordinate frame with respect to the UUV Center of Mass (COM). Several attitude orientations are also identified with respect to the Earth-fixed reference frame and defined by Euler angles ϕ , θ , and ψ for roll, pitch, and yaw, respectively. In order to ensure appropriate sensor feedback for adequate control performance [47], the detector array must be able to detect a unique light signal (pattern) for each combination of coordinate positions and attitude orientations. Furthermore, this detection must be accurate to within 0.2 m of the true COM coordinate position and within 10° of the true attitude orientation within 4 m-8 m range in x -axis.

The array geometry is chosen based upon the dimensions of the UUV. The UUV in this study is assumed to be a rigid body of box-type shape with both a width (starboard to port) and height (top to bottom) of 0.4 m and a length (from bow to stern) of 0.8 m, the size of a generic observation-class ROV used as a test platform in this research. Accordingly, the width and height of the detector array are 0.4 m x 0.4 m for both planar and curved array designs. The adapted coordinate axes convention is that of the Tait-Bryan angles [82]. Here, the x -axis points toward the bow and the y -axis towards starboard. The body-fixed z -axis points downward and completes the orthogonal triad as shown in Figure 4.2. In this study, the follower is assumed to undergo rotation about all three-axes, i.e., pitch, roll and yaw. The coordinates associated with the array detectors are transformed into that of the leader UUV via an appropriate attitude rotation matrix.

4.2.2 Array Geometry

As previously mentioned, two array shapes are compared in this study:

1. a planar array
2. a curved array

The geometry of both arrays is defined in this section.

In the planar detector array, the detectors are defined relative to the UUV COM with respect to the local (body-fixed) coordinate frame. The center and the four corners of the planar array frame are defined as

$$Arr_{center} = (COM_x + \frac{l}{2}, COM_y, COM_z) \quad (4.9a)$$

$$Arr_{min(y),max(y)} = COM_y \pm \frac{w}{2} \quad (4.9b)$$

$$Arr_{min(z),max(z)} = COM_z \pm \frac{h}{2} \quad (4.9c)$$

where COM_x , COM_y and COM_z respectively define the x , y and z coordinates of the follower COM, l is the length of the UUV, and w and h denote the width and the height of the vehicle, respectively. The lateral and vertical spacing (denoted as p_y and p_z ,) between the individual detectors on the array can be expressed as:

$$p_y = \frac{w}{N-1} \quad (4.10a)$$

$$p_z = \frac{h}{N-1} \quad (4.10b)$$

It is assumed that the detector array is an $N \times N$ square where N is the number of optical elements. That is, the number of detectors in the rows and columns of the array are the same. Accordingly, the detector spacing is also the same (i.e. $p_y = p_z$). It is important to note that for a curved array, p_y and p_z are projected detector spacing.

A hemispherical shape is used for the curved array. The number of detectors in the curved array is initially defined based on the $N \times N$ planar array design. Then, if the detectors are

projected onto the hemispheric surface, as in Fig 4.1b, with a fixed radius r :

$$x_{ij} = \sqrt{r^2 - y_{ij}^2 - z_{ij}^2} \quad (4.11)$$

where x_{ij} is the position of the detector element on the x -axis and y_{ij} and z_{ij} are the coordinates of the array that is projected onto the bow of the follower UUV. i and j are the indices that represent the row and column number of the array,. In this study, the radius, r , of the hemisphere (of the curved array) is 0.32 m and is defined from its focal point, F , which is the center of the hemisphere:

$$F_x = COM_x + \frac{l}{2} \quad (4.12a)$$

$$F_y = COM_y \quad (4.12b)$$

$$F_z = COM_z \quad (4.12c)$$

The main difference between the planar and curved array designs is that all of the optical elements in the planar array are oriented in the same direction, while the detectors in the curved array are normal to the surface of the array frame and thus allow a larger range of incidence angles.

4.2.3 Radiometry

The construction of a realistic light field (as measured by the array detectors) is based on the radiometric and hardware considerations for each detector (Section 4.2). The radiometric calculations are based on the distance (i.e., inverse square law and Beer's law) and orientation (Lambert's cosine law) of each detector with respect to the light source. Using the detector's characteristics and the associated electronics, the artificially created incident light is numerically converted into a digital signal. For the array simulator in this study,

the specifications of two types of photodiodes are used as reference (Thorlabs SM05PD1A, Thorlabs SM05PD2A). The resulting electronic signal is represented as a 10-bit (0-1023) sensor output value (thus, introducing quantization error). Environmental background noise is artificially added to the signal using a Hanning window of size $N_w = 11$. Also, a random net noise current of $\sigma_n = 10^{-6}$ is added to the electronic signal. The final digital signal is used to generate an image pattern which, in turn, is to be used by the array detectors to identify the position and the orientation of the UUV.

4.3 Results

4.3.1 Simulator Results

The success of the simulator relies on the ability of the array to provide a unique image for every UUV position/orientation combination. In order to process the simulator output images more efficiently, the output data is reduced to a few key image parameters, allowing for a multi-parameter comparison. These chosen few parameters describe the beam pattern and allow the use of simple algorithms that do not require significant computational effort. One such algorithm is the Spectral Angle Mapper (SAM) [83], which is the dot product between sets of key parameters extracted from two images that are represented as vectors, $U(u_1, u_2, \dots, u_{np})$ and $V(v_1, v_2, \dots, v_{np})$:

$$\alpha = \cos^{-1} \left(\frac{\vec{U}_t \vec{V}_t}{\|\vec{U}_t\| \|\vec{V}_t\|} \right) \quad (4.13)$$

The calculated angle between the two vectors, i.e. SAM angle α , is the numerical resemblance between the images. Two very similar images result in an angle value close to 0° , whereas two very different images result in an angle close to 90° . The SAM angle provides a good performance evaluation indicator to the different types of array detector geometries tested using a single-value parameter.

Although the UUV is a 6-DOF system, it is assumed that it is not possible to achieve

relative roll angle detection (because of axial symmetry about the body x -axis). Thus, only five parameters are provided to the simulator as input: translation along all three coordinate axes, rotation of the pitch angle, θ , and rotation of the yaw angle, ψ . Accordingly, the image output of the simulator is analyzed using five parameters that can be related to input parameters (Figure 4.3): the peak light intensity value, I , the corresponding location of the horizontal detector, j , and vertical detector, k , at peak intensity, the location of the skewness of the horizontal intensity profile gradient, S_{kh} , and skewness of the vertical intensity profile gradient, S_{kv} . The peak value is normalized with respect to a given maximum detectable intensity ($0.0 < I < 1.0$). The locations of the horizontal and vertical detectors are defined with respect to the central detector ($j = \frac{N+1}{2}$, $k = \frac{N+1}{2}$). Based on the location of the peak intensity, the slopes of the horizontal and vertical intensity are calculated. The slope of the profile is used rather than the profile itself as the slope also provides the directionality of the beam profile (i.e., negative or positive) in addition to the asymmetry of the profile. The images and the corresponding parameters for the planar and the curved array of size 21 x 21 for a given coordinate location and yaw rotation are shown in Figure 4.3 and Figure 4.4, respectively.

4.3.2 Detector Array Comparison

As a first step for the selection of the array design, the geometry of the detector array is evaluated. A performance evaluation between planar and curved arrays is conducted, where each detector array contains a 21 x 21 grid of detector elements with a detector spacing of 0.02 m. Both detector arrays are evaluated for their ability to detect changes in position and orientation, i.e., changes in SAM angle, α . Changes in position are evaluated as the UUV translates along the y -axis from a given origin (0 m) to an offset of 0.9 m in 0.03 m increments. Similarly, changes in orientation are evaluated by rotating the UUV about the z -axis, yaw rotation, from its initial reference (0°) to 30° in increments of 1° . Figure 4.5 represents the resemblance results to identify UUV positional and attitude changes based on

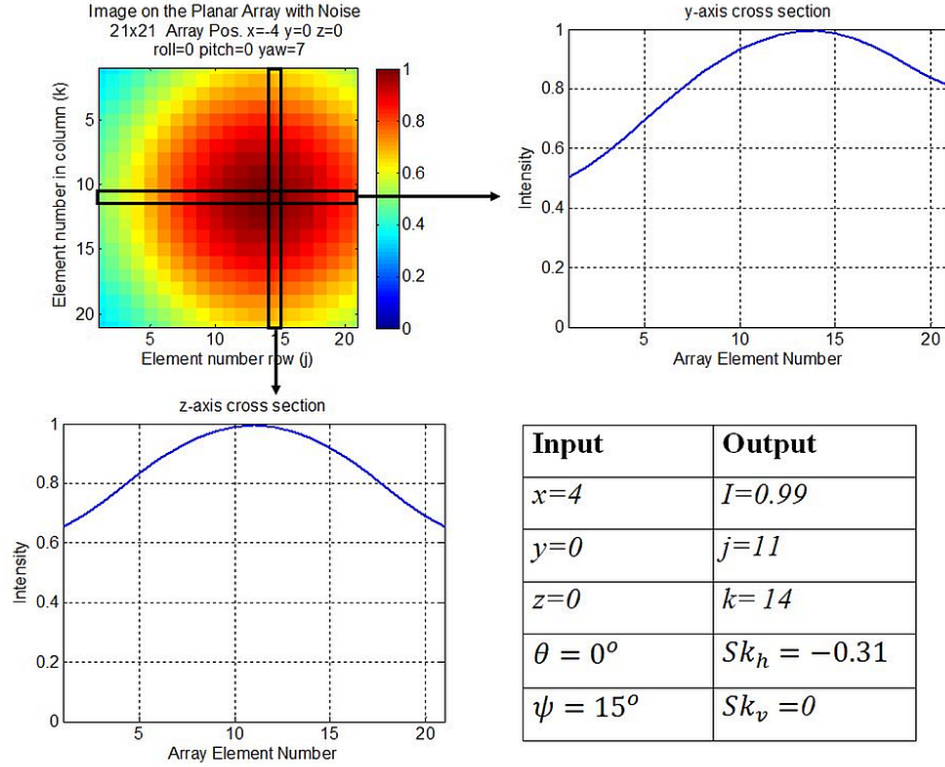


Figure 4.3: Key image parameters and intensity profiles for a planar array with hardware and environmental background noise: (top left) Output image from the simulator, (top right) Horizontal intensity profile, (bottom left) Vertical intensity profile, (bottom right) Input values used to generate output image and key parameters describing output image.

measured signals (images) collected by the detector array at 4 m. The comparative results for changes in position using the SAM algorithm show similar performance between the two array geometries, where the curved array performs slightly better (2°) at shifts greater than 0.6 m. However, an investigation of the results for changes in orientation reveals that the curved array is more sensitive to changes in orientation than the planar array. The SAM angle results for the curved array show changes of 12° at 5° yaw rotations and changes of 22° at 10° rotations, whereas the results for the planar array show changes in SAM angle of 5° at 5° yaw rotations and 11° at 10° rotations. Based on these results, it is deduced that the curved array geometry is more suitable for distinguishing changes in position and, especially, orientation of a UUV platform with respect to a reference light beacon.

After the geometry of the detector array is defined, relationships between the ability to

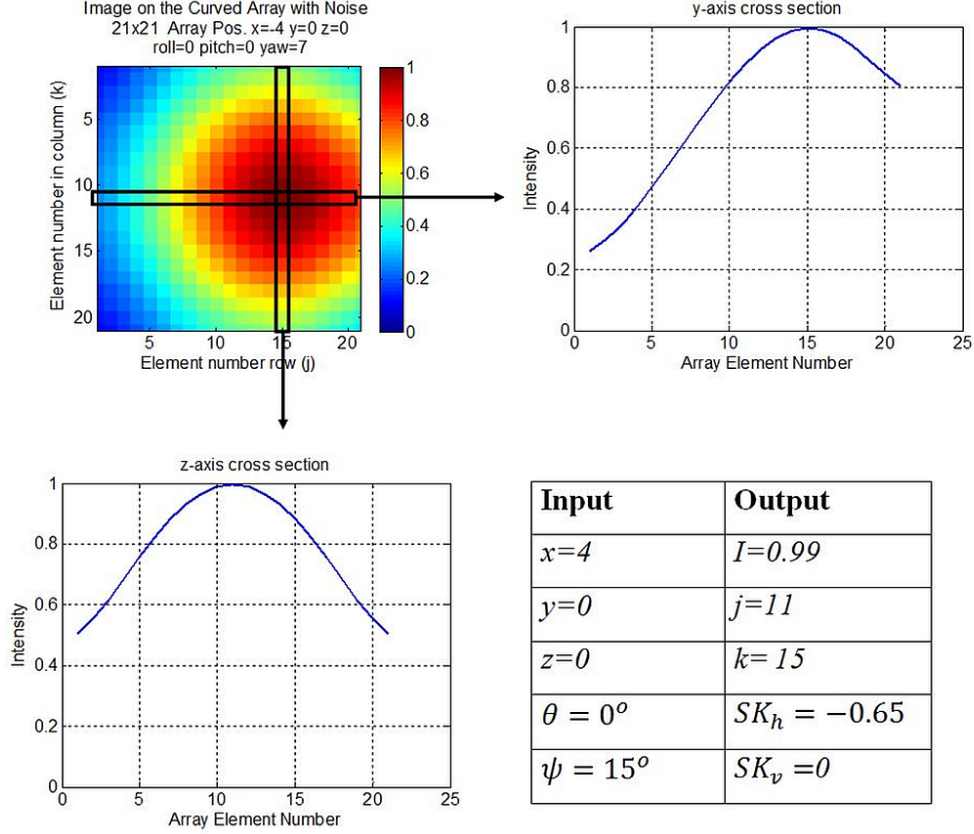


Figure 4.4: Key image parameters and intensity profiles for a curved array with hardware and environmental background noise: (top left) Output image from the simulator, (top right) Horizontal profile, (bottom left) Vertical profile, (bottom right) Input values used to generate output image and key parameters describing output image.

distinguish changes in position and orientation from the output images and the number of elements in the curved detector array are evaluated. The comparisons include different array sizes, ranging from a 3 x 3 size array up to a 101 x 101 size array at distances ranging from 4 m to 8 m to the light source. The comparative results at 4 m (Figure 4.6) show that changes in positional and rotational shifts can be detected by an array with the size of at least 5 x 5 optical elements with detector spacing of 0.1 m. Based on a threshold of a 15° SAM angle, a smaller array would fail to detect translational shifts smaller than 0.2 m or rotational changes smaller than 10°. It should also be noted that no significant changes in detection capability are observed for array sizes greater than 7 x 7 with a detector spacing of 0.067 m. The effect of operational distances greater than 4 m is shown in Figure 4.7.

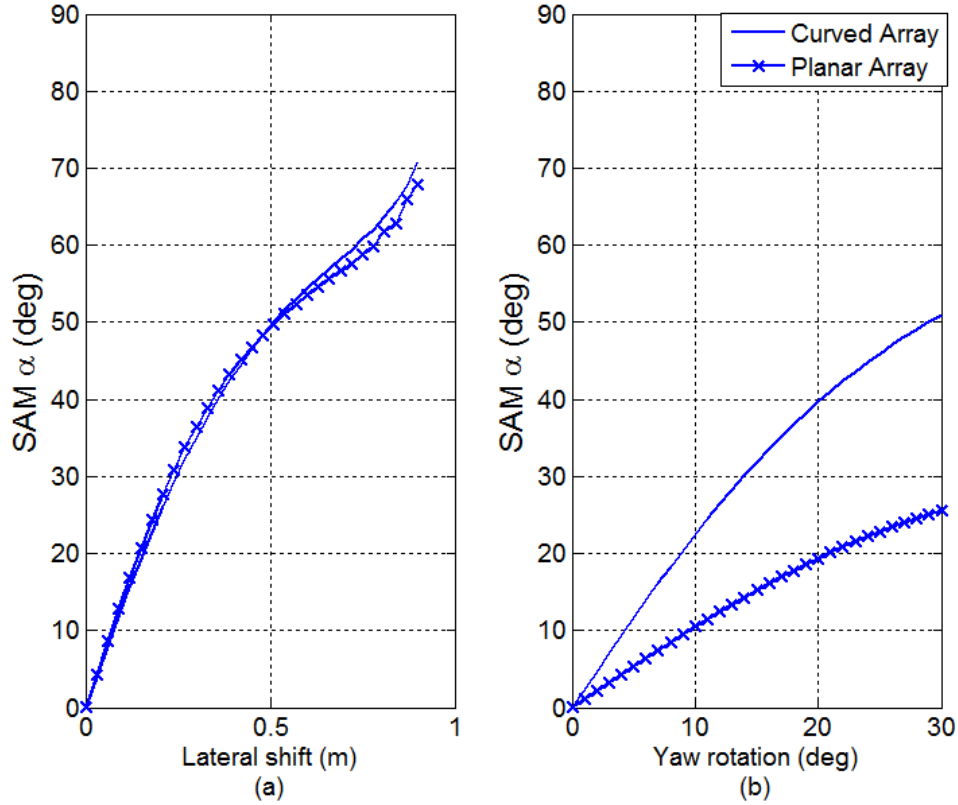


Figure 4.5: Comparative resemblance results (SAM angles) for 21 x 21 element curved and planar array (at x=4m) as a function of: (a) lateral translation, (b) yaw rotation.

Although the ability of the curved array to distinguish between the images decreases as the operational distance increases, the SAM algorithm results for 5 x 5 array at 8 m are still above 10° for a 10° yaw rotation and above 6° for 0.2 m translation.

4.3.3 Experimental Confirmation

In addition to the analytical study presented in this chapter, experimental validations are conducted at the Jere A. Chase Engineering building wave and tow tank. The underwater experiments compare the simulator outputs to that of empirical measurements. This comparison validates the optical model used in the simulator (i.e., Gaussian beam profile) and confirms the environmental physical properties that contribute to the light field as received by the detector array. As shown in Chapter 3, the light source in this study is a 400 W

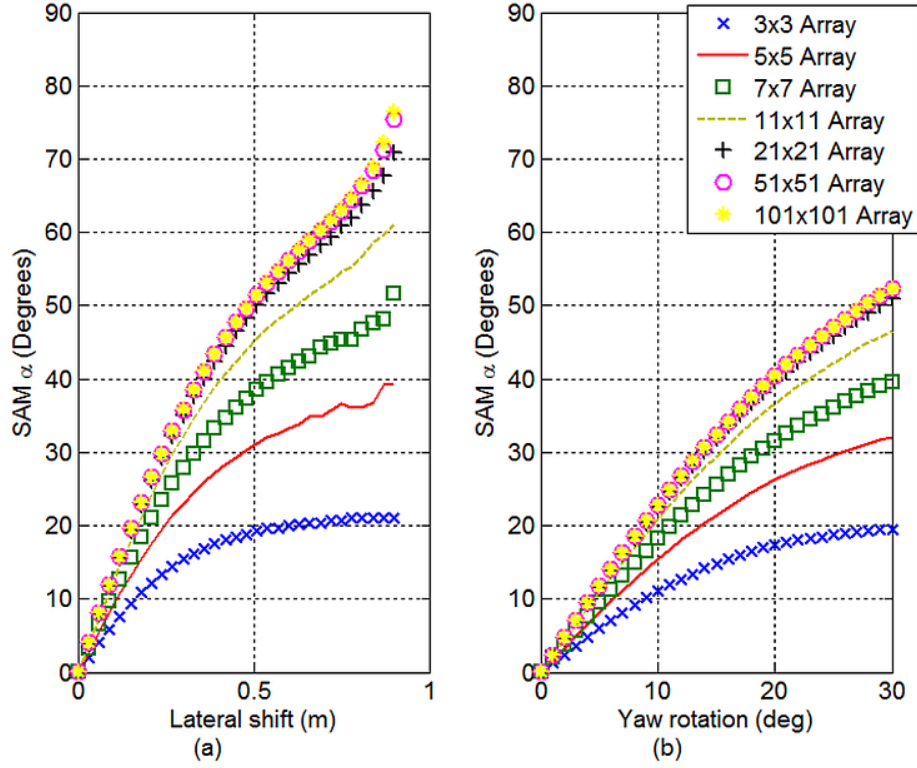


Figure 4.6: Comparative resemblance results (i.e., SAM angle) with respect to varying array sizes (incorporating environmental and background noise): (a) Under lateral motion (b) Under angular rotation.

underwater halogen lamp (contained in a waterproof fixture). Profiles of light intensity data (radiance measurements) are collected via a spectrometer such that the measurements are perpendicular to that of the illumination axis. The profiles are collected at distances ranging from 4 m to 8 m at 1 m increments and with lateral shifts from the illumination axis up to 1 m away from the axis at 0.1 m increments.

The profiles from empirical measurements are compared to profiles produced from simulator output images calculated for the same distance and orientation conditions (Figure 4.8). The measured profiles confirm that the light field calculations for the simulations are valid. Although the background noise in the simulated models is overestimated, the correlation, R^2 , between the two profiles is between 0.95-0.99 for distances from 4-8 m.

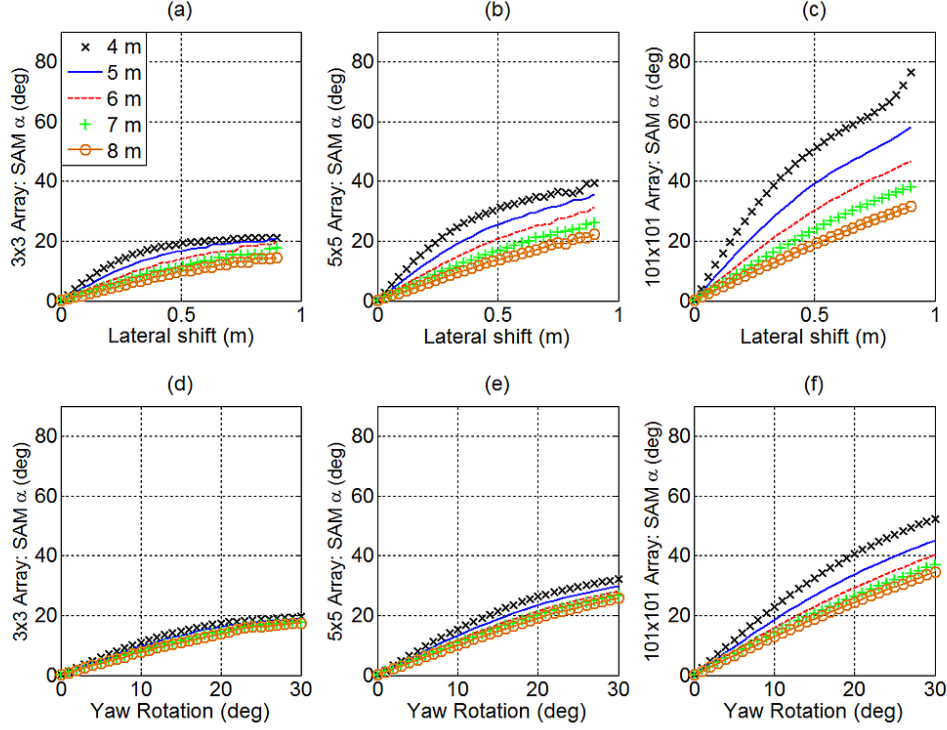


Figure 4.7: Comparative resemblance results (i.e., SAM angle) with respect to operational distance (incorporating environmental and background noise): (a-c) lateral shift, (d-f) yaw rotation - (a, d) 3 x 3 array (b, e) 5 x 5 array (c, f) 101 x 101 array with spacing of 0.2 m, 0.1 m and 0.004 m, respectively.

4.4 Discussion of Detector Array Design and Numerical Simulator

The results of this study show that the detector array simulator is a useful and reliable tool for array design in optical communication between UUVs or between a UUV and a docking station. The simulator has a modular design to allow for the addition and changing of hardware and environmental parameters. Although the simulator can evaluate other array geometries with a variety of sizes, only two traditional shapes are considered. The simulator results show that a curved array with a minimum array size of 5 x 5 elements is sufficient for distinguishing positional changes of 0.2 m and rotational changes of 10°. For the distinction of smaller changes, a larger array size is required.

A follower UUV is assumed to have 5-DOF maneuverability with respect to a given light source: three DOF translations (i.e., translations along the x , y , and z -axes) and 2-DOF

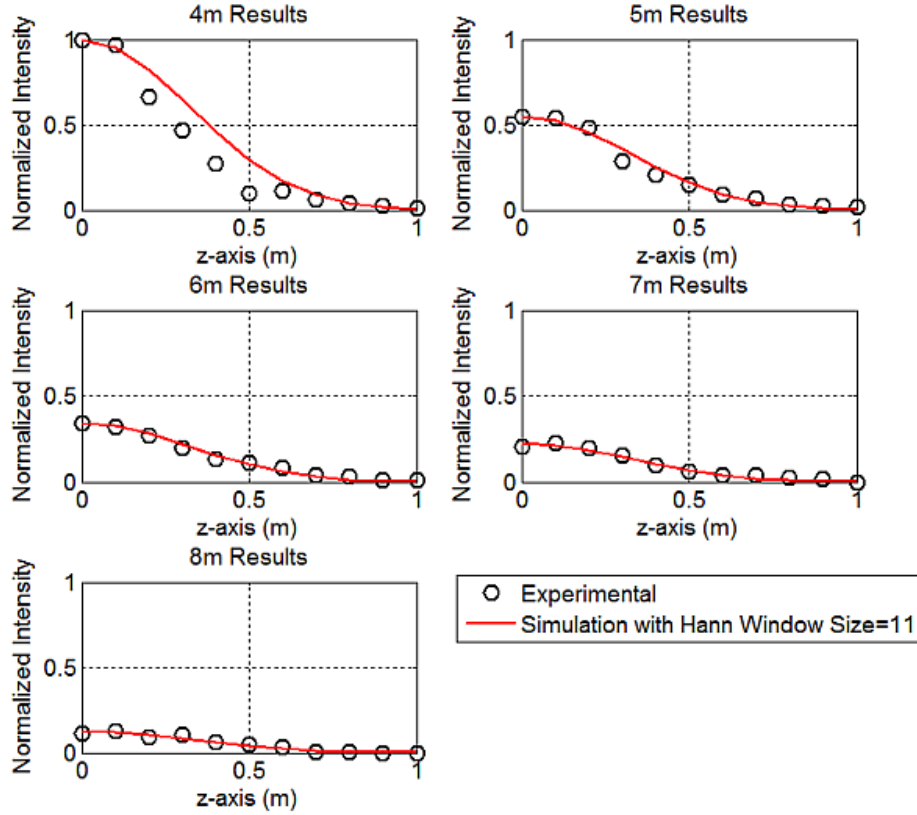


Figure 4.8: Comparison of Experimental and Simulation results (a) 4 m (b) 5 m (c) 6 m (d) 7 m (e) 8 m.

rotations (yaw and pitch). It is not possible to decouple roll changes (rotation about the body-fixed x -axis) from either pitch or yaw. This is due to the axial symmetry of the light beam. However, the use of multiple light sources or a light source with a unique intensity distribution may enable roll rotation sensing.

It is important to note that the simulator assumes that the water column is uniform with systematic background noise. As a result, the output images of the light field intersecting with the detector array resemble a Gaussian beam pattern. However, disturbances in the medium (e.g., sediment plume) may cause the beam pattern to be distorted. This point should be taken into account in the development of control algorithms for UUV navigation. Otherwise, the control algorithms may misinterpret the acquired image and direct the fol-

lower UUV away from the guiding beam. The simulator results show that detector noise does not contribute significantly to the image output. Other detectors with a larger noise level may contribute more to output images.

An alternative hardware component that may be considered instead of photodetectors is a camera array. The potential benefits using COTS cameras (CCD or CMOS) is to provide additional spatial information that can potentially enhance the performance of pose detection algorithms. However, one of the requirements for an autonomous system is the ability to process the sensors input and execute the pose detection algorithms fast enough to respond to changes in the UUVs dynamics (i.e., detection of the leader UUV and a response by the follower UUV). It seems that a camera array that performs image extraction and processing procedures may not be sufficiently fast for the UUV interaction. With that said, the camera array option is considered for future work and for applications that allow for slower update rates of pose detection algorithms.

CHAPTER 5

POSE DETECTION AND CONTROL ALGORITHMS FOR DYNAMIC POSITIONING OF UUVs VIA AN OPTICAL SENSOR FEEDBACK SYSTEM

The use of an optical feedback system for pose detection of Unmanned Underwater Vehicles (UUVs) for the purpose of UUV dynamic positioning is investigated in this chapter. The optical system is comprised of a curved optical detector array (on board the UUV) of hemispherical geometry that is used to detect the relative pose between an external light source and the UUV. This pose detection is accomplished in two ways: via SAM algorithm and via image moment variants. These two methods are also compared to a traditional image processing algorithm, phase correlation and log-polar transform. In this chapter, analytical simulations are conducted to test the efficacy of feedback controllers (Proportional-Integral-Derivative, Sliding Mode Control) using the optical feedback system and a previously developed numerical simulator. The resulting dynamic positioning and control performance of a UUV is observed in two simulated control scenarios:

1. a static-dynamic (regulation control) system in which the UUV autonomously positions itself via 4-DOF (translational control in addition to yaw/heading control) with respect to a fixed external light source
2. a dynamic-dynamic (tracking control) system where one UUV tracks another independent UUV (via translational control in 3-DOF).

In these simulations, the numerical simulator takes into account environmental conditions (water turbidity and background noise) and hardware characteristics (hardware noise

and quantization). Simulation results show proof of concept for this optical-based feedback control system for both the static-dynamic and dynamic-dynamic cases.

5.1 Introduction

As a first step to investigate positioning and coordinated formation of UUVs using optical communication, a detector array interface, i.e. a numerical simulator is designed based on theoretical models of a point source light field and a range of oceanic conditions (e.g. diffuse attenuation coefficients) [48], [84]. In this study, a curved optical detector array design of hemispherical geometry with radius of 0.55 m is used to decouple UUV translation from orientation changes using sensor detection measurements of an external light source. Array sizes of 21 x 21 and 5 x 5 grids of detection sensors are investigated in order to observe comparative pose detection performance capabilities. Performance criteria of the pose detection algorithms include positional accuracy, processing speed, and dependence on the environmental characteristics [85].

5.2 Pose Detection Algorithms

5.2.1 Phase Correlation and log-polar transform

Phase correlation and log-polar transform approach to pose detection is able to take into account images in 4-DOF (i.e., rotation, scale and translation along two axes) [86]. The phase correlation algorithm uses Fourier Shift Theorem to detect the translated images [87]. It is given that two images, represented as f_1 and f_2 , observe the same target source acquired at different locations with relative translations, dx and dy , with respect to each other. Then, at the same relative orientation, the relationship between the two images can be described as:

$$f_2(x, y) = f_1(x - dx, y - dy) \quad (5.1)$$

The corresponding relationship of the Fourier transforms for these images, $F_1(\omega_x, \omega_y)$ and $F_2(\omega_x, \omega_y)$, is given by:

$$F_2(\omega_x, \omega_y) = e^{\omega_x dx + \omega_y dy} F_1(\omega_x, \omega_y) \quad (5.2)$$

The magnitudes of $F_1(\omega_x, \omega_y)$ and $F_2(\omega_x, \omega_y)$ are comparable to each other if the relative translations, dx and dy , are, in turn, comparatively small with respect to the image size, whereas the phase difference between the two images is directly related to their translation. This phase difference is equivalent to the phase of the cross-power spectrum:

$$e^{\omega_x dx + \omega_y dy} = \frac{F_1(\omega_x \omega_y) F_2^*(\omega_x \omega_y)}{|F_1(\omega_x \omega_y) F_2^*(\omega_x \omega_y)|} \quad (5.3)$$

where F_2^* denotes the complex conjugate of F_2 .

The relative translation values are derived by calculating the inverse Fourier Transform in (5.3). The location of the resulting peak corresponds to the translation of dx and dy , respectively, such that

$$(dx, dy) = \max(F\{e^{\omega_x dx + \omega_y dy}\}) \quad (5.4)$$

The rotation and scale between two images is calculated using the log-polar transform [88]. Here, both images are first translated from a Cartesian domain (x, y) , to a log-polar domain $(\log(\rho)\theta)$ using the following transformation:

$$\log(\rho) = \log(\sqrt{(x - x_c)^2 + (y - y_c)^2}) \quad (5.5)$$

$$\theta = \arctan\left(\frac{y - y_c}{x - x_c}\right) \quad (5.6)$$

where ρ is the radial distance from the center of the image, (x_c, y_c) and θ is the corresponding angle (Figure 5.1).

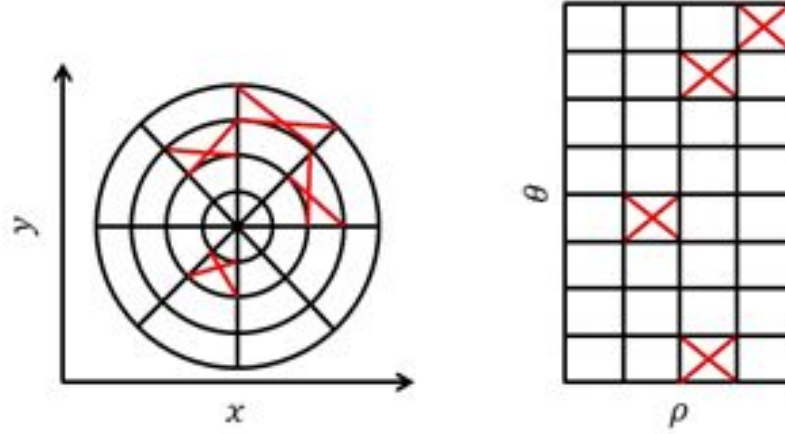


Figure 5.1: Transformation of an image from Cartesian space (left) to polar space (right).

After the transformation of the images to a log-polar domain, the phase correlation algorithm described in formula (5.3) is applied to detect relative rotation and scale between the two images.

AA reference image is calculated and obtained from the simulator and is designated as f_1 . The pose parameters for the reference image are a set of five pre-defined x -axis offsets (e.g., 4 m to 8 m with 1 m increments) with respect to the leader's beacon. All other 5-DOF pose geometries (translation with respect to the y and z axes; roll, pitch and yaw rotations) are kept the same as the leader UUV. The instantaneous image of the follower UUV in motion, f_2 , is calculated using the simulator for the pose evaluation path. The results from the phase correlation and log-polar transformation algorithms (i.e., relative translation and rotation between the reference and the instantaneous image) are converted to the local coordinate reference system showing the relative translations and rotations between the leader and that of the follower. The algorithms are evaluated in terms of their correlation to the parameters in the pose evaluation path datasets.

5.2.2 Spectral Angle Mapper (SAM)

Key parameters from the follower’s detector array output image were extracted to a vector of identifiers for each pose [84]. Changes in translation and orientation between the poses were monitored using a dot product between two identifier vectors of two poses using SAM described in Chapter 4. The SAM algorithm relies on five main image parameters that include the skewness of both the row and column of the resulting intensity profile of the image pixel with the maximum intensity and the row and column numbers of the image pixel with the maximum intensity as demonstrated in [89].

The SAM algorithm is implemented for a planar detector array of 21 x 21 elements. To quantify the amount of shift along the x -axis, an offline calibration procedure is performed for shifts ranging from 4 m to 8 m at 1 m increments. The reference image is the output obtained when there is offset along the x -axis, i.e. no translation in the y and z -axes or yaw or pitch rotations. (Roll rotation is not considered, as it is not possible to detect roll changes from a single light source configuration.) The image under test is the output for a specific relative geometry, including 5-DOF motion (6-DOF motion less roll rotation), between the light source and the detector. Images are produced for all possible poses of the follower UUV with respect to the leader UUV over a translation range $\pm 30^\circ$ at 3° increments. A vector of the five main image parameters is extracted for each image. This reference dataset, which is a look-up table of vector identifiers, is used to calculate the pose of the instantaneous images (Table 5.1). Instantaneous image vector identifiers are compared to vector identifiers in the aforementioned look-up table as shown in [89].

| INPUT | | | | OUTPUT | | | | |
|-------|------|-----------------|-------------------|--------|--------|------------------|---------|---------|
| y (m) | z(m) | yaw($^\circ$) | pitch($^\circ$) | Sk_x | Sk_y | SAM ($^\circ$) | Max row | Max col |
| 0 | 0.03 | 24 | 3 | -0.450 | -0.04 | 6.55 | 10 | 18 |
| 0 | 0.03 | 24 | 6 | -0.450 | 0.017 | 6.47 | 11 | 18 |
| 0 | 0.03 | 24 | 9 | -0.456 | 0.072 | 6.48 | 12 | 18 |
| 0 | 0.03 | 24 | 12 | -0.462 | 0.126 | 6.58 | 13 | 18 |

Table 5.1: A portion of the look-up table for pose detection.

Pose candidates based on the location of image pixel (row and column numbers) with the maximum intensity are extracted from the look-up table. The extracted pose candidates are allocated user defined weighting coefficients to form a cost function P_i such that

$$P_i = c_1|Sk_x - Sk_{xi}| + c_2|Sk_y - Sk_{yi}| + c_3|SAM - SAM_i| \quad (5.7)$$

where c_1 , c_2 and c_3 are the weighting coefficients, Sk_{xi} , is the skewness within the row, Sk_{yi} is the skewness within the column and SAM_i is the corresponding SAM angle for the instantaneous pose i . The resulting pose is determined based on the pose candidate that results in the minimum cost function P_i . The pose detection algorithm is evaluated based on the accuracy of the type of pose detection (i.e. relative translation and motion) between the leader and the follower vehicle and the amount of shift in translation and rotation. Pose detection algorithms using SAM approach are explained in more detail in [89].

5.2.3 Calculation of image moment invariants

The third approach used for pose detection in this study utilizes the image moment invariants that are defined as the weighted sum of the intensity values of the array pixels, $I_{i,j}$ with respect to the location of the peak intensity, $P_{max} = (y_o, z_o)$ [90], [91]. Image moment invariants can be defined as:

$$M_{pq} = \frac{1}{S} \sum_{i,j} (y_i - y_o)^p (z_j - z_o)^q I_{i,j} \quad (5.8)$$

where $S = \sum_{i,j} I_{i,j}$ and y_i, z_j are the row and column coordinates for a given detector in the array, respectively. p and q denote the order of moments. Image moment invariants are calculated up to the second order ($p = 2, q = 2$) for maintaining a simple and efficient calculation of the pose detection, i.e. $M_{00}, M_{10}, M_{11}, M_{22}$. The location of the pixel with the maximum intensity, P_{max} , is calculated at a sub-pixel accuracy. The relative translational and rotational motions between the UAVs in this approach are distinguished based

on moment invariant functions. The output of the image moment invariants algorithm for a specific pose is a 3 x 3 matrix where each element denotes information about the symmetry of the light intersected on the array (Figure 5.2). For example, the ratio of M_{23}/M_{33} gives information about y-axis translational shifts while the ratio of M_{32}/M_{33} relates to the z -axis translational shifts. The pose detection algorithm utilizes this property of the image moment invariants approach in a calibration procedure to determine and quantify the pose.

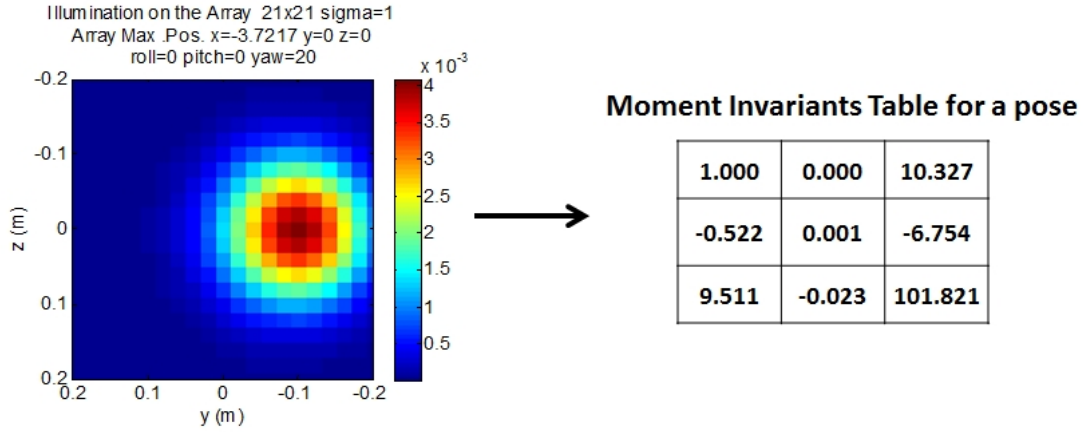


Figure 5.2: (Left) Image for a specific relative geometry between the light source and the detector. (Right) Image moments invariants output matrix.

5.3 UUV Modeling and Control

The UUV pose-based feedback control system is deemed as successful if the UUV in study is able to maintain relative pose to within an accuracy of ± 0.1 m in translation (i.e. in each x , y and z -axes) and $\pm 5^\circ$ in rotation (yaw and pitch). These specifications, without loss of generality, are determined based on requirements to adequately perform UUV docking operations with a docking station. The PID and SMC are implemented separately on a simulated UUV system under both the regulation (static-dynamic) and tracking (dynamic-dynamic) scenarios.

UUV control in this study is restricted to be decoupled. That is, the UUV is allowed to be controlled in 1-DOF at a time, (i.e. either a single x , y , or z translation or pitch or

yaw rotation). This is true for both the leader and the follower UUVs. The leader UUV is assumed to be controlled separately, say, with a user-controlled joystick (open-loop) whereas the follower UUV has PID and SMC implemented for autonomy.

For a dynamic-dynamic system under the assumption that the leader UUV has a known path *a priori*, the follower UUV can use information collected by the curved detector array as feedback to determine the leader UUVs relative pose such that

$$\boldsymbol{\eta}_f = \boldsymbol{\eta}_l - \boldsymbol{\eta}_d \quad (5.9)$$

where $\boldsymbol{\eta}_f$ is the follower pose, $\boldsymbol{\eta}_l$ is the leader pose determined by the follower, and $\boldsymbol{\eta}_d$ is the desired *relative pose*, incorporating desired relative distance and attitude, between the leader and the follower UUVs. The control problem in this case can be evaluated as a trajectory control problem as the leader is assumed to be remotely controlled to given waypoints while the follower generates its own time-varying trajectory from the leader motion. For a static-dynamic system, the problem can be considered as a setpoint regulation problem. regulation problem.

5.4 Positioning Control Results

The image moments approach requires a calibration procedure in order to distinguish the motion type and quantify the degree of relative translational and rotational displacements. In the case of a single guiding light beam, the calibration procedure is only conducted for positive translation and rotation values because the image moment invariants for positive translation and rotational motion are symmetrical. (A sign difference exists only for negative motion.) For a 21 x 21 sized light sensor detector array, image outputs from the array simulator include translation, ranging from 0 to 0.18 m in 0.02 m increments in the y and z -axis direction and from 0° to 27° with 3° increments for pitch and yaw rotations. For a 5 x 5 sized array, the calibration range for translation motion is from 0 to 0.14 m in 0.02 m

increments and from 0° to 27° with 3° increments for pitch and yaw rotations. In the x -axis direction, the calibration range between the leader and the follower vehicle is from 2 m to 8 m at 1 m increments. The limiting factor of the calibration range is the sub-pixel accuracy algorithm in both translational and rotational motion because this algorithm requires the intensity value of the neighbor pixel that is adjacent to the pixel with maximum intensity. Because of this limitation, the pixel with the maximum intensity cannot be located at a border of the array. The calibration procedure consists of two steps:

1. calibration for relative decoupled motion (i.e. the UUV being restricted to a single 1-DOF motion at a time)
2. calibration to detect motion when the UUV is translated in y -axis and rotated in yaw.

5.4.1 Static-Dynamic System

The pose detection algorithm is first based on distinguishing the type of motion (i.e. translational from rotational). This is accomplished by evaluating numerical values of the image functions which provide a descriptive feature of a specific motion type, i.e. translational or rotational motion. After the type of motion is determined, the amount of translational or rotational displacement is quantified through an off-line calibration procedure to linearly estimate the amount of relative shift in both translation (x , y and z -axis directions) and rotation (pitch and yaw) between the leader and the follower vehicles with respect to detected light levels.

In the static-dynamic system algorithm, it is assumed that the relative motion between the fixed light source and the UUV consists of 5-DOF motion (all 6-DOF except roll). In addition, pitch is not considered when the UUV aligns itself with the external light source when the UUV is initially misaligned along 3 axes of translation and yaw. The detection and control strategy for the static-dynamic system is first based on quantifying the UUV z -axis motion and control to its desired state, z_d . The second step is to distinguish between y -axis

translation and yaw motion. This second step is particularly complex as y -axis translation and yaw rotation both act on the same axis and can distort the detection algorithm and, therefore, degrade the accuracy of the results.

In this section, two sets of results are presented. The first set of results shows the detection and control capability of the pose detection algorithms combined with SMC and PID controllers when there is only one axis of translation or rotation that is initially misaligned. For each DOF, the UUV is directed to a desired state. The second set of results consists of case studies in which all pose detection capabilities and models are utilized. In this case, 4 axes of translation/rotation are misaligned (x , y , z and yaw) and the UUV has four desired states to reach. This is also conducted introducing a constant external current (disturbance). The control loop for all the simulations is run at a rate of 10 Hz. The detection and control sequence are shown in Appendix A.

Single-DOF SMC, Motion with 21 x 21 Detector Array

In this scenario, a UUV is mounted with a curved detector array consisting of 21 x 21 photodetector elements. A single stationary light source placed underwater acts as a guiding beacon to position the UUV with respect to a given reference value. 1-DOF SMC control is established for each of the five axes (i.e. x , y , z , pitch and yaw) separately. It is assumed that there are no external disturbances in the environment. The simulation results in Figure 5.3 show that with the pose detection algorithms and SMC, the UUV in study converges to the desired reference point for each DOF. In addition, Table 5.2 shows the results for decoupled translation and rotation, showing UUV initial conditions, reference (desired) position/orientation and final position/orientation.

Single DOF SMC, Motion with 5 x 5 Detector Array

It is shown in [84] that a 5 x 5 curved detector array is sufficient to distinguish between translational and rotational displacements. In addition, the construction of a 5 x 5 array is

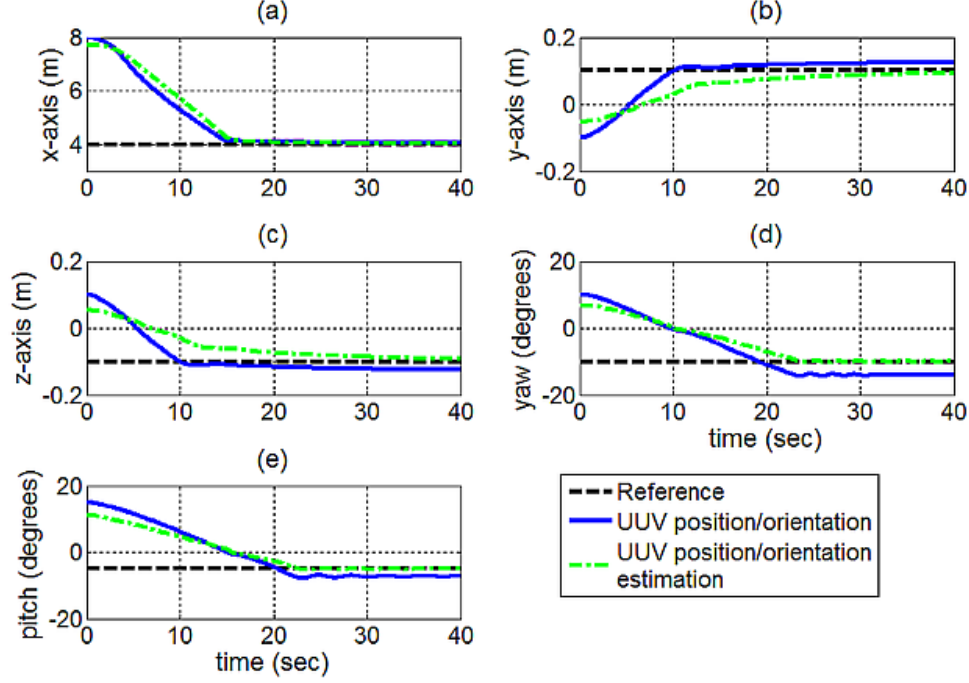


Figure 5.3: Independent DOF SMC results for a curved 21 x 21 array. (a) x -axis control (b) y -axis control (c) z -axis control (d) yaw control (e) pitch control.

more cost-efficient than the construction of a 21 x 21 array. Therefore, it is decided that pose detection and control algorithms are to be developed for a 5 x 5 array. SMC is implemented in the same way as applied in the case of the 21 x 21 array. The simulations are conducted without any external disturbance present. It is seen that the pose detection algorithm and SMC work efficiently to dynamically position the UUV to the vicinity of the desired reference values as shown in Figure 5.4 and Table 5.3, especially in the translational directions. In both cases, i.e. a 21 x 21 and a 5 x 5 detector arrays, it is observed that small amplitude oscillations exist for yaw and pitch control. As it is shown that pose detection and SMC for a 5 x 5 array demonstrate satisfactory control performance and that a more costly option of a 21 x 21 array is not necessary, further simulations in this study are conducted solely with a 5 x 5 detector array.

| Initial position/ orientation | Reference position/ orientation | Final position/ orientation |
|----------------------------------|------------------------------------|--------------------------------|
| $x_i = 8$ m | $x_d = 4$ m | $x_f = 4.02$ m |
| $y_i = -0.1$ m | $y_d = 0.1$ m | $y_f = 0.09$ m |
| $z_i = 0.1$ m | $z_d = -0.1$ m | $z_f = -0.09$ m |
| $\psi_i = 10^\circ$ | $\psi_d = -10^\circ$ | $\psi_f = -10.05^\circ$ |
| $\theta_i = 10^\circ$ | $\theta_d = -5^\circ$ | $\theta_f = -5.03^\circ$ |

Table 5.2: Initial, reference and final UUV positions and orientations for a 21 x 21 curved array for decoupled 5-DOF Control.

| Initial position/ orientation | Reference position/ orientation | Final position/ orientation |
|----------------------------------|------------------------------------|--------------------------------|
| $x_i = 8$ m | $x_d = 5$ m | $x_f = 4.99$ m |
| $y_i = -0.1$ m | $y_d = 0.1$ m | $y_f = 0.09$ m |
| $z_i = -0.14$ m | $z_d = 0.14$ m | $z_f = 0.14$ m |
| $\psi_i = 20^\circ$ | $\psi_d = -20^\circ$ | $\psi_f = -17.7^\circ$ |
| $\theta_i = -20^\circ$ | $\theta_d = 20^\circ$ | $\theta_f = 15.3^\circ$ |

Table 5.3: Initial, reference and final UUV positions and orientations for a 5 x 5 curved array for decoupled 5-DOF Control.

x-axis PID control with a 5 x 5 Detector Array

In addition to the SMC to dynamically position a UUV to a desired distance and orientation, the effectiveness of a PID controller is also investigated. The PID controller is tested for the control of translation only in the x -axis direction and without any disturbances present. The selected PID controller gains are $P=400$, $I=2$ and $D=300$. The PID controller does, in fact, eventually control the UUV to the desired reference value (Figure 5.5). However, after a reasonable effort to tune control gains, excessive overshoot (maximum of 30%) still persists. PID controller performance is acceptable for translational control about the x -axis, but a potential overshoot is not acceptable for y and z -axis translational control because it causes the UUV to lose its line-of-sight with the external light source. Therefore, it is concluded that PID control is considered unsuitable for this application.

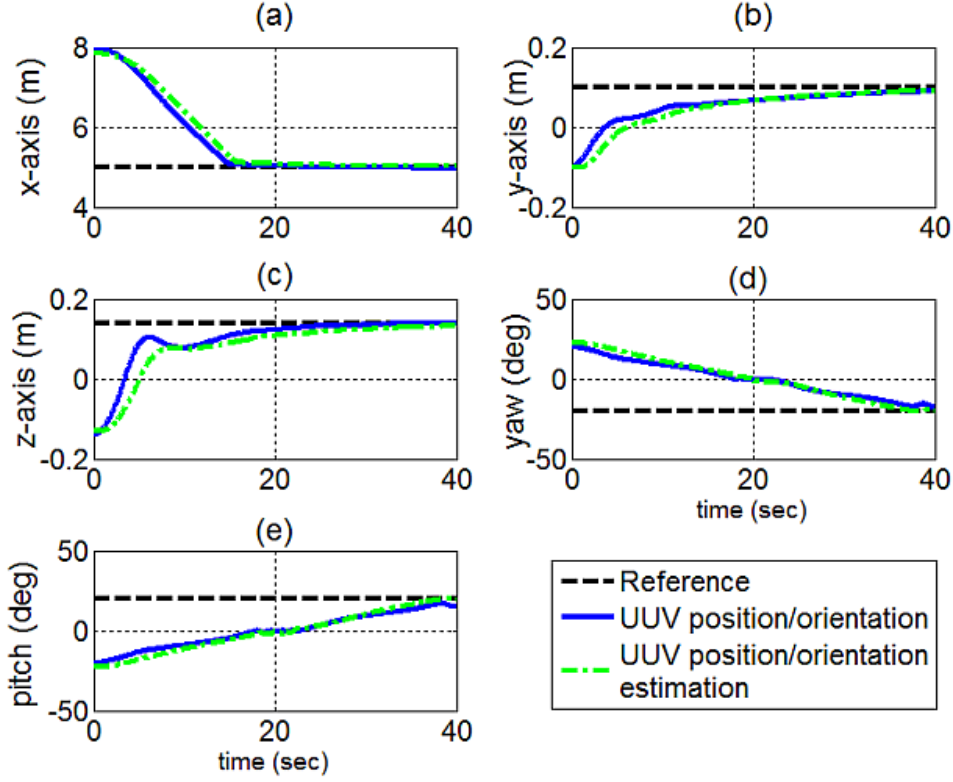


Figure 5.4: Independent DOF control results with SMC for a curved 5 x 5 array. (a) x -axis control (b) y -axis control (c) z -axis control (d) yaw control (e) pitch control.

Case study: Dynamic Positioning with Multiple Concurrent Initial Pose Errors

After it is determined that a 5 x 5 array with the implementation of SMC is suitable for pose detection and control of a UUV, a dynamic positioning case study is conducted. In contrary to the cases described in the previous sections, the UUV is now given 4-DOF off-axis initial conditions (i.e., concurrent non-zero errors in x , y , z and yaw). The goal is to dynamically position the UUV with respect to the fixed, single beam light source with a desired position and orientation. The control strategy in this case study is for the UUV to perform decoupled control actions, one DOF at a time, until the desired reference value is finally reached. The decoupled control sequence is as follows:

1. z -axis control
2. yaw control

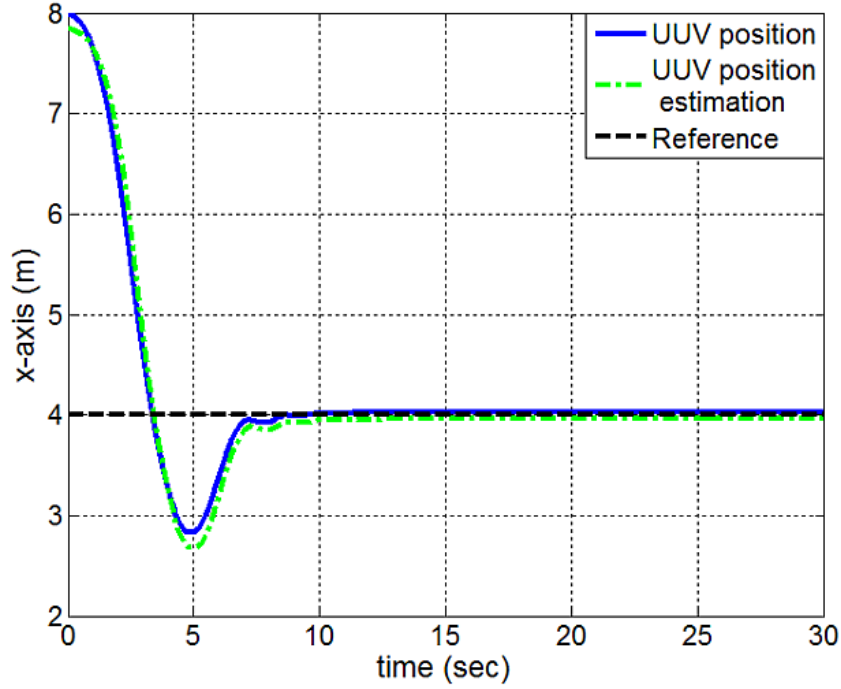


Figure 5.5: PID x -axis control for a 5 x 5 array.

3. y -axis control

4. x -axis control

The initial, reference and final positions and orientations are listed in Table 5.4.

| Initial position/ orientation | Reference position/ orientation | Final position/ orientation |
|----------------------------------|------------------------------------|--------------------------------|
| $x_i = 8$ m | $x_d = 4$ m | $x_f = 4.12$ m |
| $y_i = 0.14$ m | $y_d = 0$ m | $y_f = -0.01$ m |
| $z_i = 0.14$ m | $z_d = 0$ m | $z_f = 0.02$ m |
| $\psi_i = -20^\circ$ | $\psi_d = 0^\circ$ | $\psi_f = -0.1^\circ$ |

Table 5.4: Initial, reference and final UUV positions and orientations for a 5 x 5 curved array for decoupled 4-DOF control.

The results demonstrate that the UUV accomplishes the control task to within reasonable accuracy (Figure 5.6). The calibration procedure for y and yaw detection is based on the case where the UUV z -axis coordinate is perfectly aligned with the corresponding z -axis coordinate of the external light source. Thus, the pose detection algorithm is robust

enough to produce accurate estimates in the presence of relatively small steady-state errors. In the second step, yaw control is quite accurate with 0.1° error and then the control system switches to y -axis control mode, where it stops at $t=80$ s when a satisfactory y -axis position is reached. In the final step, the x -axis coordinate is controlled with a steady-state error of 0.12 m. It should be noted that after y -axis control stops and x -axis control begins, there is a slight change in the UUV y -axis coordinate. This is due to the steady-state error in yaw.

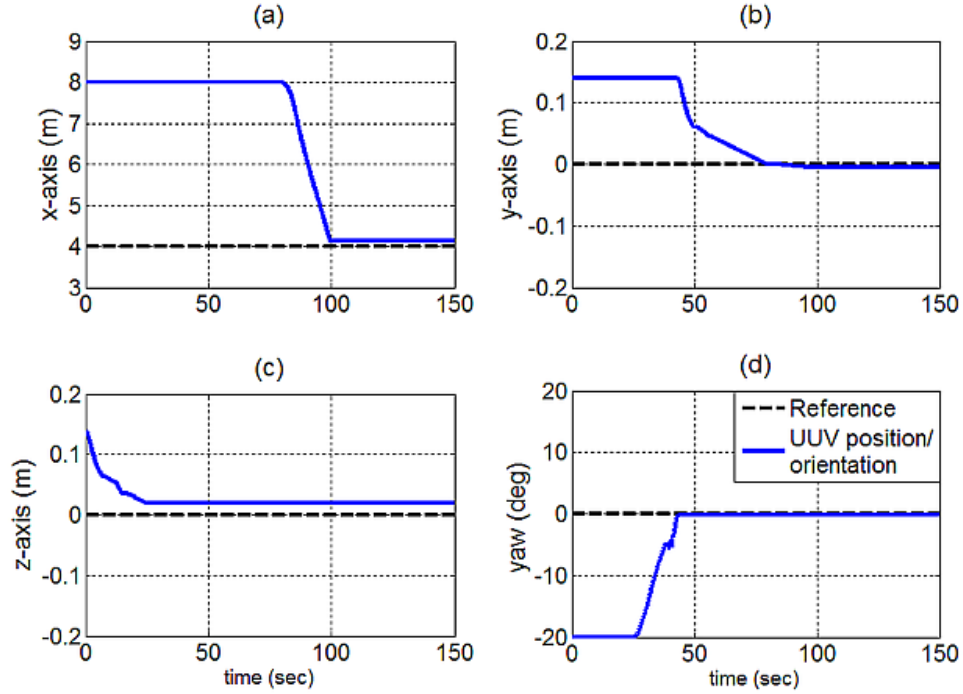


Figure 5.6: UUV docking case study using SMC for a 5×5 array. The UUV with four initial non-zero pose errors is commanded to position itself with respect to a fixed light source. (a) x -axis control (b) y -axis control (c) yaw control (d) z -axis control.

Case study: Dynamic Positioning with Multiple Concurrent Initial Pose Errors in the Presence of Added Disturbances

In this scenario, the UUV initial conditions and the references are kept the same as that in Table 5.4, but a constant current (external disturbance) of -0.03 m/s in the x -axis direction is introduced. It is observed from the results as shown in Figure 5.7 that z -axis control is not significantly affected by the added current but does have a noted steady-state

error. And, although yaw control is affected by the current, it stabilizes at 8° . Due to the yaw steady-state offset, when the UUV moves along its body-fixed coordinate x -axis, the UUV also moves in the Earth-fixed coordinate y -axis. This can be observed from $t = 7$ s. to $t = 82$ s. In this period, there is only x -axis control. Then, the controller switches to y -axis control and it attempts to regulate to the y -coordinate but does so with some chatter. As the UUV approaches to x -axis desired reference, the SMC switches between x and y -axis control to the end of the simulation.

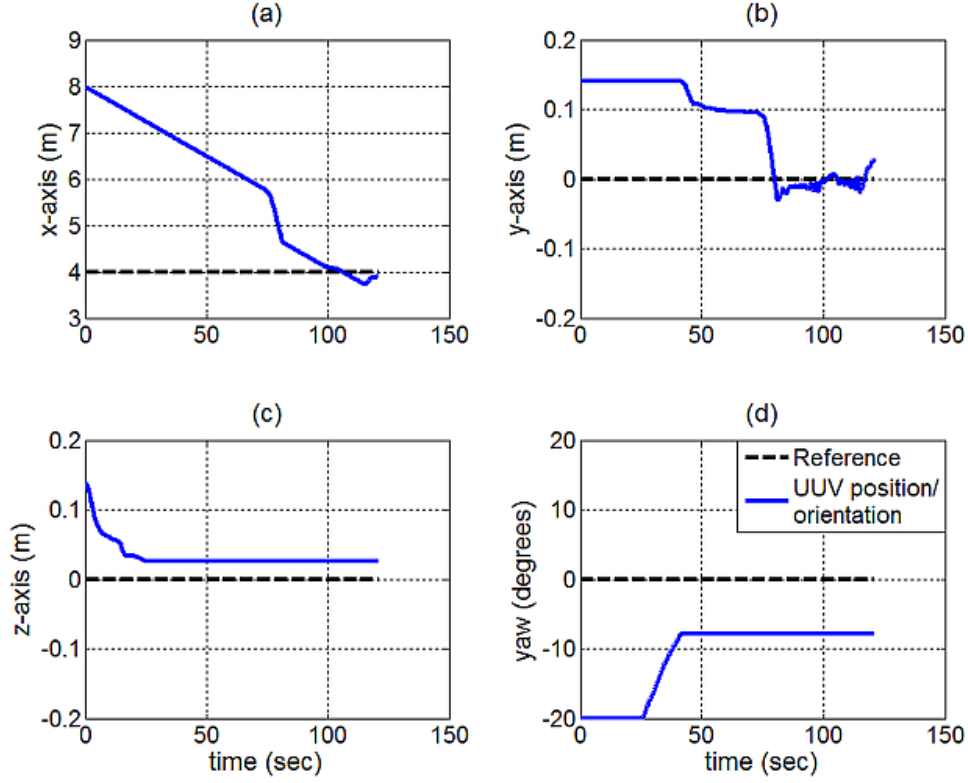


Figure 5.7: UUV docking case study using SMC for a 5×5 array with a current of -0.03 m/s in x -axis. (a) x -axis control (b) y -axis control (c) yaw control (d) z -axis control.

5.4.2 Dynamic-Dynamic System

In addition to the static-dynamic scenario in which the optical-based sensor system uses SMC to control a UUV with respect to a fixed light source, the capabilities of the dynamic-dynamic (tracking control) scenario are also investigated. In the dynamic-dynamic system,

there are two moving UUVs: a leader UUV and a follower UUV. The leader UUV has a light source at its crest and is assumed to move independently, for example, via remote operation. The follower UUV processes the sampled light field from the leader UUV on the detector array and performs the appropriate control action autonomously in order to track the leader. In this scenario the leader and the follower UUV initial conditions, reference values and the final positions are given in Table 5.5.

| Initial Leader position | Reference position | Final Leader position | Final Follower position |
|-------------------------|--------------------|-----------------------|-------------------------|
| $x_{il} = -8$ m | $x_d = -8$ m | $x_{fl} = -9.75$ m | $x_{ff} = -1.5$ m |
| $y_{il} = 0$ m | $y_d = 0$ m | $y_{fl} = 0.1$ m | $y_{ff} = 0.14$ m |
| $z_{il} = 0$ m | $z_d = 0$ m | $z_{fl} = 0.11$ m | $z_{ff} = 0.14$ m |

Table 5.5: Initial, reference and final UUV positions and orientations for a 5 x 5 curved array for dynamic-dynamic control.

Initial evaluation of yaw control in a dynamic-dynamic scenario (not shown here) reveals that relatively small deviations in yaw cause loss of line-of-sight between the UUVs. For this research, yaw control in a dynamic-dynamic system is not within the scope of this study. The controlled DOF between the UUVs are, instead, translation about all three coordinate axes. SMC is implemented for the control of a UUV mounted with a 5 x 5 detector array. In this simulated scenario, both the leader and follower UUV start with an 8 m offset in the x -axis direction and no offset along the y and z -axis directions. The control goal for the follower UUV is to maintain these initial conditions when the leader UUV translates along $x - y - z$ axes. The results shown in Figure 5.8 demonstrate that at the end of the scenario, the x -axis offset between the leader and the follower UUVs is maintained at a steady-state distance of 8.25 m, the y -axis offset at 0.04 m and the z -axis offset 0.03 m. The x -axis leader pose estimation during the time of flight is within reasonable accuracy and as a result, a smoother follower UUV trajectory is achieved. For z -axis control, initially, the leader UUV's z -axis coordinate is estimated to decrease while it actually increases. The pose detection algorithm then corrects its estimations and a more accurate control action is performed. A similar situation is observed in y -axis control where it is seen that the leader UUV is initially

estimated to move in the reverse direction of its actual trajectory. Then, the detection algorithm corrects its estimations and more accurate control feedback and trajectory control are achieved.

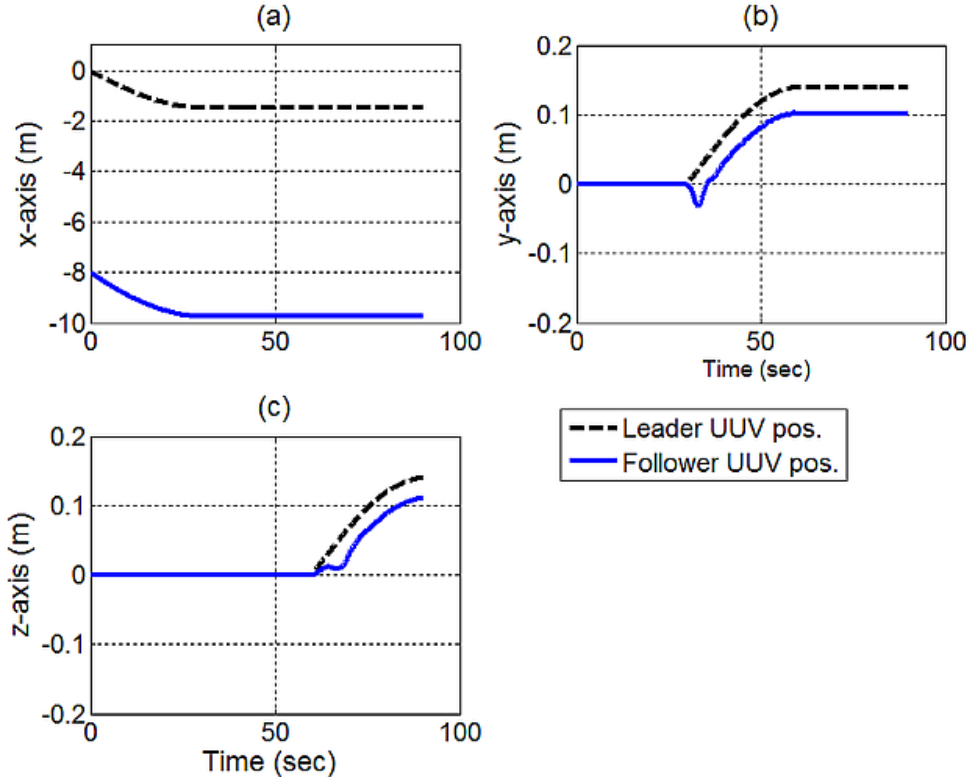


Figure 5.8: The leader-follower case study in a dynamic-dynamic system with SMC for a 5 x 5 array. (a) x -axis control (b) y -axis control and (c) z -axis control.

5.5 Discussion of Analytical Pose Detection and Positioning Control

Simulation results of pose detection algorithms and SMC demonstrate that dynamic positioning of UUVs can be established with acceptable accuracy. The performance of the pose detection algorithms evaluated in this chapter (phase correlation and log polar transform, SAM, and image moment invariants) are compared based on their ability to provide fast, reliable and accurate pose estimates. The phase correlation and log-polar transform algorithm yield accurate results for cases when the motion is only translation. For rotational motion detection, it is not suitable as symmetric detected images of the external light source prevent

accurate pose estimations. It should be stressed that roll angle is not detectable as there is a single axisymmetric light source with a Gaussian intensity profile. The results of SAM algorithm and its application on the control of a leader-follower UUV application for a planar array are shown in [89]. SAM algorithm can yield successful results. However, the calibration procedure to provide pose outputs is extensive and a lengthy look-up table is needed to generate a pose output. Therefore, it may not respond to the system requirement of a fast processing algorithm. Image moment invariants approach is chosen due to the following reasons: Simple linear models exist for pose estimation, which leads to faster computational speeds and makes it suitable for real-time applications. In addition, less calibration time is required as its dependence on the look-up tables decreases. This results in less required computational effort in the implementation of the system. Furthermore, an accurate estimate of poses can be obtained with multiple concurrent non-zero pose errors. More specifically, x -axis pose estimation can be obtained when the UUV undergoes y and z -axis translations and yaw rotations. Alternatively, a procedure can be developed to distinguish and quantify concurrent y -axis translations and yaw motions.

SMC and PID controllers are evaluated in conjunction with the feedback obtained from the image moment invariants algorithm. The PID controller results in system overshoot. While overshoot can be tolerated in x -axis control, overshoot in the y and z -axis directions or in yaw is not desirable as it results in the UUV losing line of sight with the external light source. The SMC is selected as a first-order controller with a time-varying boundary layer and a saturation function (to minimize chatter). The controller is a SISO controller where the kinematic and dynamic cross-coupling terms are neglected in the UUV model. The uncertainties due to added mass and hydrodynamic forces are compensated in the control system. SMC requires position and velocity state information as sensor feedback. The position information can be obtained from pose detection algorithms. However, for the velocity signals, the derivative of the pose information is taken. In order to avoid data fluctuations, the Kalman filter is implemented for both position and velocity signals. SMC

simulation results suggest that satisfactory positioning results can be obtained. Overshoot which is an important criterion in this study is not observed in SMC simulation results. The study of the effect of external disturbances such as current suggest that the control system can yield acceptable results (especially in x and y -axis directions) under a modest amount of constant current in x -axis (-0.03 m/s). However, the steady-state error in yaw increases and requires compensation for reasonable accuracy.

The effect of the detector array size on the dynamic positioning is investigated by developing pose detection algorithms for a 21 x 21 and 5 x 5 detector arrays. The simulation results conducted on a 5 x 5 array suggest that the developed algorithms yield satisfactory control results, so as to deem the use of a more costly 21 x 21 array unnecessary. The SMC controller is shown to be robust against modeling uncertainties and to modest amount of disturbances. However, when there are larger disturbance forces (especially in the $y - z$ plane and/or when there is non-systematic background noise such as a sediment plume), the estimated pose may be misinterpreted and the UUV could lose line of sight with the external light source.

CHAPTER 6

EXPERIMENTAL POSE DETECTION AND POSITIONING CONTROL

The capabilities of an optical detector array to determine the pose (x , y and z -axes) of a UUV based on optical feedback to be used in UUV docking applications are demonstrated in this chapter. The optical detector array consists of a 5×5 photodiode array that samples the intersected light field emitted from a single light source and forms an image. After a set of calibrations for pose geometry, it is possible to develop pose detection algorithms based on an image processing approach, specifically image moments invariants. Monte Carlo analysis is performed to determine the system performance under environmental and hardware uncertainties such as diffuse attenuation coefficient, temperature variations and electronic noise. A previously developed simulator [84] is used as a test bed to run the Monte Carlo simulations. The simulator takes the relative geometry between the light source and the detector and environmental and hardware characteristics as inputs. The performance evaluation for Monte Carlo simulations is based on the generated pose outputs with respect to changing environmental and hardware parameters for a number of samples, i.e. $N_S=2000$. Monte Carlo analysis results verify that the pose uncertainties associated with x , y and z -axis are 0.88 m, 0.67 m and 0.56 m, respectively, with 95% confidence interval bounds. Experimental results of this study show that the pose estimates along the x , y and z -axes are accurate to within 0.5 m, 0.2 m and 0.2 m, respectively [92].

6.1 Docking Station Maneuvers

Unmanned Underwater Vehicles (UUVs) provide an operational platform for long periods of deployment on the order of hours and in depths that are too dangerous for divers. However, the time of operation of these systems is limited based on the hardware available in the platform, such as the power supply and data storage capacity. In order to extend the duration of the mission, the power supply needs to be replaced or recharged and data should be transferred from the UUVs internal storage unit to an external storage unit in order to clear space for additional data collection. A common approach to extend the UUV operations underwater is the use of docking stations which enable the UUVs to conduct data transfer and recharge the batteries [8].

The two most common types of docking station architectures are: (1) funnel-docking station in which the UUV enter a tube for homing [93]; and (2) pole-docking station, where the UUV connects to the station using a hook mechanism placed perpendicular to the seafloor [94]. The structural design of the funnel docking station is similar to a cone (Figure 6.1a). The funnel docking station is designed for a specific class of UUVs of the same length with the same physical connections for power [19]. The funnel docking station allows a small tolerance of misalignment as the UUV navigates into the cone. Due to the cone shaped design, the UUVs entrance trajectory into the docking station is restricted. The data transfer in the funnel type system can be conducted through wired communication or wireless Ethernet radios [9]. The power transfer is accomplished by having a charge pin inserted from the docking mechanism. The data and power transfer in these systems are reliable as there is a stable connection between two platforms when the vehicle goes into the funnel type docking station. However, the design of each funnel-docking station is unique for a specific class of UUVs. The architecture of the pole-docking station offers an omnidirectional docking approach (Figure 6.1b). The UUV latches onto a vertical docking pole in order to dock. After the UUV is securely latched, a circular carriage that moves along the pole forces the

UUV to mate with the inductive links for data and power transfer [95]. The pole docking station does not restrict the UUVs entrance trajectory into the docking station. However, the tolerance of UUV speed and its distance from the pole is limited. If the UUV is not rigidly attached to the pole, power and data connections between the UUV and the docking station may not be successful [9].

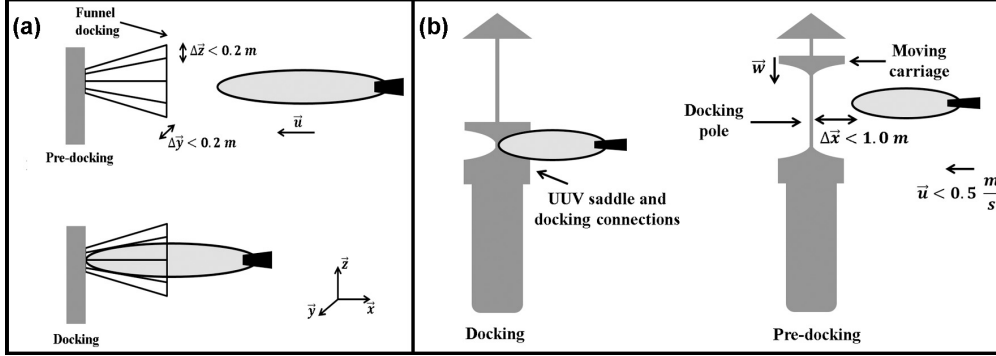


Figure 6.1: (a) Funnel type docking station and (b) Pole type docking station architectures.

Recent studies have demonstrated the potential use of both acoustic and optical communication for docking [61], [62],citer65. In these systems, acoustic communication is used in relatively longer ranges, about 10 m, for navigating towards a docking station and video cameras are used in closer ranges, within 8-10 m, to guide the vehicle into the docking station.

This chapter presents pose detection to be used in a UUV control system using only the feedback from an optical detector array. This approach can be utilized in UUV navigation e.g. into a docking station. The detection system developed is based on a static-dynamic system, i.e. where only one UUV is navigating to a fixed docking station that is fixed in space. A single beacon light source at the docking station was used as a transmitting unit, and a prototype detector array interface mounted on a dynamic UUV platform is used as a detector unit. The input data generated from the detector array are signature images of the light field that are used to calculate the relative pose between the UUV and the docking station and provide feedback to guide the UUV to the docking station. The pose detection performance during the navigation of the UUV platform is evaluated for both the funnel-

docking and pole-docking stations. Without loss of generality, the control system is designed for the environmental characteristics of Portsmouth Harbor, NH. As a proof-of-concept, a scaled model is experimentally tested at the wave and tow tank at Jere A. Chase Ocean Engineering facilities.

The performance of the experimental platform, i.e. optical detector array, developed in this study is evaluated in terms of two criteria. The first criterion is accuracy of pose detections along all three translational axes, x , y and z . This criterion reflects the potential of successful funnel type docking operation of a UUV in which the entrance trajectory is restricted. The second criterion is the accuracy of UUV velocity estimates which is important when evaluating when UUV performance of pole type docking operation during approach in which the UUV speed tolerance (as opposed to entrance trajectory) is limited.

6.2 Detection Array Hardware

The pose detection algorithms were developed based on the image moment invariants approach which is described in Section 5.2.3. The hardware selection for this study is based on the results obtained from prior research that included evaluation of different detector array geometries based on their capability to generate a unique pose feedback to the UUV as shown in Chapter 5.

The detector module used in this research consists of a 5×5 photodiode array of Thorlabs SM05PD1A photodiodes, two Analog to Digital (A/D) boards, an on-board computer (OBC), power supply and reverse-bias circuit elements. The photodiodes placed on a hemispherical surface with an outer diameter of 0.25 m. The hemispherical surface with 25 holes of 0.0254 m diameter is manufactured using a Rapid Prototyping Machine (Dimension SST 768) using ABS material. Each detector is placed in waterproof acrylic fixtures that are mounted into the holes on the frame (photodetector facing outward) and aligned concentric to the hemisphere center. The length of each acrylic fixture outside the hemisphere is 0.064 m. Thus, the effective radius of the detector array (radius of the hemisphere plus the length

of the fixture) is 0.19 m.

The photodiodes were connected to a reverse-bias circuit that provide dynamic output range of 0 to 5 V. SubMiniature version A (SMA) cables are used to connect the photodiode output to the reverse bias circuit. The light intensities collected by the photodiodes are sampled using two A/D boards on two different Arduino microcontroller platforms with 10-bit resolution (0-1023 bit range). The data sampled at the A/D boards are transmitted serially to the OBC running a 1 GHz ARM Cortex processor with a Linux operating system. The OBC receives the collected light intensity data from the photodiodes and sends it to a Linux-based PC. The photodiode intensity readings are sampled at 5 Hz. The power supply used in the reverse-bias circuit is provided by 5 V port on the Arduino platform. The reverse-bias circuit to increase the dynamic range of a single photodiode consists of a $47\ \Omega$ resistor, a $1\ M\Omega$ resistor and a $0.47\ \mu F$ capacitor. detector array module concept and the reverse-bias circuit used can be seen in Figure 6.2 and Figure 6.3, respectively. The final experimental platform can be seen in Figure 6.4.

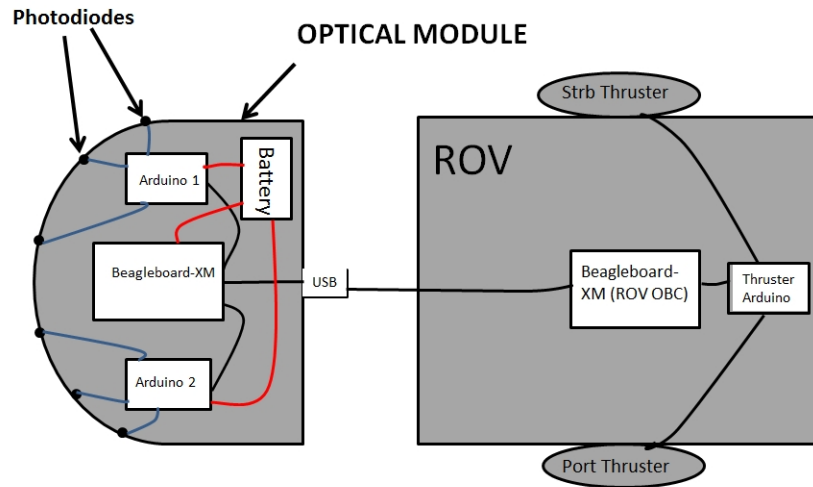


Figure 6.2: (Left) Optical Module Concept with data acquisition components. (Right) ROV platform.

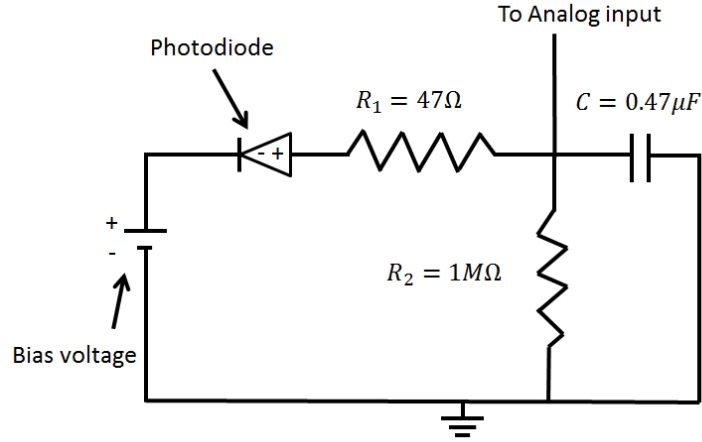


Figure 6.3: Reverse-bias circuit used in the experiments.

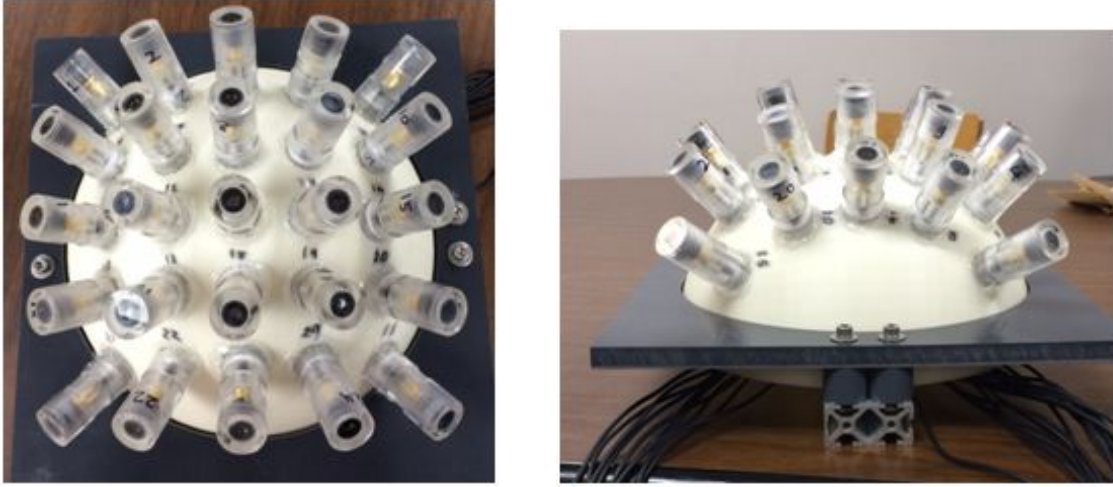


Figure 6.4: The optical detector array used in the experiments. (Left) Top view. (Right) Side view.

6.3 Methodology

The empirical measurements in the study are conducted in the wave and tow tank at the UNHs Jere A. Chase Ocean Engineering facilities. The measurements are based on a scaled model designed for use in Portsmouth Harbor between New Hampshire and Maine. A prospective location for a docking station is considered at the entrance to the harbor near UNHs Judd Gregg Marine Research Complex facilities in Fort Point, Newcastle, NH. Portsmouth Harbor is a highly active port that includes a naval shipyard, fishing vessels, sur-

vey vessels and recreational vessels. As a result, the harbor is acoustically noisy and optical communication is the most viable method to navigate a UUV to a docking station. There are several factors that affect the reliability of the system performance such as the diffuse attenuation coefficient, bathymetry and current amplitude information in the prospective implementation area. According to UNH Coastal Ocean Observation Center archive on August 16, 2005, the average diffuse attenuation coefficient value in Portsmouth Harbor area was 0.2 m^{-1} [96]. The depths in the harbor range up to 20 m in depth at the center of the navigational channel with a current speed range of 0.1-0.9 m/s at around 12 m depth at Fort Point [97], [98].

The depth of the wave and tow tank is 2.44 m with relatively clear water conditions (diffuse attenuation coefficient of 0.09 m^{-1}). The tank is outfitted with a cable-driven tow carriage with actuation that extends through the length of the tank that can move up to 2.0 m/s. A single light source (400 W metal halide light with ballast) is evaluated as a potential guiding beacon for the docking station. This mock-up docking station is placed onto the wall of the wave and tow tank (Figure 6.5 and Figure 6.6). The detector array is mounted on an aluminum frame on the wave and tow tank. For pose calibration, the distance between the light source and the detector array is measured and the x -axis offset is controlled with the actuating mechanism.

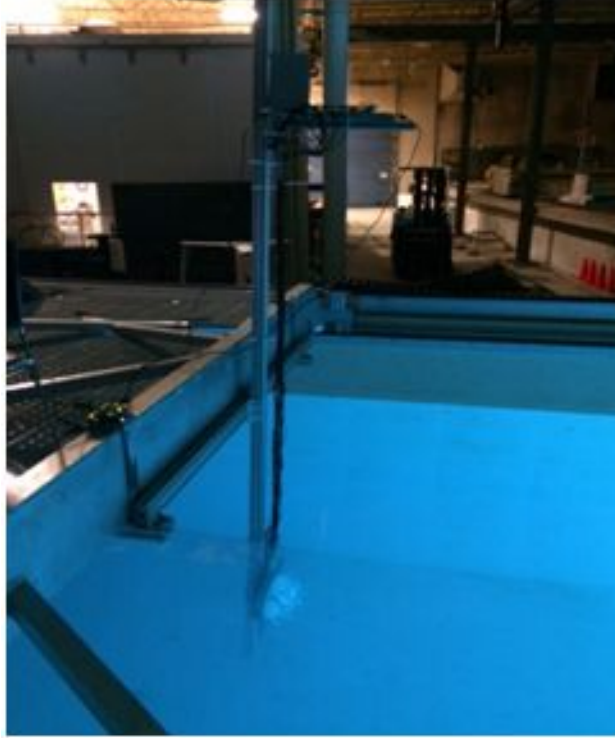


Figure 6.5: Detector array mounted on the dynamic platform on the wave and tow tank.

6.3.1 Photodiode and Pose Estimation Calibration Procedure

Two types of calibration procedures are conducted for this study:

1. Calibration for photodiodes
2. Calibration for pose estimation in water in wave and tow tank.

Photodiode calibration considers various factors: Output consistency of the photodiodes to be used in the optical detector array when they are exposed to the same light field conditions, photodiode responses to the potential temperature variations and potential electrical noise levels and cross-talk within the system. Pose estimation calibration is also used in the development of pose detection and control algorithms.



Figure 6.6: 400 W light beacon mock-up docking station mounted on the wall of the wave and tow tank.

Photodiode Calibration

In photodiode calibration procedure, in order to check the consistency of the photodiode outputs, a single photodiode, i.e. photodiode under test, is mounted to a threaded cage plate (Thorlabs SM05). The photodiode and cage plate setup are stabilized at a distance of 0.18 m away from a halogen light source (PL-900 Fiber-Lite). The output from the photodiode under test is connected to a Tektronix DPO 3054 oscilloscope. The data is collected for 2 minutes and the average voltage was recorded. 25 photodiodes were tested at a time in order to observe their output voltage range under same conditions (Figure 6.7).

A separate calibration procedure is conducted to quantify SM05PD1A photodiode response to the potential temperature changes in water, where each photodiode is placed in an acrylic waterproof housing and submerged into a digitally controlled refrigerated bath/-circulator (NESLAB RTE-111). In this procedure, the water bath is used to change the

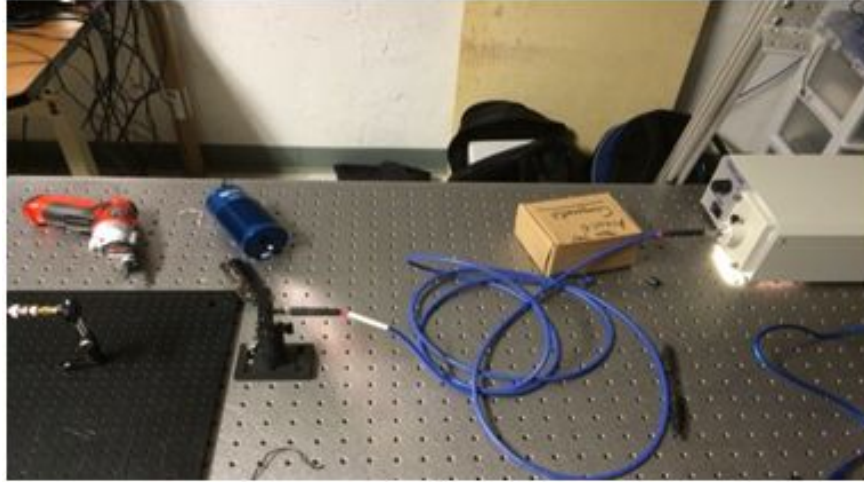


Figure 6.7: Photodiode Calibration.

surrounding water temperature from 20°C to 70°C at 10°C increments. (20°C is approximately the operating temperature at the wave and tow tank). Here, a green laser at 532 nm wavelength (Z-Bolt SCUBA underwater dive laser) with the power output of 4 mW illuminates the photodiode. A k-type thermocouple is used to measure the temperature of the photodiode and fixture. At each temperature, the system is brought to thermal steady state before the voltage output of the photodiode is measured. The SM05PD1A output is connected to an oscilloscope (National Instrument PXI 5142) and the responses for varying temperatures are recorded (Figure 6.8 and Figure 6.9).

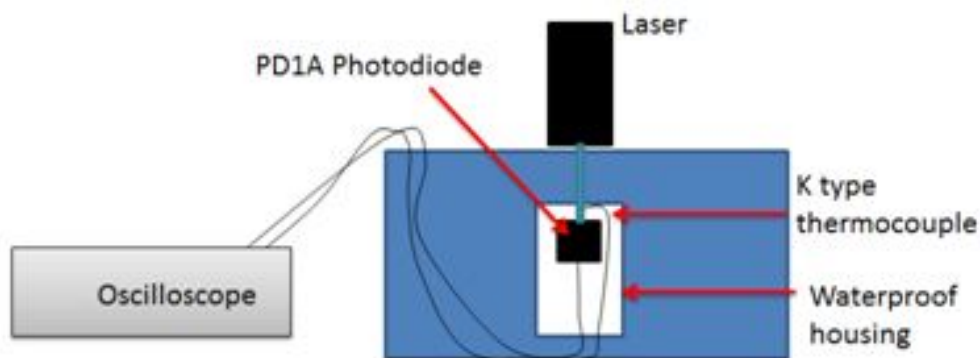


Figure 6.8: Diagram for temperature calibration.

Photodiode response is also observed for any potential noise and electronic cross-talk in the data acquisition system. In order to test these effects, all of the photodiodes are mounted



Figure 6.9: Experimental setup for photodiode response to the temperature changes.

on the curved detector array. In a dark environment, one photodiode is illuminated at a time with a light source using a black plastic tube between the light source and the detector. The remaining 24 photodiodes are exposed to the ambient light. The response of each of the 25 photodiodes is observed for any potential cross-talk that can occur during the transmission of the signals with 3.3 m SMA cables. Potential noise sources in the hardware are explained in more detail in Chapter 4.

Pose Calibration

Pose calibration procedure is conducted to detect and quantify the pose to be used as feedback signal in the control system. The DOF of interest for UUV motion for calibration stage are translations along x , y and z -axes. Calibration is conducted using the optical detector array in the tow carriage in the wave and tow tank. The center of the light source is submerged 1 m deep into the water column. The calibration procedure for translation along the x -axis is conducted using the wave and tow tank computer-controlled actuation mechanism. Along this axis, the optical detector array distance from the light source is

varied from 4.5 m to 8.5 m at 1 m increments. For the y and z -axes, aluminum 80/20 frames are used to precisely quantify the amount of translational array offset. The calibration procedure for y -axis is for a range of -0.6 m to 0.6 m at 0.3 m increments. For z -axis, the calibration procedure was conducted starting at 1 m (referred to as 0 m in the plots) deep in the water column to 1.8 m (referred to as 0.8 m in the plots) depth at 0.2 m increments. Thus, at each x -axis position, 25 different images (beam patterns) are collected (125 images in total calibration scheme). The photodiode intensity data collected during the calibration procedure are analyzed offline in order to develop algorithms that convert the light input into pose information.

6.3.2 Stochastic Assessment of Pose Uncertainty

An accuracy assessment of the pose detection algorithms is developed using Monte Carlo analysis. The accuracy assessment is used to predict the uncertainty in the final pose based on optical feedback. All the first-order and second-order parameters contributing to the pose estimation are identified. These parameters include from environmental characteristics (such as diffuse attenuation coefficient and temperature variation in the water column) and the detector array and processor hardware noise as in Chapter 3. By using a random distribution for a larger number of samples (e.g. $N_S=2000$) for these parameters, the total propagation uncertainty (TPU) can be obtained.

The parameters that contribute to the forming of the beam pattern on the optical detector array mainly depend on the environmental conditions. More specifically, the diffuse attenuation coefficient, (a measure of turbidity in the water) and the temperature variation in the medium are the key contributors to environmental conditions. The scattering of light in the water column is not taken into account in this study. The uncertainties relating to diffuse attenuation coefficient and the water temperature variations are modeled as uncorrelated Gaussian random variables. The uncertainty associated with the hardware characteristics is modeled as unipolar random values drawn from standard uniform distribution. These

variables are taken into account into the developed numerical simulator which generates an image on the specified number of photodiodes based on:

1. The geometry between the light source and the detector
2. The environmental characteristics of the medium (e.g. turbidity and the temperature)
3. Hardware characteristics (e.g. electronic noise and light source intensity profile and distribution), etc

Pre-determined model uncertainty parameters were integrated into the hardware and environment model to estimate the total uncertainty propagation in the pose detection algorithms. The simulation scheme for Monte Carlo analysis is shown in Figure 6.12.

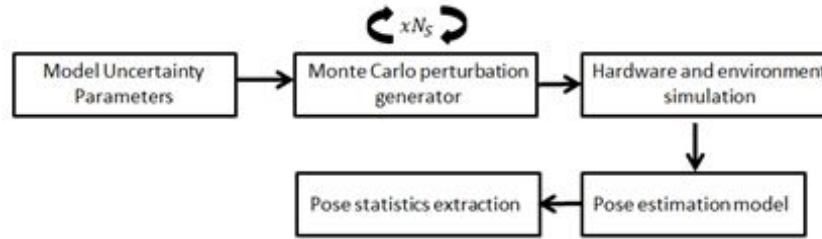


Figure 6.10: Monte Carlo flow diagram for the pose statistics.

The standard deviation of the hardware noise is determined during the calibration process and it was deduced that the standard deviation of the noise did not exceed 1% of the maximum photodiode intensity. Uncertainty parameters used in Monte Carlo analysis are given in Table 6.1

| Parameter | Standard deviation |
|---------------------------------|---------------------|
| Output values consistency | 2.4 mV |
| Temperature variation | 3°C |
| Net electronic noise | 1 mV |
| Diffuse attenuation coefficient | $0.015 \frac{1}{m}$ |

Table 6.1: Uncertainty parameters for Monte Carlo simulations.

6.3.3 Pose Detection Performance Evaluation

The performance of the pose detection system is evaluated in terms of two criteria:

1. Positioning accuracy of the UUV platform with respect to the light source for both steady-state and dynamic cases
2. Velocity estimation accuracy during the navigation

For the first criterion, the UUV platform, which is the optical detector array mounted on the moving tow carriage of the tow tank, is set in the water column at a pre-determined offset distance from the light source. Then, with a specified tow carriage acceleration and velocity, the UUV platform is actuated to a final position. In the dynamic tests, the goal is to detect the location of the center of the light source to within an accuracy of 0.5 m along the x -axis and to within 0.2 m along the y and z -axes when the UUV platform is both stationary and in motion. This is a requirement for both locating the target, (i.e. the docking station) and for a successful docking operation. The tolerances along the y and z -axes are more stringent than the error tolerance along the x -axis, as the UUV requires a certain accuracy in y and z -axes to enter into the docking station.

Two sets of experiments are conducted in order to verify the system performance. The first set of experiments has the UUV platform and the light source aligned in y and z -axes with an offset of 8.5 m in x -axis. The second set of experiments is conducted for the case when there are offsets of 0.6 m in y -axis and 0.8 m in z -axis. These offsets are chosen as the maximum possible offset specified by the calibration range in order to evaluate the system performance in its most limiting conditions.

For the second criterion (during the motion of the UUV platform), it is also important to estimate the velocity relative to the light source. Based on the velocity feedback obtained from the optical detector array, the UUV control system can control its speed during its navigation for a smoother entrance into the pole docking station. The velocity estimation

performance of the UUV platform is evaluated during the dynamic experiments that are conducted for pose estimates.

6.4 Calibration Results

The output signals from the photodiodes, based upon the light sources emitted light field intersecting the detector array, are to be used in pose detection and control algorithms. Therefore, the consistency of the photodiode readings is vital and need to be characterized. In order to observe the photodiode response, all of the photodiodes are fixed at a constant, 0.18 m distance from the halogen light source (PL-900 Fiber-Lite). The calibration results show that the photodiode readings are in the range from 291 to 300 mV and have mean value of 297.4 mV and standard deviation 2.41 mV. This result confirms that the photodiode measurements under the prescribed experimental conditions have very little variation. Regardless, these variations should still be taken into account in the pose detection algorithms.

In order to determine the temperature dependence of the SM05PD1A photodiode under water, its response to temperature variation was characterized for a specific light source, i.e. Z-Bolt SCUBA underwater dive laser which operates at wavelength of 532 nm. For calibration, the temperature is varied from 20°C to 70°C at 10°C increments. It is observed from the experiment that the voltage output from SM05PD1A decreases as the temperature increases. During the experiments, it was noted that at 70°C, the steam build-up from the water bath affects the amount of light incident on the photodiode. Therefore, this data point is considered as an outlier. By applying a linear fit line to the rest of the data points, temperature sensitivity was found to be 2 mV/°C where,

$$V_o(T) = -2T + 576 \quad (6.1)$$

Here $V_o(T)$ is the measured temperature (in voltage) and T is the temperature (in °C). Based

on the surrounding temperature in the environment, the temperature voltage readings can be adjusted to take into account varying temperature effects, which in turn, can be integrated in the pose detection and control algorithms.

The photodiode detector array system was investigated for noise and cross-talk that can exist because of the signal transmission between the SMA cables or in their connection to the reverse-bias circuitry. It is observed from the data that when there is no incident light on the other photodiodes, the noise level in the system contributed by the dark current, shot noise, background noise, quantification errors, cable transmission losses (including the 3.3 m SMA cables from the photodiodes to the reverse-bias circuitry and the serial communication losses) are in the range of 1 mV.

Underwater calibration procedure is conducted to develop algorithms for determining the pose and the velocity during UUV platform navigation. At each x -axis position, 25 images are sampled at different locations (5 different measurements along the y -axis ranging from -0.6 m to 0.6 m at 0.3 m increments and 5 different measurements along the z -axis ranging from 0 m to 0.8 m at 0.2 m increments), totaling 125 images for pose estimation calibration. In order to observe the variation in the photodiode readings, 200 different measurements are taken at each of the 125 locations. For each location, it is found that the standard variation in the photodiode readings is approximately 1% of the maximum photodiode intensity.

6.5 Stochastic Model Results

In order to predict the performance of the pose detection algorithms under varying environmental and hardware conditions, such as in Portsmouth Harbor, New Hampshire, a stochastic approach, (i.e., Monte Carlo analysis) is performed. The goal, here, is to evaluate the system performance when there is uncertainty in environmental conditions (diffuse attenuation coefficient and temperature variations) and hardware characteristics. The measurements of these parameters are either not always available or require extensive experimental work to obtain. The uncertainties in the environment and hardware affect the reliability

of the light intensity measurements and, thus, the pose output for each axis. Monte Carlo analysis is conducted to evaluate the system performance under these varying parameters.

Two sets of Monte Carlo analyses are conducted in this study. The first analysis compares experimental pose estimates to the model generated pose estimates. The simulations in the second analysis under the same detector trajectory (i.e. starting from $x=8.5$ m to $x=4.5$ m) the model generated nominal poses are calculated by changing the diffuse attenuation coefficient, temperature and hardware noise with sample size of, $N_S=2000$. The standard deviation of the hardware noise is set to 1% intensity of the photodiode with the maximum intensity. The Monte Carlo analysis results for x , y and z -axes are shown in Figure 6.11, respectively.

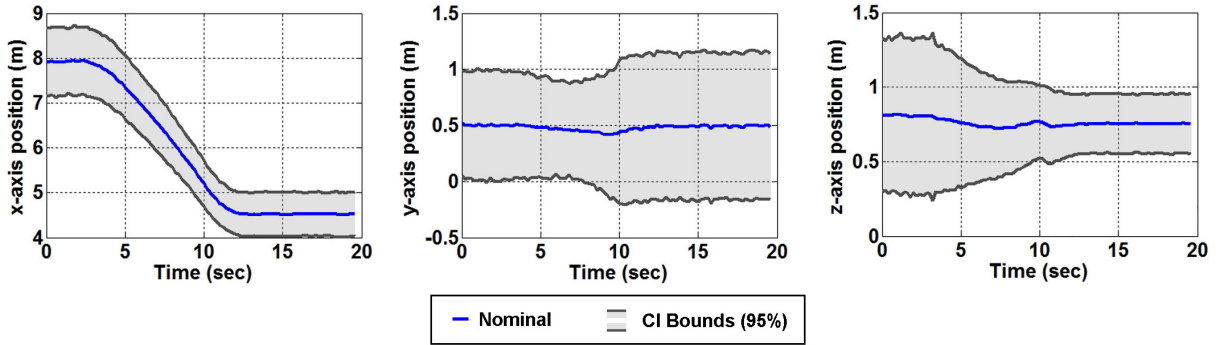


Figure 6.11: Monte Carlo generated CI bounds (95%).

The maximum observed uncertainty for x -axis is approximately around 0.78 m while it is 0.67 m and 0.56 m for y and z -axes respectively. The uncertainty bounds along the x -axis estimations do not exhibit much variation during the course of trajectory. However, for y -axis, the uncertainty decreases until $t=6.8$ sec. and then proceeds to increase as the detector approaches to its final position. For the z -axis, the uncertainty decreases with platform motion towards the light source and converges to a minimum value.

The second Monte Carlo simulation scenario is conducted under the scenario where a UUV motion is restricted to the $x - y$ plane and is given a predefined trajectory (from point A to point B) as shown in Figure 6.12. The light source is assumed to be at the origin.

Because the UUV navigates in x - y plane, it is likely that, the y -axis pose be misinterpreted as yaw motion. Thus, the capability of the detection algorithm to distinguish and quantify y -axis and yaw are also evaluated in this scenario. standard deviation of hardware noise is set to 0.5% intensity of the photodiode with the maximum intensity. The pitch angle is not taken into account in this study as the UUV is assumed to be built stable in pitch.

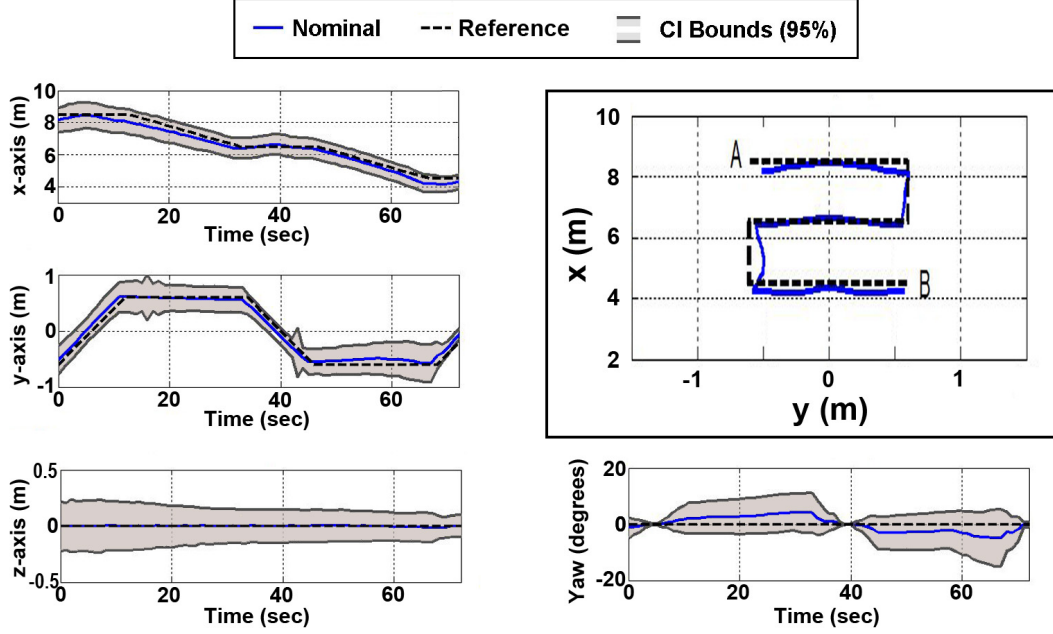


Figure 6.12: Monte Carlo Simulation results with 95% CI bounds for navigation in $x - y$ plane. (Top-left) Nominal x -axis pose estimates. Middle-left: y -axis estimation. (Bottom-left) z -axis estimation. (Top-right) UUV reference navigation in the $x - y$ plane and the nominal estimation. (Bottom Right) Yaw pose estimation.

6.6 Pose Detection Performance Evaluation

The success of the optical detector array depends on its pose and velocity estimates when the UUV platform is both stationary and approaching to the light source. There are several identifiers that can be used to estimate the pose. For x -axis pose estimation, the pose detection algorithm relies on the intensity of the middle photodiode. An exponential fit is applied to the intensity readings on the middle photodiode taken at $x=4.5$ m to $x=8.5$ m at

1 m increments, the center of the light source was aligned with the middle photodiode. For the estimation of y and z -axis offsets with respect to the light source, the algorithm relies on the image moments invariants calculations. For each pose, the image moments invariants algorithm yields a 3×3 matrix which indicates symmetry information of the sampled light field. The matrix is also used to develop the pose detection algorithms for y and z -axes offsets and fits linear-fit models to estimate the pose in the corresponding axes. Because the x -axis distance estimation solely relies on the middle photodiode intensity, the estimates decrease in accuracy as the relative offset between the light source and the middle photodiode increases. Thus, the pose estimation along the x -axis is corrected based on the y and z -axis pose estimates. The velocity estimation along the x -axis is obtained by calculating the time derivative of the initial x -axis pose estimates.

In order to validate the system performance for both stationary and dynamic cases, two types of experiments are conducted

1. the centers of the light source and UUV platform being aligned
2. the center of the light source and that of the UUV platform having a priori maximum offsets (i.e., at the maximum limits of the calibration scheme)

In both of these cases, the UUV platform is given an initial position of 8.5 m and a final position of 4.5 m with given a velocity of 0.5 m/s , acceleration and deceleration values of 0.2 m/s^2 .

Case 1: Aligned light source and UUV platform

In this case, the UUV platform is stationary at the beginning of the experiment at $x=8.5$ m for 5.5 s. Then, the tow tank is commanded to go to 4.5 m (Fig 6.13). There is no UUV platform offset along y and z -axes with respect to the light source and the velocity estimates are applied a moving average window of size 10.

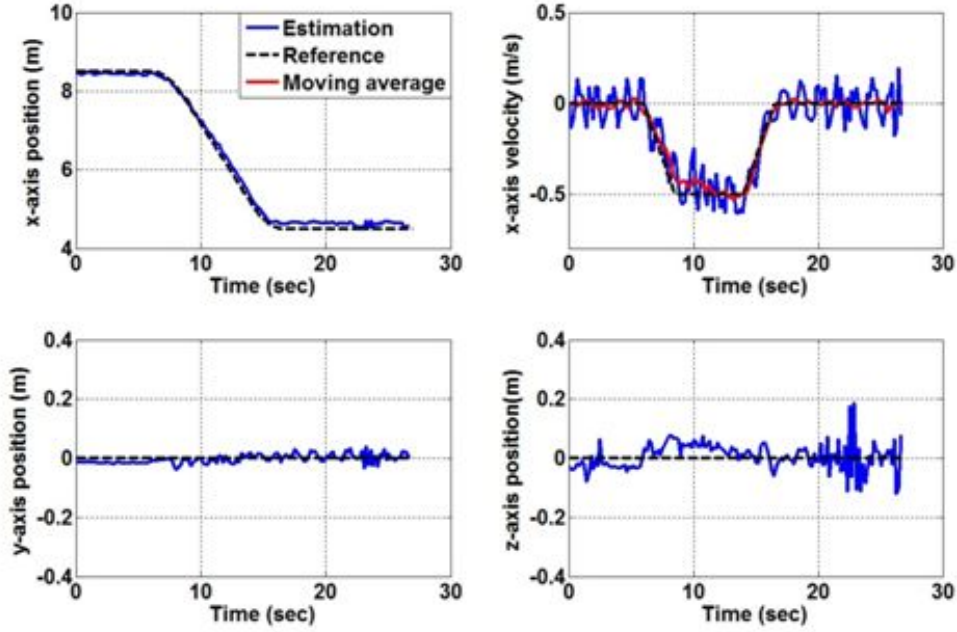


Figure 6.13: Empirical Pose detection for case 1: (Top left): Reference position, x -axis pose estimate. (Top right): Velocity reference, raw velocity estimates and moving average window of size 10 applied to the raw velocity estimates. (Bottom left): y -axis pose estimate. (Bottom right): z -axis pose estimate.

The results for the first experimental case show that x -axis pose estimate is accurate to within 0.15 m when both stationary and in motion. For y -axis pose, the pose estimates are very accurate throughout the experiment, staying within 0.05 m at all times. The z -axis pose estimates at the initial stage are quite accurate both at initial stage of $x=8.5$ m and during its approach to the light source, within 0.08 m error. Although pose estimates were fluctuating with high frequency when the platform comes to steady state, these fluctuations still stay within 0.2 m error. Because the velocity estimates are obtained by taking the time-derivative of the x -axis pose estimate, the velocity signal is prone to noise. However, by applying a moving average window of size 10, it is observed that the estimated velocity trend follows the reference velocity within a reasonable accuracy, less than 0.14 m/s.

Case 2: The UUV platform at maximum offset

The second experimental case is identical with the first experimental case but with the addition of y and z -axis offsets (Figure 6.14). In this experiment, y -axis offset is set to $+0.6$ m and z -axis offset is set to 0.8 m below the light source (1.8 m below the water surface). The UUV platform is commanded to move to the final x -axis position of 4.5 m from its initial x -axis position of 8.5 m away from the light source at 2.5 s. Again, a moving average window of sample size 10 is applied.

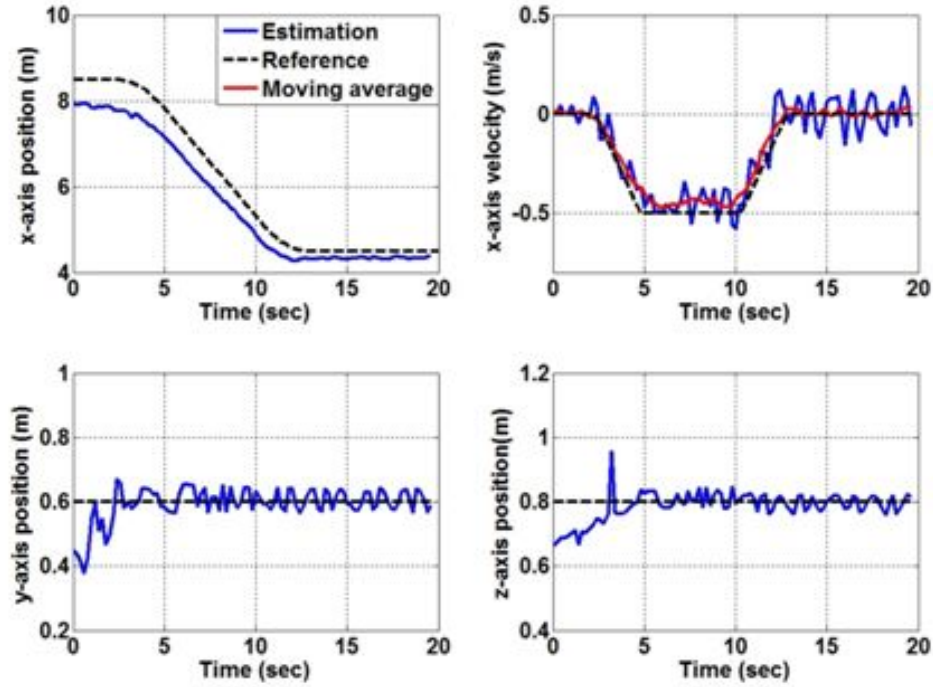


Figure 6.14: Empirical Pose detection for case 1: (Top left): Reference position, x -axis pose estimate. (Top right): Velocity reference, raw velocity estimates and moving average window of size 10 applied to the raw velocity estimates. (Bottom left): y -axis pose estimate. (Bottom right): z -axis pose estimate.

The results showed that the pose estimates along the x -axis start with a 0.5 m difference in the initial stationary state ($x=8.5$ m) and the estimation error reduces after the system goes to dynamic state. The error between the actual platform position and the estimation reduces to 0.15 m when the platform returns to a stationary state ($x=4.5$ m). The pose

estimates along the y and z -axis were within 0.2 m error in the initial stationary state ($x=8.5$ m) and are reduced significantly to 0.05 m in dynamic state and maintains it when returning back to a stationary state ($x=4.5$ m). The estimated velocity trend followed the predefined tow carriage velocity within maximum of 0.14 m/s error at all times.

6.7 Discussion of Experimental Pose Detection Results

TPU of the pose estimation was calculated using the Monte Carlo approach. The simulation results show that two of the most influential factors affecting the study is the turbidity of the water column and the hardware noise. These two components affect the photodiode intensity readings significantly. As a result, the uncertainty of the poses can increase drastically. The temperature variation results obtained from the calibrations was not found to be a significant factor affecting the photodiode intensity readings.

The results confirm that the hardware and detection system of the detector array can be applied in static-dynamic system applications, e.g. for both funnel-docking and pole-docking stations. Evaluation of the feedback signal from the experimental results showed that the current design can estimate the translational pose within 0.5 m along the x -axis, and 0.2 m along the y and z -axes. These results suggest that the proposed system has strong potential in both types of UUV docking station applications that is planned to be implemented in Portsmouth Harbor, New Hampshire.

Image moments invariants method is utilized in this research in order to develop pose detection algorithms to detect and quantify the relative motion between the UUV and the light source. The pose detection algorithms are developed when there is no noise in the system. The algorithms can provide very accurate estimations when the noise is introduced to the system (standard deviation is 0.5% and is 1% of the intensity of the photodiode with the maximum intensity). This shows that algorithm has specific tolerance to noise. However, when excessive noise is added into the system in the form of hardware noise (e.g. standard deviation of the noise is more than 1% of the intensity value of the photodiode with the

maximum intensity), the pose detection accuracy decreases.

It is also important to distinguish between the y -axis translation and yaw motion for the control system performance. The results suggest that pose detection algorithms can provide reasonable discrimination between y -axis translation and yaw when only y -axis translation exists. However, in some cases, y -axis translation values can be interpreted as small angle yaw rotations (less than 5° in the nominal case). At these values, the photodiode intensity values for small angle yaw rotation and respective y -axis values are very similar, if not impossible making it difficult to distinguish the motions from each other. This small-angle is verified for the case for pure yaw motion, (i.e. no y -axis translation) by conducting a Monte Carlo analysis (Figure 6.15).

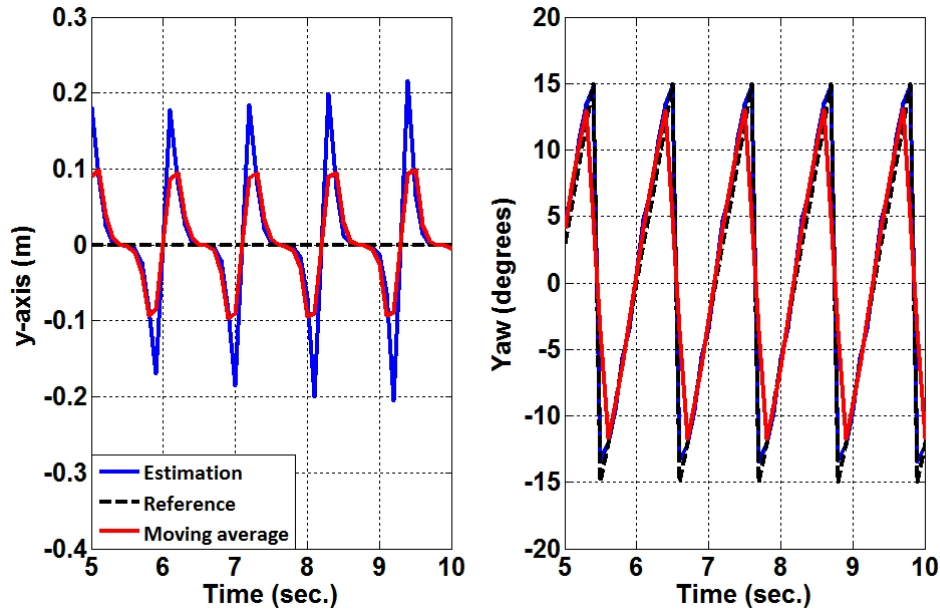


Figure 6.15: Yaw and y -axis cross-talk when there is only yaw motion.

It is observed from the results in Figure 6.15 that between rotations of ± 5 degrees, yaw motion was interpreted as y -axis motion. These results from both simulation cases confirm that at small yaw angle detections, the control system requires an additional step to validate UUV yaw motion. Utilizing more than a single light source can also decrease this cross-talk effect.

When calculating the TPU results for the environmental conditions in Portsmouth Harbor, the range considerations of parametric uncertainties in environmental conditions should be increased. The parameters that are expected show greater variation in the Portsmouth Harbor than in UNH Ocean Engineering facilities are the diffuse attenuation coefficient due to turbidity. In addition, scattering, which is not considered in the model used in this study, can potentially be a significant factor that affects the observed beam pattern. Although it is not found to be a significant factor, the seasonal water temperature variations in Portsmouth Harbor should also be taken into account in the pose detection algorithms. Otherwise, these effects are expected to increase the overall uncertainty in pose estimation. Another important parameter to be considered during implementation of such a system in Portsmouth Harbor are disturbances such as current and waves. In terms of mechanical design and construction, docking platform should be constructed to withstand these disturbances. In addition, the UUV controller should be able to compensate for the potential disturbances.

The experimental y and z -axis pose outputs from the optical detector array exhibit high frequency behavior at times. One potential contributor to these phenomena is the vibration associated with the tow carriage during the motion. The vibration can cause the crabbing behavior and affect the photodiode intensity results. The second potential contributor is the drag force that the optical detector array experiences during the motion which causes differences between the calibration measurements and the test case measurements. These two contributors should be measured to compensate for the effects of these in the detection system for future study. The third potential contributor is a result of the models that are developed to estimate the pose using the image moment invariants algorithm matrix elements. The model generated uncertainty is coupled into TPU in the Monte Carlo analysis. A more detailed study analyzing the effect of the uncertainty of these models into the overall system should be further investigated for future study. The velocity of the UUV platform can be estimated within 0.14 m/s of the actual velocity. However, because the velocity estimation relies on the estimated pose, the signal is prone to noise. Thus, in order to utilize the

estimated velocity signal for feedback in the UUV control system, for future experiments, the signals should be filtered for a smoother velocity reference, which is an important from a control systems implementation.

Hardware improvements such as using a higher resolution A/D boards and operation in clearer waters can improve the pose detection results. From the architectural perspective, it is possible to design a larger or smaller detector array that can fit to a variety of UUV classes, both for Autonomous Underwater Vehicles (AUVs) or Remotely Operated Vehicles (ROVs), for a variety of pose detection applications. The major design features of the hemispherical detector array are an effective radius of 0.19 m and a 5 x 5 array of photodiodes. Increasing the diameter of the array, using additional photodiode elements and using different detector array geometry other than a hemisphere can increase the pose resolution. The placement of the acrylic fixtures on the optical detector array also affects the reliability of the pose estimates.

CHAPTER 7

DISCUSSION

In order to fully utilize the optical based sensor feedback in underwater, characterization of the underwater environment is essential. Experiments conducted in wave and tow tank show that the effective range between the light source and the light detector is dependent on the diffuse attenuation coefficient as it affects the light intensity during its travel under water. In addition, the size of the beam pattern emitted from the light source also has a role in determining the usable portion of the light perpendicular to the optical axis. The approximate dimensions of the optical detector array can be determined based on the location where the light intensity starts to decrease to a certain value such as FWHM.

Because a single light source with a Gaussian light intensity profile is assumed in this study, it is not possible to detect roll changes. In addition, most UUVs are built stable in roll and pitch, i.e. for rotations in these DOFs is limited. Therefore, roll detection is not taken into account in this study. However, the use of multiple light sources or light sources with different intensity patterns other than Gaussian intensity profile has the potential to add roll detection capability to the detection system. The maximum effective range between the light source and the light detector is maintained at 8.5 m in this study. Utilizing lasers, e.g. a green laser at 532 nm wavelength, can increase the operational range significantly.

The detector array can detect translational changes of 0.2 m and rotational changes (pitch and yaw) of 10° . A larger array size is needed to detect smaller changes. However, a larger array size may not be suitable for all UUV types. While some UUVs, such as a larger work-class ROVs, can accommodate array sizes with larger dimensions, for the observation class

ROVs or an AUV, the mechanical stability can degrade by changing locations of center of gravity and center of buoyancy. Another factor affecting the detection capability is the light source characteristics. A narrow beam light source can provide better resolution detections both in translation and rotation. Light sources with different intensity profiles other than Gaussian can also change the detection capabilities.

Pose feedback is obtained by converting the beam pattern sampled on an optical detector array into usable pose information through image processing algorithms. Among these algorithms used in this study are phase correlation and log-polar transform, Spectral Angle Mapper (SAM), and image moments invariants. Phase correlation and log polar transform algorithm are able to yield reliable translation estimations. However, these methods are not practical for rotational estimation due to the symmetry of the sampled images. SAM algorithm proves to be useful for verifying the pose detection capability of the array. However, in terms of control algorithm development perspective, the SAM algorithm requires extensive calibration. The SAM algorithm also increases the required number of characteristic image parameters to distinguish between varying types of motion. This can increase the processing time and therefore result in a slower UUV thruster response both of which is undesirable. Image moments invariants algorithm yields reliable estimates for both translation and rotation. In addition, the processing time to obtain pose estimates is shorter due to the use of linear models obtained from the calibration procedure. In addition, the calibration procedure is not as lengthy as the SAM algorithm. Therefore, image moments invariants approach is chosen to extract the pose from a sampled image.

Two types of controllers are evaluated in this study, Proportional-Integral-Derivative (PID) and Sliding Mode Controller (SMC). The response characteristics such as overshoot are identified in conjunction with the feedback obtained from the image moments invariants algorithm. The analytical results for a static-dynamic system suggest that PID control results in excessive overshoot which cannot be tolerated in this application. When overshoot occurs during alignment with the light source, a UUV loses line-of-sight and, hence, com-

munication with the guiding beacon. The overshoot can be tolerated in x-axis but for y and z-axis control, this must be avoided. Control simulations with SMC suggest that satisfactory performance may be obtained in both static-dynamic and dynamic-dynamic system scenarios. However, a time-varying boundary layer must be implemented with SMC in order to avoid chatter. In addition, SMC requires full-state feedback, i.e. it should receive measurements for both position and velocity. The developed optical detector array can yield only pose information. The time-derivative of the pose measurements must be taken and filtered to provide the controller a smooth reference. Overshoot is not observed in SMC which makes it a more viable choice over PID control. For the controllers that require extensive knowledge about the vehicle model and parameters, vehicle system identification should be empirically determined. Other type of controllers such as H_∞ and adaptive controllers should also be investigated for their practicality in UUV control with optical feedback applications. Additional sensors that measure disturbances and the implementation of observers can also contribute to a better control system.

It is also found that satisfactory control performance can be obtained by using a minimal 5 x 5 array and, thus, use of a larger size array is not necessary. This is an important finding as it eliminates the costs associated with extra hardware particularly the number of required photodiodes, which in turn require large number of ADC boards, extra OBCs and reverse-bias circuitry. This also reduces the logistical complexity of hardware implementation.

The uncertainty analysis through Monte Carlo simulations reveals that the most important factors affecting pose estimation accuracy is the turbidity in the water and environmental and sensor noise. It is also observed that the temperature variation does not have a significant effect on the estimations. Monte Carlo analysis is performed for 2000 realizations with varying diffuse attenuation coefficients, hardware noise and temperature values. The samples for these parameters are generated with respect to normal distributions with an assumed known mean and standard deviation. The pose detection algorithms are developed for zero hardware noise in the system and the algorithms prove to be robust to noise with

a standard deviation more than 1% of the intensity value of the photodiode with the maximum intensity. However, as expected, increasing the amount of hardware noise results in additional uncertainty in the system. If the background noise in the environment is excessive or turbidity is high, the algorithms may not yield accurate estimations. It should be noted that, this is an inherent issue with this application.

It is also of importance to distinguish motion that occurs in the same plane. For example, y -axis translation and yaw rotation act on the same plane and therefore, is difficult to distinguish between these different motion types. After calibration, it is found that for the most part of the range under test, i.e. 15° , y -axis translation and yaw rotation can be distinguished. The failure to discriminate between y -axis translation and yaw rotation occurs when yaw is less than 5° . At this angle, the corresponding intensity values on the optical detector array are almost identical to the translational counterpart, making distinguishing between these two motion types difficult, especially in turbid and/or noisy environments.

The accuracy of the detections is tested for two types of potential docking applications, i.e. funnel docking and pole docking. In funnel docking applications, an appropriate UUV entrance trajectory is more important than its speed. Therefore, for this application pose estimation accuracy is critical. For pole docking applications, accurate UUV velocity estimates is more critical. The pose detection algorithms are developed based on sampled beam patterns for a total number of 125 positions. Based on this set of calibrations, to estimate the pose, linear models are developed utilizing the image moments invariants matrix identities. The performance of the optical detector array is evaluated for both accuracy of pose estimates and velocity estimates. The experimental evaluation of the pose detection of optical detector array demonstrates that the developed system can determine the pose to within 0.5 m accuracy along the x -axis, and 0.2 m in both y and z -axes. Velocity estimates are accurate to within 0.14 m/s of the actual tow carriage velocity.

There are several factors that contribute to the accuracy of the pose detections using optical feedback. The physical affects that contribute to the errors in the measurements

include the vibration of the towing mechanism on the wave and tow tank and the drag force exerted on the optical detector array. These effects cause array displacement and, as a result, the real-time intensity measurements differ significantly from the offline calibration measurements at the same locations. The setup used in the experiments consists of a single 80/20 aluminum frame submerged into the water. One potential solution to minimize these effects on the accuracy of pose estimates is to use a more stable setup for calibrations. In addition, the placement of the acrylic fixtures on the hemispherical surface also is a source of systematic error for pose estimates. Another potential contribution to pose estimation errors is the linear models obtained from the calibration procedure through image moments invariants algorithms. Because the calibration models are linear, the pose estimates are not equally accurate at each position across the experimental range.

In the real-world implementation of such a system such as in Portsmouth Harbor, pose estimation uncertainties are expected to increase due to increased diffuse attenuation coefficient as a result of increased turbidity in the harbor. In addition, background noise which can be evident in the form of sediment plumes is expected to increase the pose uncertainty. By evaluating the data from NOAA Charts [97]- [98], environmental disturbances such as waves and currents are also expected to increase in Portsmouth Harbor, the docking station should be constructed to withstand these environmental forces. The UUV control system should also compensate for these disturbances while navigating into the docking station.

CHAPTER 8

CONCLUSIONS

This study has shown the proof of concept of an optical detection system that can yield satisfactory pose estimation results. Pose detection capabilities and limitations have been demonstrated for static-dynamic and dynamic-dynamic systems through simulation and experiments. The limitations of the system in real-world conditions have been identified.

In order to design such a system, as the first step, underwater environment was characterized in order to evaluate the feasibility of a detection and control system using optical feedback. From the experiments, it was found that in 500-550 nm wavelength band, the light transmission is at maximum. FWHM radius of the beam expands from 0.3 m to 0.4 m from 4.5 m to 8.5 m distance. These findings yield a foundation for hardware selection and dimensions of the proposed optical detector array design.

Two types of optical array geometries were evaluated for pose detection in underwater, i.e. planar and curved arrays. The selection criteria for the optical array design include the following:

1. The array should distinguish changes in position and orientation based on a single light source. The array is expected to distinguish motion in 5-DOF, i.e. translations in x , y and z -axis as well as pitch and yaw. Due to the beam symmetry emitted from a single light source, it is not possible to detect roll.
2. The array should have minimum number of optical detectors that can yield pose information, reduce processing time and reduce the costs. In order to evaluate the performance criteria, a numerically based simulator that takes the relative geometry

between the light source and the detector as inputs, the water turbidity, hardware and background noise was developed.

SAM algorithm evaluated the changes in position and orientation. Using a 21×21 array, it was shown that the translational changes of 0.2 m and rotational shifts of 10° can be detected. The curved array was also shown to be more sensitive to the changes in rotation whereas the two arrays performed similar for the translational shifts. Further simulations showed that a minimum of 5×5 array is required to distinguish changes in 5-DOF. Experimental measurements verified the accuracy of the simulator generated images.

The goal of this research is to use the optical feedback generated from the optical detector array in control applications. Pose detections and control algorithms were developed in order to dynamically position the UUV in static-dynamic system, i.e. a fixed light source as a guiding beacon and a UUV, and dynamic-dynamic system, i.e. moving light source mounted on the crest of a leader UUV and a follower UUV follows its path. The algorithms were evaluated based on processing time, positional accuracy and dependence on the environmental characteristics. A hemispherical array of sizes 5×5 and 21×21 was used to develop the algorithms. Evaluation of image processing techniques such as log-polar transform and phase correlation, SAM and image moments invariants demonstrated that image moments invariants method is the most suitable algorithm in terms of processing time and positional accuracy. The dependence on the noise is an inherent issue for this application and under excessive noise the accuracy of the results degrades for all of the algorithms. Evaluation of PID and SMC for static-dynamic and dynamic-dynamic cases demonstrated that PID is not suitable for this application as it creates an overshoot during dynamic positioning, causing the UUV to lose line of sight with the light source. SMC on the other hand did not yield excessive oscillations and showed satisfactory performance for both static-dynamic and dynamic-dynamic applications. Analysis of the effect of detector number on the array revealed that a 5×5 detector array is sufficient to generate pose feedback to be used in UUV control applications.

After analytical results that compare the effect of detector size, geometry, image processing algorithms and control algorithms on the accuracy of pose estimations, the optical detector array was experimentally built. The final prototype consists of a hemispherical 5 x 5 array with an effective radius of 0.19 m. The underwater calibrations were conducted for 125 different positions in x , y and z -axis. Pose detection algorithms were developed based on the calibration results using image moments invariants algorithm. Underwater experiments conducted in wave and tow tank showed that pose detection accuracy was within 0.3 m in x -axis and it was within 0.1 m in y and z -axis. The velocity estimations were also within 0.1 m/s. The stochastic assessment of the pose estimations was done using Monte Carlo simulations. The Monte Carlo simulation results show that the experimental pose estimations are within model generated CI bounds (95%). It was also demonstrated there is reasonable discrimination power between y -axis translation and yaw rotation. The faulty detections were small angle yaw rotation less than 5° . The results also demonstrate that at the extreme calibration conditions, the x -axis pose estimation uncertainty (95%) was on the order of 1.5 m, y -axis pose estimation uncertainty was 1.3 m and z -axis pose uncertainty was on the order of 1 m. In the field implementation, i.e. in Portsmouth Harbor, the pose detection uncertainty in 4-DOFs, x , y , z and yaw, are expected to increase due to higher turbidity and environmental disturbances such as waves, currents.

LIST OF REFERENCES

- [1] HJ Curti, Gerardo G Acosta, and OA Calvo. Autonomous underwater pipeline inspection in autotracker project: the simulation module. In *Oceans 2005-Europe*, volume 1, pages 384–388. IEEE, 2005.
- [2] Gabrielle Inglis, Clara Smart, Ian Vaughn, and Chris Roman. A pipeline for structured light bathymetric mapping. In *Intelligent Robots and Systems (IROS), 2012 IEEE/RSJ International Conference on*, pages 4425–4432. IEEE, 2012.
- [3] DB Edwards, TA Bean, DL Odell, and MJ Anderson. *A leader-follower algorithm for multiple AUV formations*. IEEE, 2004.
- [4] James Jalbert, John Baker, John Duchesney, Paul Pietryka, William Dalton, DR Blidberg, Steve Chappell, Robert Nitzel, and Ken Holappa. A solar-powered autonomous underwater vehicle. In *Oceans 2003. Proceedings*, volume 2, pages 1132–1140. IEEE, 2003.
- [5] Michael J Hamilton, Stephanie Kemna, and David Hughes. Antisubmarine warfare applications for autonomous underwater vehicles: the glint09 sea trial results. *Journal of Field Robotics*, 27(6):890–902, 2010.
- [6] Scott Willcox, Dani Goldberg, Jerome Vaganay, and J Curcio. Multi-vehicle cooperative navigation and autonomy with the bluefin cadre system. In *Proceedings of the International Federation of Automatic Control Conference (IFAC-06)*, 2006.
- [7] Joseph Curcio, John Leonard, Jerome Vaganay, Andrew Patrikalakis, Alexander Bahr, David Battle, Henrik Schmidt, and Matthew Grund. Experiments in moving baseline navigation using autonomous surface craft. In *OCEANS, 2005. Proceedings of MT-S/IEEE*, pages 730–735. IEEE, 2005.
- [8] Ken Teo, Edgar An, and PJ Beaujean. A robust fuzzy autonomous underwater vehicle (auv) docking approach for unknown current disturbances. *Oceanic Engineering, IEEE Journal of*, 37(2):143–155, 2012.
- [9] Brett W Hobson, Robert S McEwen, Jon Erickson, Thomas Hoover, Lance McBride, Farley Shane, and James G Bellingham. The development and ocean testing of an auv docking station for a 21” auv. In *OCEANS 2007*, pages 1–6. IEEE, 2007.
- [10] Youmin Zhang and Hasan Mehrjerdi. A survey on multiple unmanned vehicles formation control and coordination: normal and fault situations. In *Unmanned Aircraft Systems (ICUAS), 2013 International Conference on*, pages 1087–1096. IEEE, 2013.

- [11] M Anthony Lewis and Kar-Han Tan. High precision formation control of mobile robots using virtual structures. *Autonomous Robots*, 4(4):387–403, 1997.
- [12] Yoko Watanabe. Coordinated control of multiple uavs: Theory and flight experiment. In *AIAA Guidance Navigation & Control (GNC) Conference*.
- [13] Jonathan RT Lawton, Randal W Beard, and Brett J Young. A decentralized approach to formation maneuvers. *Robotics and Automation, IEEE Transactions on*, 19(6):933–941, 2003.
- [14] Rongxin Cui, Shuzhi Sam Ge, Bernard Voon Ee How, and Yoo Sang Choo. Leader–follower formation control of underactuated autonomous underwater vehicles. *Ocean Engineering*, 37(17):1491–1502, 2010.
- [15] Jaydev P Desai, Jim Ostrowski, and Vijay Kumar. Controlling formations of multiple mobile robots. In *Robotics and Automation, 1998. Proceedings. 1998 IEEE International Conference on*, volume 4, pages 2864–2869. IEEE, 1998.
- [16] Naomi Ehrich Leonard and Edward Fiorelli. Virtual leaders, artificial potentials and coordinated control of groups. In *Decision and Control, 2001. Proceedings of the 40th IEEE Conference on*, volume 3, pages 2968–2973. IEEE, 2001.
- [17] Andrew Howard, Maja J Matarić, and Gaurav S Sukhatme. Mobile sensor network deployment using potential fields: A distributed, scalable solution to the area coverage problem. In *Distributed Autonomous Robotic Systems 5*, pages 299–308. Springer, 2002.
- [18] Jaydev P Desai, James P Ostrowski, and Vijay Kumar. Modeling and control of formations of nonholonomic mobile robots. *Robotics and Automation, IEEE Transactions on*, 17(6):905–908, 2001.
- [19] Ben Allen, Tom Austin, Ned Forrester, Rob Goldsborough, Amy Kukulya, Greg Packard, Mike Purcell, and Roger Stokey. Autonomous docking demonstrations with enhanced remus technology. In *OCEANS 2006*, pages 1–6. IEEE, 2006.
- [20] JC Evans, KM Keller, JS Smith, P Marty, and OV Rigaud. Docking techniques and evaluation trials of the swimmer auv: an autonomous deployment auv for work-class rovs. In *OCEANS, 2001. MTS/IEEE Conference and Exhibition*, volume 1, pages 520–528. IEEE, 2001.
- [21] Toshifumi Fukasawa, Toshihito Noguchi, Tadayuki Kawasaki, and Makoto Baino. ”marine bird”, a new experimental auv with underwater docking and recharging system. In *OCEANS 2003. Proceedings*, volume 4, pages 2195–2200. IEEE, 2003.
- [22] Bruno Jouvencel, Olivier Parodi, and Xianbo Xiang. Coordinated formation control of multiple autonomous underwater vehicles for pipeline inspection. *International Journal of Advanced Robotic Systems*, 7(1):75–84, 2010.
- [23] Pedro Calado and Joao Sousa. Leader-follower control of underwater vehicles over acoustic communications. In *OCEANS, 2011 IEEE-Spain*, pages 1–6. IEEE, 2011.

- [24] Pan Feng. Leader-follower cooperative navigation with communication delays for multi auvs. In *Signal Processing, Communications and Computing (ICSPCC), 2011 IEEE International Conference on*, pages 1–5. IEEE, 2011.
- [25] Saba Emrani, Alireza Dirafzoon, and Heidar A Talebi. Leader-follower formation control of autonomous underwater vehicles with limited communications. In *Control Applications (CCA), 2011 IEEE International Conference on*, pages 921–926. IEEE, 2011.
- [26] Ethem M Sozer, Milica Stojanovic, and John G Proakis. Underwater acoustic networks. *Oceanic Engineering, IEEE Journal of*, 25(1):72–83, 2000.
- [27] SM Smith and D Kronen. Experimental results of an inexpensive short baseline acoustic positioning system for auv navigation. In *OCEANS’97. MTS/IEEE Conference Proceedings*, volume 1, pages 714–720. IEEE, 1997.
- [28] AJ Plueddemann, AL Kukulya, R Stokey, and Lee Freitag. Autonomous underwater vehicle operations beneath coastal sea ice. *Mechatronics, IEEE/ASME Transactions on*, 17(1):54–64, 2012.
- [29] Pedro Tiago Martins Batista, Carlos Silvestre, and Paulo Oliveira. Ges integrated lbl/usbl navigation system for underwater vehicles. In *CDC*, pages 6609–6614, 2012.
- [30] Bradley G Boone, Jonathan R Bruzzi, Wesley P Millard, Karl B Fielhauer, Bernard E Kluga, Christian W Drabenstadt, and Robert S Bokulic. Optical communications development for spacecraft applications: recent progress at jhu/apl. In *Aerospace Conference, 2005 IEEE*, pages 1570–1582. IEEE, 2005.
- [31] Eric Y Chan, Jeff C Adams, Jonathan M Saint Clair, Kenneth A Morrison, and Martin Sosa. Application of cots high-power laser diodes and driver for a free-space laser communication terminal. In *Optoelectronics and High-Power Lasers & Applications*, pages 54–67. International Society for Optics and Photonics, 1998.
- [32] Peter G Goetz, William S Rabinovich, G Charmaine Gilbreath, Rita Mahon, Mike S Ferraro, Lee Swingen, Robert J Walters, Scott R Messenger, Linda M Wasiczko, James Murphy, et al. Multiple quantum well based modulating retroreflectors for inter-and intra-spacecraft communication. In *SPIE Optics+ Photonics*, pages 63080A–63080A. International Society for Optics and Photonics, 2006.
- [33] Linda M Wasiczko, Harris R Burris, N Glenn Creamer, Rita Mahon, Christopher Moore, Lee Swingen, James Murphy, Mena Stell, Brad E Pinney, Peter Goetz, et al. Optical communication and navigation for spacecraft docking using modulating retroreflectors. In *Optics & Photonics 2005*, pages 58920E–58920E. International Society for Optics and Photonics, 2005.
- [34] Curtis D Mobley. *Light and water: Radiative transfer in natural waters*. Academic press, 1994.

- [35] Marek Doniec, Carrick Detweiler, Iuliu Vasilescu, and Daniela Rus. Using optical communication for remote underwater robot operation. In *Intelligent Robots and Systems (IROS), 2010 IEEE/RSJ International Conference on*, pages 4017–4022. IEEE, 2010.
- [36] JH Smart. Underwater optical communications systems part 1: variability of water optical parameters. In *Military Communications Conference, 2005. MILCOM 2005. IEEE*, pages 1140–1146. IEEE, 2005.
- [37] John W Giles and Isaac N Bankman. Underwater optical communications systems. part 2: basic design considerations. In *Military Communications Conference, 2005. MILCOM 2005. IEEE*, pages 1700–1705. IEEE, 2005.
- [38] Brandon Cochenour, Linda Mullen, and Alan Laux. Spatial and temporal dispersion in high bandwidth underwater laser communication links. In *Military Communications Conference, 2008. MILCOM 2008. IEEE*, pages 1–7. IEEE, 2008.
- [39] Brandon M Cochenour, Linda J Mullen, and Alan E Laux. Characterization of the beam-spread function for underwater wireless optical communications links. *Oceanic Engineering, IEEE Journal of*, 33(4):513–521, 2008.
- [40] Frank Hanson and Mark Lasher. Effects of underwater turbulence on laser beam propagation and coupling into single-mode optical fiber. *Applied optics*, 49(16):3224–3230, 2010.
- [41] Curtis D Mobley, Bernard Gentili, Howard R Gordon, Zhonghai Jin, George W Kattawar, Andre Morel, Phillip Reinersman, Knut Stamnes, and Robert H Stavn. Comparison of numerical models for computing underwater light fields. *Applied Optics*, 32(36):7484–7504, 1993.
- [42] DJ Bogucki, J Piskozub, M-E Carr, and GD Spiers. Monte carlo simulation of propagation of a short light beam through turbulent oceanic flow. *Optics express*, 15(21):13988–13996, 2007.
- [43] Chadi Gabriel, M Khalighi, Salah Bourennane, Pierre Leon, and Vincent Rigaud. Channel modeling for underwater optical communication. In *GLOBECOM Workshops (GC Wkshps), 2011 IEEE*, pages 833–837. IEEE, 2011.
- [44] Frank C Eliot. Geometric design of linear array detectors. *Electron Devices, IEEE Transactions on*, 21(10):613–616, 1974.
- [45] Seung-Bum Rim, Peter B Catrysse, Rostam Dinyari, Kevin Huang, and Peter Peumans. The optical advantages of curved focal plane arrays. *Optics Express*, 16(7):4965–4971, 2008.
- [46] Iuliu Vasilescu, Paulina Varshavskaya, Keith Kotay, and Daniela Rus. Autonomous modular optical underwater robot (amour) design, prototype and feasibility study. In *Robotics and Automation, 2005. ICRA 2005. Proceedings of the 2005 IEEE International Conference on*, pages 1603–1609. IEEE, 2005.

- [47] Firat Eren, ML Thein, Barbaros Celikkol, Shachak Pe'eri, and Jud DeCew. Distance detection of unmanned underwater vehicles by utilizing optical sensor feedback in a leader-follower formation. In *Oceans, 2012*, pages 1–6. IEEE, 2012.
- [48] Firat Eren, Shachak Pe'eri, and May-Win Thein. Characterization of optical communication in a leader-follower unmanned underwater vehicle formation. In *SPIE Defense, Security, and Sensing*, pages 872406–872406. International Society for Optics and Photonics, 2013.
- [49] Steve Cowen, Susan Briest, and James Dombrowski. Underwater docking of autonomous undersea vehicles using optical terminal guidance. In *OCEANS'97. MTS/IEEE Conference Proceedings*, volume 2, pages 1143–1147. IEEE, 1997.
- [50] Felix Schill, Uwe R Zimmer, and Jochen Trumpf. Visible spectrum optical communication and distance sensing for underwater applications. In *Proceedings of ACRA*, volume 2004, pages 1–8, 2004.
- [51] N Farr, A Bowen, J Ware, C Pontbriand, and M Tivey. An integrated, underwater optical/acoustic communications system. In *OCEANS 2010 IEEE-Sydney*, pages 1–6. IEEE, 2010.
- [52] N Fair, AD Chave, Lee Freitag, James Preisig, SN White, Dana Yoerger, and F Sonnichsen. Optical modem technology for seafloor observatories. In *OCEANS 2006*, pages 1–6. IEEE, 2006.
- [53] Marek Doniec, Michael Angermann, and Daniela Rus. An end-to-end signal strength model for underwater optical communications. *Oceanic Engineering, IEEE Journal of*, 38(4):743–757, 2013.
- [54] Marek Doniec, Iuliu Vasilescu, Mandar Chitre, Carrick Detweiler, Matthias Hoffmann-Kuhnt, and Daniela Rus. Aquaoptical: A lightweight device for high-rate long-range underwater point-to-point communication. In *OCEANS 2009, MTS/IEEE Biloxi-Marine Technology for Our Future: Global and Local Challenges*, pages 1–6. IEEE, 2009.
- [55] Iuliu Vasilescu, Keith Kotay, Daniela Rus, Matthew Dunbabin, and Peter Corke. Data collection, storage, and retrieval with an underwater sensor network. In *Proceedings of the 3rd international conference on Embedded networked sensor systems*, pages 154–165. ACM, 2005.
- [56] Pedro Batista, Carlos Silvestre, and Paulo Oliveira. A two-step control strategy for docking of autonomous underwater vehicles. In *American Control Conference (ACC), 2012*, pages 5395–5400. IEEE, 2012.
- [57] Michael D Feezor, F Yates Sorrell, Paul R Blankinship, and James G Bellingham. Autonomous underwater vehicle homing/docking via electromagnetic guidance. *Oceanic Engineering, IEEE Journal of*, 26(4):515–521, 2001.

- [58] Robert S McEwen, Brett W Hobson, Lance McBride, and James G Bellingham. Docking control system for a 54-cm-diameter (21-in) auv. *Oceanic Engineering, IEEE Journal of*, 33(4):550–562, 2008.
- [59] Pan-Mook Lee, Bong-Hwan Jeon, and Chong-Moo Lee. A docking and control system for an autonomous underwater vehicle. In *OCEANS’02 MTS/IEEE*, volume 3, pages 1609–1614. IEEE, 2002.
- [60] Pakpong Jantapremjit and Philip A Wilson. Control and guidance for homing and docking tasks using an autonomous underwater vehicle. In *Intelligent Robots and Systems, 2007. IROS 2007. IEEE/RSJ International Conference on*, pages 3672–3677. IEEE, 2007.
- [61] Jonathan Evans, Paul Redmond, Costas Plakas, Kelvin Hamilton, and David Lane. Autonomous docking for intervention-auvs using sonar and video-based real-time 3d pose estimation. In *Oceans 2003. Proceedings*, volume 4, pages 2201–2210. IEEE, 2003.
- [62] Hayato Kondo, Kenji Okayama, Jin-Kyu Choi, Takeo Hotta, Masaki Kondo, Tadatsugi Okazaki, Hanumant Singh, Zizhen Chao, Kazuhiko Nitadori, Masao Igarashi, et al. Passive acoustic and optical guidance for underwater vehicles. In *OCEANS, 2012-Yeosu*, pages 1–6. IEEE, 2012.
- [63] Szymon Krupinski, Francesco Maurelli, Gabriel Grenon, and Yvan Petillot. Investigation of autonomous docking strategies for robotic operation on intervention panels. In *OCEANS 2008*, pages 1–10. IEEE, 2008.
- [64] Thor I Fossen. *Guidance and control of ocean vehicles*, volume 199. Wiley New York, 1994.
- [65] TI Fossen. Marine control systems: Guidance, navigation and control of ships, rigs, and underwater vehicles. *Trondheim, Norway: Marine Cybernetics*, 2002.
- [66] Thor I Fossen. *Handbook of marine craft hydrodynamics and motion control*. John Wiley & Sons, 2011.
- [67] Suguru Arimoto. Stability and robustness of pid feedback control for robot manipulators of sensory capability. In *Robotics Research, 1st Int. Symp.*, pages 783–799. MIT Press, 1984.
- [68] Wallace M Bessa, Max S Dutra, and Edwin Kreuzer. Depth control of remotely operated underwater vehicles using an adaptive fuzzy sliding mode controller. *Robotics and Autonomous Systems*, 56(8):670–677, 2008.
- [69] Jean-Jacques E Slotine, Weiping Li, et al. *Applied nonlinear control*, volume 60. Prentice-Hall Englewood Cliffs, NJ, 1991.
- [70] Thor Inge Fossen. *Nonlinear modelling and control of underwater vehicles*. Fakultet for informasjonsteknologi, matematikk og elektroteknikk, 1991.

- [71] Shachak Pe’eri and Glenn Shwaery. Radiometric and photometric determinations of simulated shallow-water environment. *International Journal of Remote Sensing*, 34(18):6437–6450, 2013.
- [72] Ivan Moreno and Ching-Cherng Sun. Modeling the radiation pattern of leds. *Optics express*, 16(3):1808–1819, 2008.
- [73] A Saleh BE and MC Teich. Fundamentals of photonics, 1991.
- [74] William D Philpot. Bathymetric mapping with passive multispectral imagery. *Applied optics*, 28(8):1569–1578, 1989.
- [75] Adiel Elkabetz and Yitzhak Yitzhaky. Background modeling for moving object detection in long-distance imaging through turbulent medium. *Applied optics*, 53(6):1132–1141, 2014.
- [76] Harold T Yura. Small-angle scattering of light by ocean water. *Applied optics*, 10(1):114–118, 1971.
- [77] Harold T Yura. Propagation of finite cross-section laser beams in sea water. *Applied optics*, 12(1):108–115, 1973.
- [78] Clayton Kunz, Chris Murphy, Richard Camilli, Hanumant Singh, John Bailey, Ryan Eustice, Michael Jakuba, Ko-ichi Nakamura, Chris Roman, Taichi Sato, et al. Deep sea underwater robotic exploration in the ice-covered arctic ocean with auvs. In *Intelligent Robots and Systems, 2008. IROS 2008. IEEE/RSJ International Conference on*, pages 3654–3660. IEEE, 2008.
- [79] David A Smallwood and Louis L Whitcomb. Adaptive identification of dynamically positioned underwater robotic vehicles. *Control Systems Technology, IEEE Transactions on*, 11(4):505–515, 2003.
- [80] Shahriar Negahdaripour and Pezhman Firoozfam. An rov stereovision system for ship-hull inspection. *Oceanic Engineering, IEEE Journal of*, 31(3):551–564, 2006.
- [81] James Diebel. Representing attitude: Euler angles, unit quaternions, and rotation vectors. *Matrix*, 58:15–16, 2006.
- [82] Chris McGlone, Edward Mikhail, and Jim Bethel. *Manual of photogrammetry*. 1980.
- [83] FA Kruse, AB Lefkoff, JW Boardman, KB Heidebrecht, AT Shapiro, PJ Barloon, and AFH Goetz. The spectral image processing system (sips) interactive visualization and analysis of imaging spectrometer data. *Remote sensing of environment*, 44(2):145–163, 1993.
- [84] F Eren, S Pe’eri, Y Rzhano, M Thein, and B Celikkol. Optical detector array design for optical sensor based pose detection between unmanned underwater vehicles (uuv). *Oceanic Engineering, IEEE Journal of*, accepted for publication.

- [85] F Eren, M Thein, S Pe’eri, Y Rzhanov, and B Celikkol. Development of pose detection algorithms for dynamic positioning of unmanned underwater vehicles (uuv’s) utilizing optical feedback. *Oceanic Engineering, IEEE Journal of*, submitted.
- [86] David S Casagrande. *Real-time featureless visual odometry for sea floor imaging with a Lagrangian float*. University of Rhode Island, 2013.
- [87] Jignesh N Sarvaiya, Suprava Patnaik, and Salman Bombaywala. Image registration using log-polar transform and phase correlation. In *TENCON 2009-2009 IEEE Region 10 Conference*, pages 1–5. IEEE, 2009.
- [88] George Wolberg and Siavash Zokai. Robust image registration using log-polar transform. In *Image Processing, 2000. Proceedings. 2000 International Conference on*, volume 1, pages 493–496. IEEE, 2000.
- [89] Firat Eren, May-Win Thein, Shachak Pe’eri, Yuri Rzhanov, Barbaros Celikkol, and Robinson Swift. Pose detection and control of multiple unmanned underwater vehicles (uuv’s) using optical feedback. In *OCEANS 2014-TAIPEI*, pages 1–6. IEEE, 2014.
- [90] Rafael C Gonzalez and Richard E Woods. Digital image processing, 2002.
- [91] Yuri Rzhanov, Firat Eren, May-Win Thein, and Shachak Pe’eri. An image processing approach for determining the relative pose of unmanned underwater vehicles. In *OCEANS 2014-TAIPEI*, pages 1–4. IEEE, 2014.
- [92] F Eren, S Pe’eri, Y Rzhanov, M Thein, B Celikkol, and R Swift. An experimental study for feedback and control system using an optical detector array for pose detection of unmanned underwater vehicles (uuv’s). *Optics express*, submitted.
- [93] P Sotiropoulos, D Grosset, G Giannopoulos, and F Casadei. Auv docking system for existing underwater control panel. In *OCEANS 2009-EUROPE*, pages 1–5. IEEE, 2009.
- [94] Hanumant Singh, James G Bellingham, Franz Hover, S Lemer, Bradley A Moran, Keith von der Heydt, and Dana Yoerger. Docking for an autonomous ocean sampling network. *Oceanic Engineering, IEEE Journal of*, 26(4):498–514, 2001.
- [95] Martin F Bowen and Donald B Peters. A deep sea docking station for odyssey class autonomous underwater vehicles. Technical report, Woods Hole Oceanographic Institution, 1998.
- [96] Shachak Peeri, James V Gardner, Larry G Ward, and John Ru Morrison. The seafloor: A key factor in lidar bottom detection. *Geoscience and Remote Sensing, IEEE Transactions on*, 49(3):1150–1157, 2011.
- [97] NOAA Office of Coast Survey (1983) Portsmouth Harbor, <http://www.charts.noaa.gov/pdfs/13283.pdf>, Accessed: 2015-02-12.

- [98] NOAA Center for Operational Oceanographic Products and Services (2007) Tides and Currents, <http://tidesandcurrents.noaa.gov/cdata/dataplot?id=pir0702&bin=3&bdate=20070519&edate=20070520&unit=1&timezone=utc>, Accessed: 2015-02-12.

APPENDIX A

Numerical Simulator Algorithms and Frame Design

Simulator Input

- Array dimensions
- Relative geometrical shift in x, y, z, θ, ψ
- Number of optical elements to be placed on the array
- Light source characteristics (light distribution Root Mean Square value, divergence angle)
- Diffuse attenuation coefficient

Figure A.1: Numerical Simulator input parameters

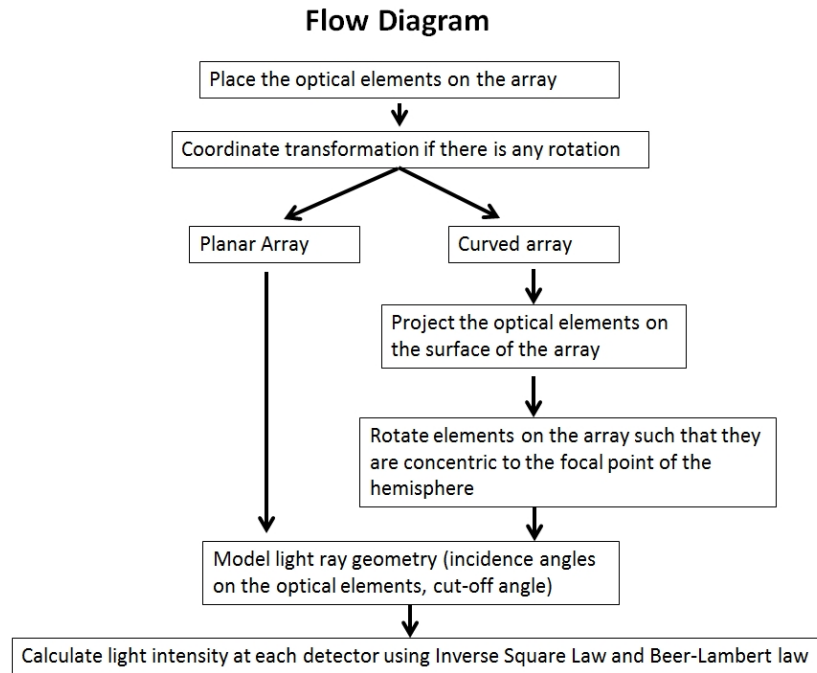


Figure A.2: Numerical Simulator Flow Diagram.

Detection and control strategy for 4-DOF system
x, y, z and yaw

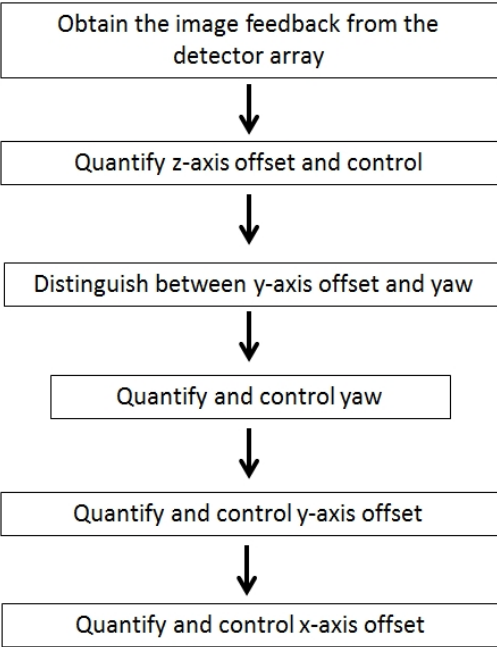


Figure A.3: 4-DOF system detection and control strategy.

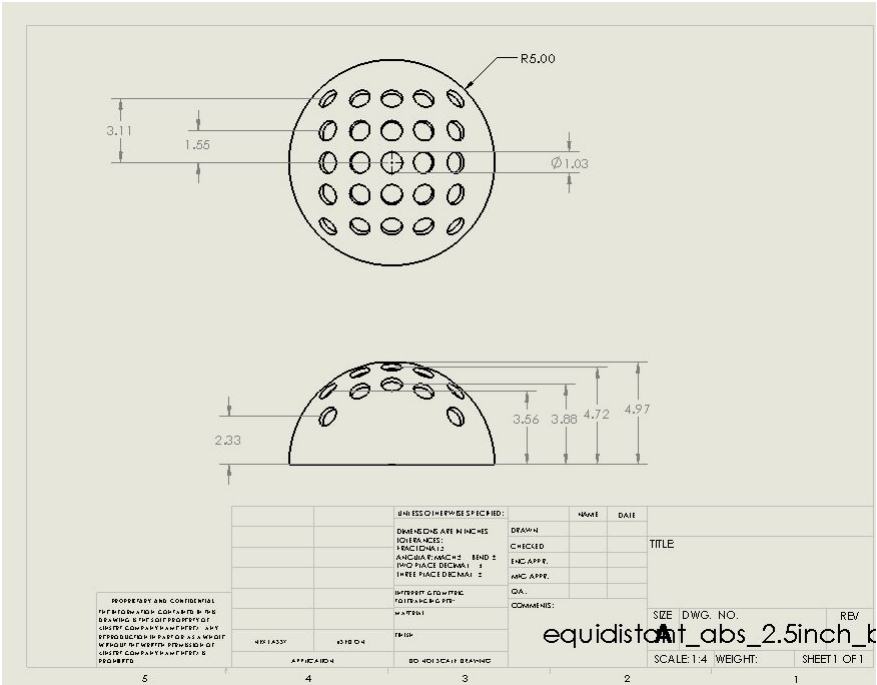


Figure A.4: Detector Array Frame dimension drawing.

APPENDIX B

Photodiode Data Collection Procedure using Beagleboard-XM and two Arduinos

This section demonstrates the data collection procedure using the onboard computer Beagleboard-XM (BB-XM) and two Arduinos used as A/D converters. Any photodiodes can be used in this type of setup and here Hamamatsu S1133 will be used. In the actual experiments Thorlabs SM05PD1A will be used.

The data collection procedure is like the following. Photodiodes intersect the light and converts that into current. A voltage reading across the terminals is done by two separate Arduino A/D input pins of 10-bits, i.e. 0-1023 bits. Currently, there are 9 photodiodes so there will be 5 photodiodes on one Arduino and 4 on the other. Arduinos are connected serially to the BB-XM via the USB ports. BB-XM is connected to a PC through a RS-232 (on BB-XM) to USB cable (on PC side) (Figure B.1). Python serial libraries are used for communication. In addition, all the code to collect the data is written in Python programming language.

This section is divided into two sections,

1. Arduino
2. Beagleboard-XM (BB-XM)

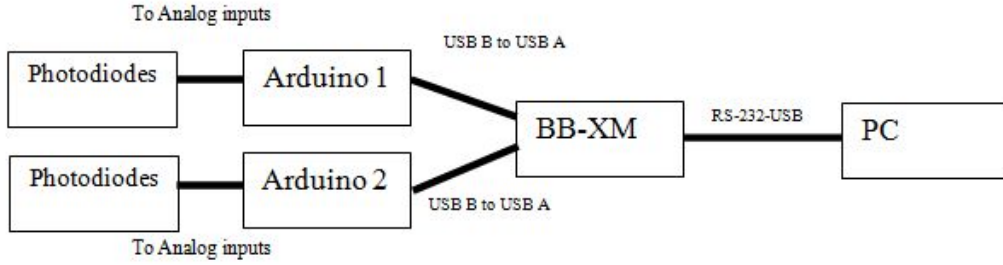


Figure B.1: Photodiode-PC communication general diagram.

B.1 Arduino

1. Upload the Arduino sketches (The Arduino sketch for this application is in the folder hmtsu. The programs name is hmtsu.ino) to the Arduino Boards on a PC. Make sure that the program is uploaded separately to the two boards and modify the program accordingly. For example, there are 25 photodiodes and so Arduinos will get 13 and 12 PD readings accordingly. Change the number of PDs specified in the sketch accordingly (Figure B.2).
2. Disconnect the Arduino from the PC.

B.2 Beagleboard-XM (BB-XM)

In order to access BB-XM, we use the Linux (Ubuntu) operating system.

1. Power the BB-XM. We use a RS-232 to USB cable here. RS-232 cable is connected to the BB-XM and the USB end connects to the PC. Connect the Arduino USB cables to the two of BB-XM USB ports. Make sure the SD card is in BB-XM. BB-XM will be powered from PC in experiments (We will connect a battery in later stages). After making sure everything is connected, connect the barrel end of the 5V barrel jack to USB power cable to the BB-XM and the USB end to the PC (Figure B.3).

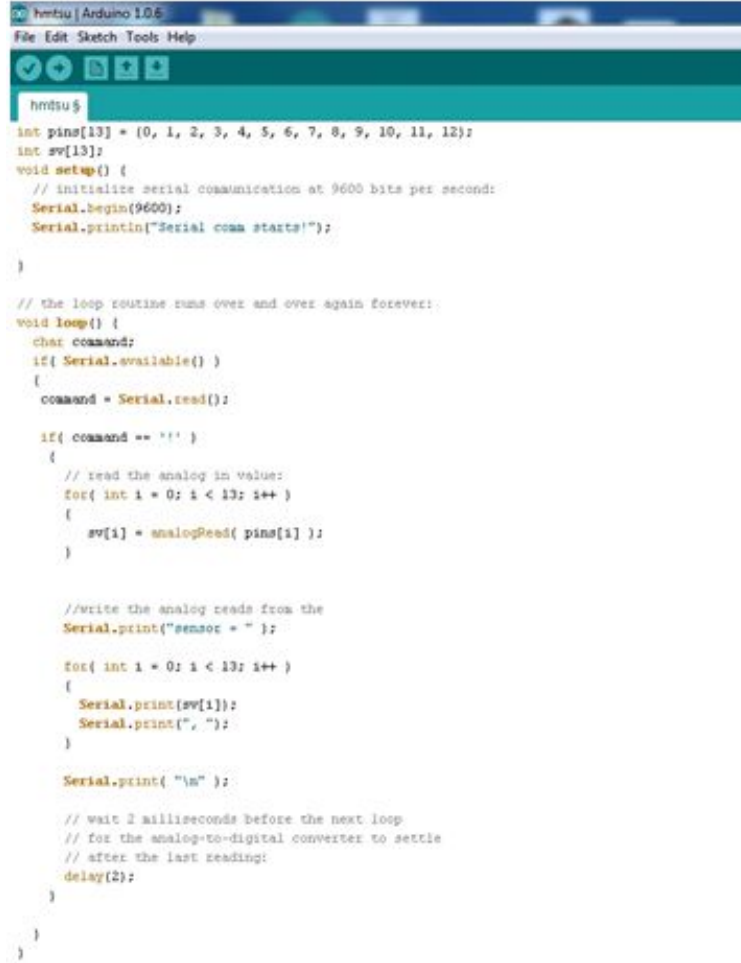


Figure B.2: Arduino sketch. This will be for one Arduino. For the other Arduino change the 13 to 12 and other variables accordingly.

2. Connect to the BB-XM from a PC through minicom. Open a terminal in Ubuntu by Ctrl+Alt+T. In the terminal window type: **minicom**. It should display Initializing Modem on the screen. (If it does not connect, the port name might not be correct. In this case find the correct port name and type **minicom D /dev/ttyUSBX**. Note: ttyUSBX is the device name. You can find the device name by typing **cd /dev** and then type **ls**). (Figures B.4 and B.5)
3. After accessing BB-XM through minicom, arm login will not accept what you type as password initially. At the second attempt, type armlogin: **frat**, password:**1985fir**. Remember that you will not be able to see what you type in the password prompt

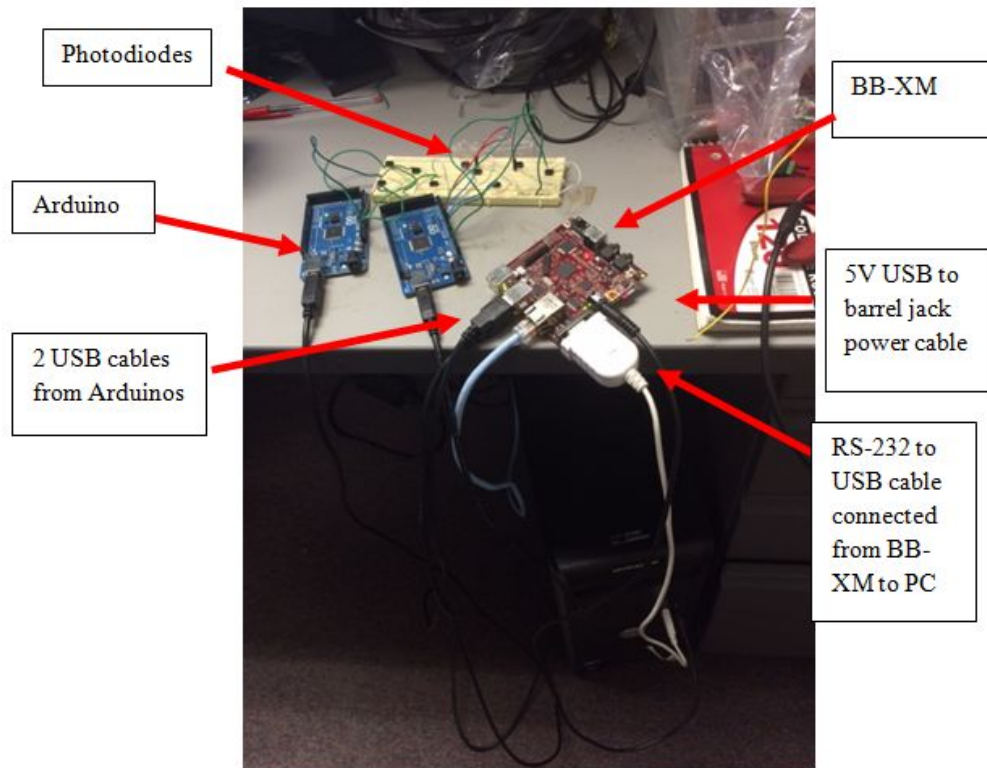


Figure B.3: BB-XM setup.

area. (Figure B.6)

4. Similarly, you can check the Arduino device names on BB-XM by typing `cd /dev` and then typing `ls` in the minicom terminal. The Arduino device names are typically `ttyACM0` and `ttyACM1`. These port names are very important while establishing the serial connection between BB-XM and the PC. (Figure B.7)
5. For serial communication protocol and for data collection code, we use Python programming language in both platforms, PC and BB-XM.
6. To access the data collection program in BB-XM, type `cd rovr`. (Note: If you are in `/dev` folder, then you need to go back to home by typing `cd`) All the programs are in the `rovr` folder. Then type `ls` to see the programs. The program to collect data from Arduinos to the BB-XM is `readPD.py`



Figure B.4: Minicom login screen.

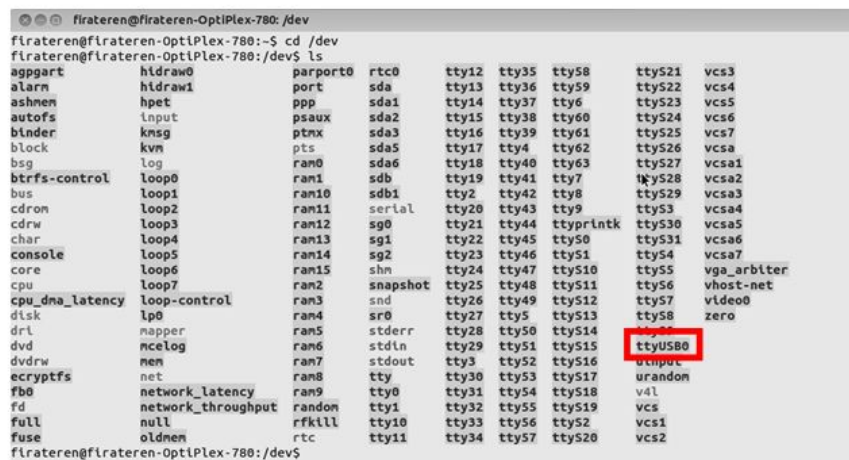


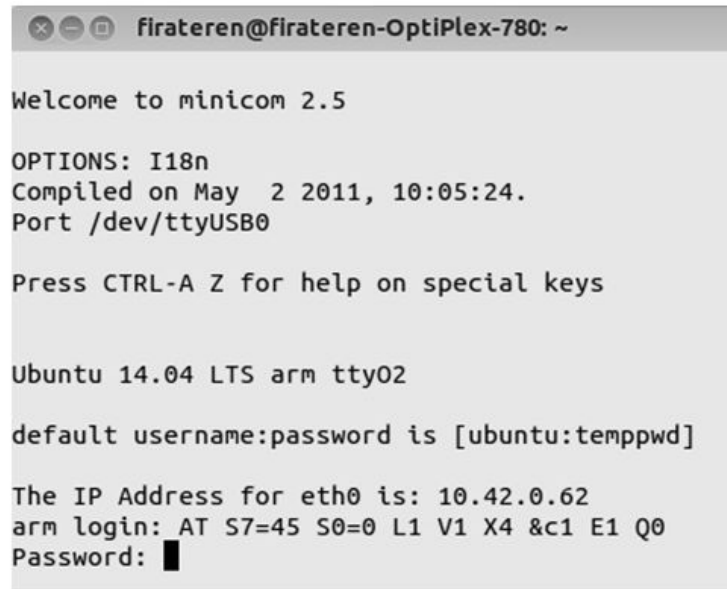
Figure B.5: Serial to USB port check on PC.

7. In order to access the contents of the program readPD.py, type **vim readPD.py** (Figure B.8). vim is the name of the text editor. Make sure the device names match with the connected device names. **IMPORTANT:** If you need to edit the file, you need to go into insert mode. Do this by hitting I button on keyboard. When it is in insert mode, you will see - - INSERT - - at the bottom of the program. If you are not in the insert mode, you can not change the contents. **When you are in the INSERT mode:**

To save and exit type: **wq**

To exit without saving, type: **q!**

To exit only if you have not changed anything, type: **q**

A screenshot of a terminal window titled 'firateren@firateren-OptiPlex-780: ~'. The terminal displays the following text: 'Welcome to minicom 2.5', 'OPTIONS: I18n', 'Compiled on May 2 2011, 10:05:24.', 'Port /dev/ttyUSB0', 'Press CTRL-A Z for help on special keys', 'Ubuntu 14.04 LTS arm tty02', 'default username:password is [ubuntu:temppwd]', 'The IP Address for eth0 is: 10.42.0.62', 'arm login: AT S7=45 S0=0 L1 V1 X4 &c1 E1 Q0', and 'Password: ' followed by a black square cursor.

```
firateren@firateren-OptiPlex-780: ~  
  
Welcome to minicom 2.5  
  
OPTIONS: I18n  
Compiled on May 2 2011, 10:05:24.  
Port /dev/ttyUSB0  
  
Press CTRL-A Z for help on special keys  
  
Ubuntu 14.04 LTS arm tty02  
  
default username:password is [ubuntu:temppwd]  
  
The IP Address for eth0 is: 10.42.0.62  
arm login: AT S7=45 S0=0 L1 V1 X4 &c1 E1 Q0  
Password: █
```

Figure B.6: Arm login and password screen.

8. The data collection and observation will be on the PC side. Open a new terminal on PC (Ctrl+Alt+T). Then type **cd Desktop/test**. The name of the program for data collection is **getPD.py**. You can also access the program by clicking the test folder in Desktop and double clicking on the **getPD.py** program. (Figure B.9). This program reads the serial output coming from the BB-XM and saves it into a text file.
9. To collect data, go to the minicom terminal, go to the **rov** folder and type **python readPD.py**. You will see the series of numbers printed out on the minicom terminal.
10. Now go to the PC terminal to the test folder on Desktop. Type **python getPD.py**. You will see an error saying that the device reports open but no serial data. Go to the minicom terminal and close it. If minicom screen is open, there will be no data collection.
11. Go back to the PC terminal and once again type **python getPD.py**. The data collection will start.

IMPORTANT: You can kill the data collection by pressing CTRL+C on the PC terminal. For data collection at a different geometry, change the filename to your


```

flrat@arm: ~/rov
code to read serial out of arduino
# TODO: download VIM for syntax highlighting.

import serial
import re

ser = serial.Serial('/dev/ttyACM0', baudrate = 9600)
ser2 = serial.Serial('/dev/ttyACM1', baudrate = 9600)
pc = serial.Serial('/dev/ttyO2', baudrate = 115200)

#f= open('test_data.txt','w')
#angles = [0]*6

while True:
    ser.write('!')
    data1=ser.readline()
    #print data
    # data = re.findall( '\d+', data)
    # data = filter( None, data )
    #get the average of the data list
    #time.sleep(0.25)

    ser2.write('!')
    data2=ser2.readline()
    time.sleep(0.1)
    # print data1+data2
    # print 'flrat'+hop
    # data=data1+' '+data2
    # pc.write(data1+'\r\n'+data2+'\r\n')
    pc.write(data1+data2)

```

Make sure device names are correct

Figure B.8: The program that reads data from two Arduinos and passes it to the PC. (readPD.py).

```

getPD.py (~/Desktop/test) - gedit
# program to get the serial data from BB-XM
# use this file to collect data

import serial
import time
import re

# make sure the connection names are correct
sercom=serial.Serial(port='/dev/
ttyUSB0',baudrate=115200,parity=serial.PARITY_NONE,stopbits=serial.STOPBITS_ONE,bytesize=serial.EIGHTBITS)

sercom.open()
sercom.isOpen()

# make sure to change the filename to correspond to the test coordinate
f=open('x=4.5m_y=0m_z=0m_yaw=0deg.txt','w')

while True:
    # bytesToRead = sercom.inWaiting()
    x=sercom.readline()
    f.write(time.ctime()+' '+x)
    f.flush()
    print time.ctime()+' '+x
f.close()

```

Make sure device name is correct

Text file. You can specify the name for the actual geometry.

Figure B.9: The program that reads the serial output of BB-XM and saves it to a file (getPD.py).

APPENDIX C

Programs for Experimental Data Collection and Analysis

This chapter includes the programs that were written for photodiode data collection. The photodiode readings are first sampled in the Arduino A/D sketch, i.e. Arduino environment program. Then, the readings from two Arduinos are received by the BB-XM in two different USB ports. The program that resides in the PC, i.e. readPD.py, saves the readings in a text file. Then a separate MATLAB file was written to read the contents of the text file.

C.1 Program to collect photodiode data to Arduino (hmtsu.ino)

```
int pins[13] = {0, 1, 2, 3, 4,5,6,7,8,9,10,11,12};
int sv[13];
void setup() {
    // initialize serial communication at 9600 bits per second:
    Serial.begin(9600);
    Serial.println("Serial comm starts!");
}
// the loop routine runs over and over again forever:
void loop() {
    char command;
    if( Serial.available() )
    {
        command = Serial.read();
```

```

    if( command == '!' )
    {
        // read the analog in value:
        for( int i = 0; i < 13; i++ )
        {
            sv[i] = analogRead( pins[i] );
        }

        //write the analog reads from the
        Serial.print("sensor = " );
        for( int i = 0; i < 13; i++ )
        {
            Serial.print(sv[i]);
            Serial.print(", ");
        }

        Serial.print( "\n" );

        // wait 2 milliseconds before the next loop
        // for the analog-to-digital converter to settle
        // after the last reading:
        delay(2);
    }
}
}

```

C.2 Program to get the photodiode readings from Arduino to BB-XM (readPD.py)

```

# code to read serial out of arduino

import serial

import re

```

```

import time

ser = serial.Serial('/dev/ttyACM0', baudrate = 9600)
ser2 = serial.Serial('/dev/ttyACM1', baudrate = 9600)
pc = serial.Serial('/dev/tty02', baudrate = 115200 )

while True:

    ser.write("!")

    data1=ser.readline()

    ser2.write("!")

    data2=ser2.readline()

    time.sleep(0.1)

    pc.write(data1+data2)

```

C.3 Program to get the photodiode readings from BB-XM to PC and save as a .txt file (getPD.py)

```

# program to get the serial data from BB-XM
# use this file to collect data

import serial
import time
import re

# make sure the connection names are correct

sercom=serial.Serial(port='/dev/ttyUSB0',baudrate=115200,parity=serial.PARITY_NONE,stopbits=se

sercom.open()

sercom.isOpen()

# make sure to change the filename to correspond to the test coordinate

f=open('single arduino.txt','w')

while True:

# bytesToRead = sercom.inWaiting()

```

```

x=sercom.readline()

f.write(time.ctime()+','+x)

f.flush()

# print time.ctime()+','+x

f.close()

```

C.4 Program that extracts the intensity readings from the text file and processes

```

% Data processing program that reads in the txt files and parses the values
% into photodiode values

clear;clc;
close all

%% 1) Data Parsing
count=1;

% fileID=fopen('x4.5_y0_z1_upright.txt','r'); %1
xi=4.5;
zi=1.2;
yi=0.3;
% for xi=4.5:8.5
    for zi=1:0.2:1.8
        for yi=-0.6:0.3:0.6

fileID=fopen(sprintf('x%2g_y%1g_z%1g.txt',xi,yi,zi));
N=5;
data=fread(fileID, [1 inf], '*char');

```

```

% Number of detectors on Arduino 1 and 2

PD1=13;
PD2=12;

Psum=PD1+PD2+2; % This property is used for data parsing
% find 2014 in the file.. Change this to 2015 in the next year
cycles = strfind(data, '2015');
fclose(fileID);
% Day_ind=strfind(data,Day);
comaind=strfind(data,',');
% Day_ind=Day_ind(2:end)'
k=2;

if comaind(14)-comaind(13)<=5
for i=1:length(cycles)/2
Ard1(i,:)=str2num(data(cycles(2*i-1)+5 : comaind(Psum*i-PD1)));
Ard2(i,:)=str2num(data(cycles(2*i)+5: comaind(Psum*i)));
k=k+1;

end
else

PD1=12;PD2=13;
for i=1:length(cycles)/2
Ard2(i,:)=str2num(data(cycles(2*i-1)+5 : comaind(Psum*i-PD1-2)));
Ard1(i,:)=str2num(data(cycles(2*i)+5: comaind(Psum*i)));
k=k+1;

end

```



```

end

PD=[Ard1 Ard2];

%% Plot of the average
PDsum=mean(PD);
stdev(count,:)=std(PD);
for i=1:5
    B(i,1:5)=PDsum(1,5*i-4:5*i ) ;
end

subplot(5,5,count)
imagesc(B)
caxis([0 1023])

%% 2) Moment Calculation
[row,col]=find(B==max(max(B)));
row=row(1);
col=max(col); % Sometimes multiple values are returned. Will pick max

row;

%% Sub-pixel accuracy algorithm
% First derivatives
dIdx= (B(row,col+1)-B(row,col-1))/2;
dIdy= (B(row+1,col)-B(row-1,col))/2;
% Second derivatives
d2Idx2=B(row,col+1)-2*B(row,col)+B(row,col-1);
d2Idy2=B(row+1,col)-2*B(row,col)+B(row-1,col);
% Second partial derivatives

```

```

d2Idxdy=0.25*(B(row+1,col+1)+B(row-1,col-1)-B(row-1,col+1)-B(row+1,col-1));
H=[d2Idx2 d2Idxdy; d2Idxdy d2Idy2];
D=[dIdx;dIdy];
S=-inv(H)*D;
col_sub(count)=col+S(1); % Calculate the sub-pixel accuracy
row_sub(count)=row+S(2);
title(sprintf('x=%1gm y=%1gm z=%1gm ',xi,yi,zi))
xf=1:N;
yf=1:N;
[Ypos,Zpos]=meshgrid(xf,yf);
Ysort=reshape(Ypos,N*N,1);
Zsort=reshape(Zpos,N*N,1);
i=0;li=1;
for i=0:2
    for j=0:2
        k=1;
        for k=1:N*N
            Mom(k,li)=((Ysort(k)-col_sub(count))^i) * ((Zsort(k)-row_sub(count))^j)
                *PDsum(k);
            Mom_norm(k,li)=Mom(k,li)/sum(PDsum);
        end
        li=li+1;
    end
end
Mnt=sum(Mom_norm);
Mmnt(3*count-2:3*count,:)=transpose(reshape(Mnt,3,3));
count=count+1;
end
end

```

```
% end  
sprintf('row values are between %1g-%1g',min(row_sub),max(row_sub))  
sprintf('col values are between %1g-%1g',min(col_sub),max(col_sub))
```

APPENDIX D

Beam Patterns from Experimental Data

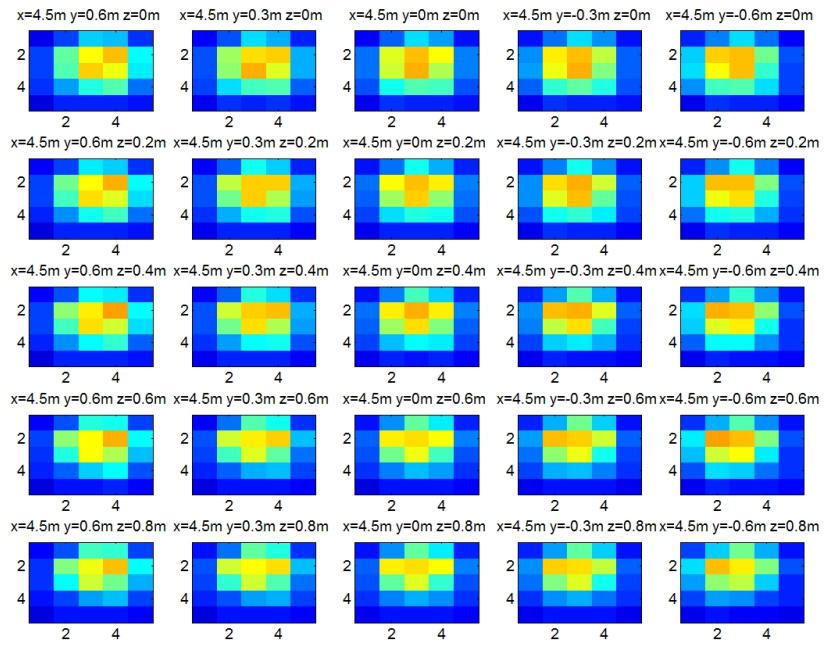


Figure D.1: Beam pattern images at $x=4.5$ m.

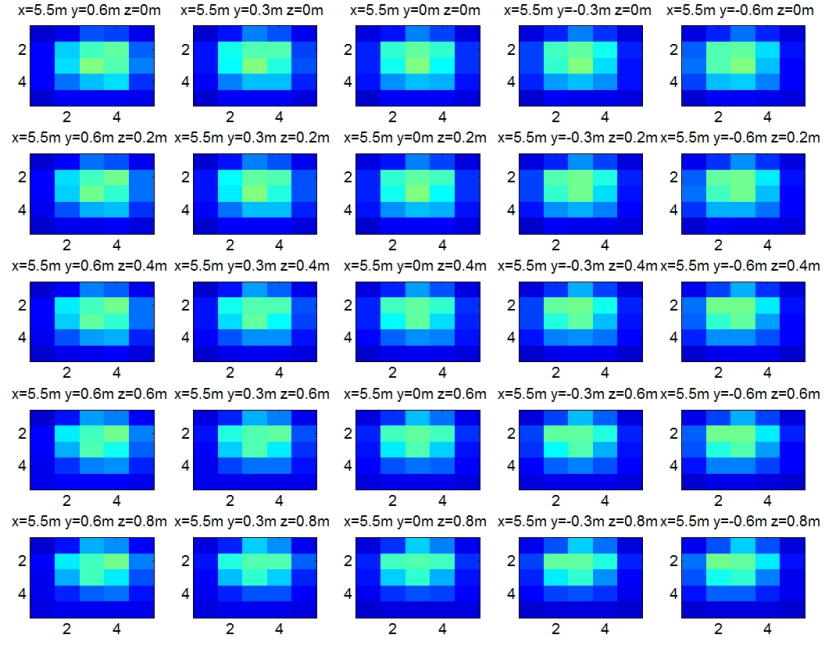


Figure D.2: Beam pattern images at $x=5.5$ m.

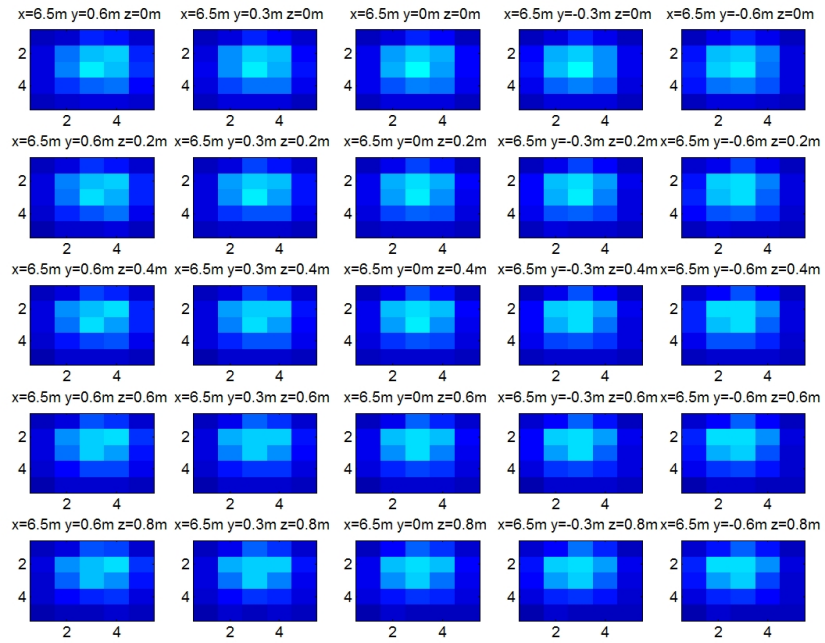


Figure D.3: Beam pattern images at $x=6.5$ m.

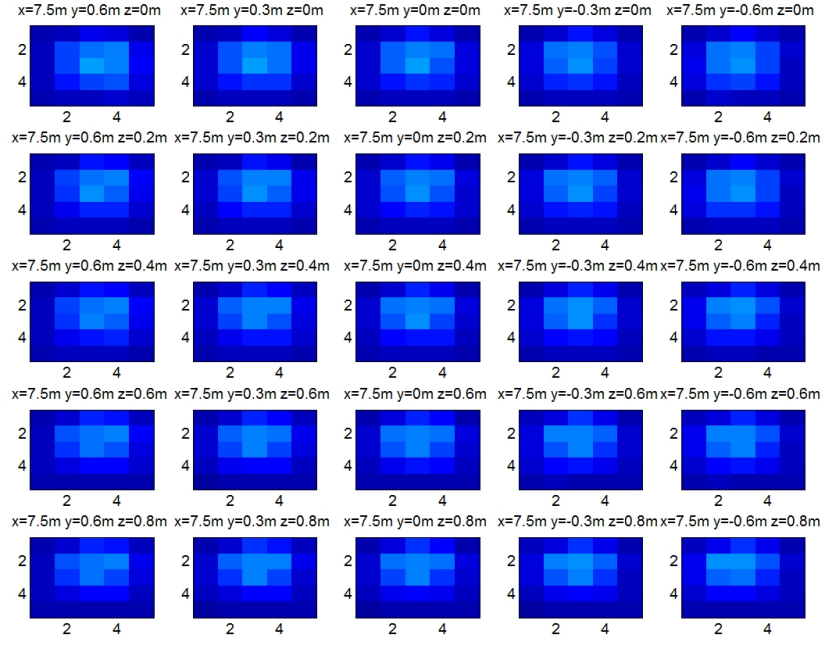


Figure D.4: Beam pattern images at $x=7.5$ m.

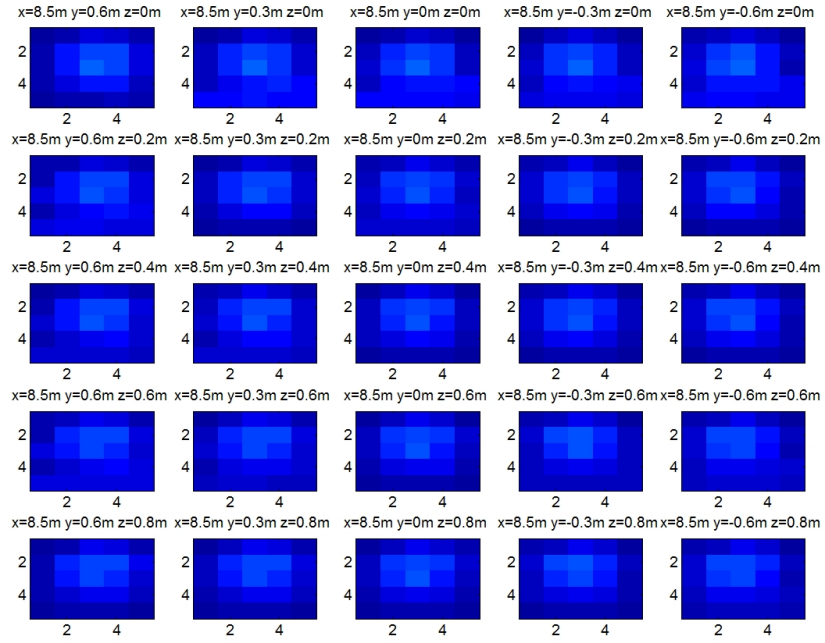


Figure D.5: Beam pattern images at $x=8.5$ m.